

Duquesne University

## Duquesne Scholarship Collection

---

Electronic Theses and Dissertations

---

Winter 12-20-2020

# Mechanical Strength Assessment of Pharmaceutical Compacts with Refractive Index Measurements from Terahertz Time of Flight Spectroscopy

Shikhar Mohan

Follow this and additional works at: <https://dsc.duq.edu/etd>

---

### Recommended Citation

Mohan, S. (2020). Mechanical Strength Assessment of Pharmaceutical Compacts with Refractive Index Measurements from Terahertz Time of Flight Spectroscopy (Doctoral dissertation, Duquesne University). Retrieved from <https://dsc.duq.edu/etd/1942>

This Immediate Access is brought to you for free and open access by Duquesne Scholarship Collection. It has been accepted for inclusion in Electronic Theses and Dissertations by an authorized administrator of Duquesne Scholarship Collection.

MECHANICAL STRENGTH ASSESSMENT OF PHARMACEUTICAL COMPACTS  
WITH REFRACTIVE INDEX MEASUREMENTS FROM TERAHERTZ TIME OF  
FLIGHT SPECTROSCOPY

A Dissertation

Submitted to the Graduate School of Pharmaceutical Sciences

Duquesne University

In partial fulfillment of the requirements for  
the degree of Doctor of Philosophy

By

Shikhar Mohan

December 2020

Copyright by  
Shikhar Mohan

2020

MECHANICAL STRENGTH ASSESSMENT OF PHARMACEUTICAL COMPACTS WITH  
REFRACTIVE INDEX MEASUREMENTS FROM TERAHERTZ TIME OF FLIGHT  
SPECTROSCOPY

By

Shikhar Mohan

Approved June 29, 2020

---

Carl A. Anderson, Ph.D.  
Associate Professor of Pharmaceutics  
Graduate School of Pharmaceutical  
Sciences, Duquesne University  
(Committee Chair)

---

James K. Drennen, III, Ph.D.  
Associate Professor of Pharmaceutics  
Associate Dean for Graduate Programs  
and Research, Duquesne University  
(Committee Member)

---

Peter L.D. Wildfong, Ph.D.  
Associate Professor of Pharmaceutics  
Graduate School of Pharmaceutical  
Sciences, Duquesne University  
(Committee Member)

---

Ira S. Buckner, Ph.D.  
Associate Professor of Pharmaceutics  
Graduate School of Pharmaceutical  
Sciences, Duquesne University  
(Committee Member)

---

Eiji Kato, Ph.D.  
Senior Engineer  
New Concept Product Initiative  
Advantest Corporation  
(External Committee Member)

## ABSTRACT

# MECHANICAL STRENGTH ASSESSMENT OF PHARMACEUTICAL COMPACTS WITH REFRACTIVE INDEX MEASUREMENTS FROM TERAHERTZ TIME OF FLIGHT SPECTROSCOPY

By

Shikhar Mohan

December 2020

Dissertation supervised by Carl A. Anderson, PhD.

The mechanical strength of pharmaceutical compacts is often considered as a critical quality attribute for roller and tablet compaction processes. Most traditional mechanical strength tests are destructive, thus, preventing further material testing. This thesis expands on the application of terahertz time of flight spectroscopy (THz-TOF) as a nondestructive technique for assessing mechanical strength. This technique is able to extract the refractive index; which is a function of porosity and crystallinity of the solid. Thus, it was hypothesized that refractive index measurements from terahertz time of flight spectroscopy are directly related to porosity; therefore, these nondestructive measurements are able to correlate to the mechanical strength of pharmaceutical compacts. This hypothesis was achieved by generating refractive index based models for predicting various types of destructive mechanical strength measurements including radial tensile strength, indentation hardness, and axial tensile strength for pharmaceutically relevant tablet systems. This work provides further support for THz-TOF as a potential process analytical technology tool for roller compaction and/or tablet compaction processes.

## DEDICATION

This dissertation is dedicated to my grandparents.

## ACKNOWLEDGMENT

I would like to thank all my well-wishers. I would especially like to thank my wife, Jordan. She joined me in Pittsburgh after our marriage. My life significantly improved afterwards as she became my bodyguard. She viciously protected me from anything that would cause me harm, especially my worst enemy, bugs/spiders. But also, unfortunately, great tasting unhealthy food. She sacrificed a lot for me including a honeymoon trip and her sanity to finally see me being graduated after almost a decade. Therefore, I will have to do whatever she asks of me including eating her weird nutritious cooking. The support of Jordan, my family, and my close friends were critical for me in achieving my graduate degree at Duquesne University.

## Table of Contents

ABSTRACT.....	iv
ACKNOWLEDGMENT.....	vi
LIST OF FIGURES.....	ix
Chapter 1: Introduction .....	1
1.1. Statement of the problem .....	1
1.2. Hypothesis and Specific Aims .....	3
1.3. Literature Review .....	4
1.3.1. Theory .....	5
1.3.2. Methods to Determine Refractive Index of Solids.....	11
1.3.3. Pharmaceutical Applications of Refractive Index .....	38
1.3.4. Summary .....	52
Chapter 2: Evaluating the Robustness of Terahertz Based Porosity Models Against Chemical Composition and Process Parameter Variations for Multicomponent Pharmaceutical Compacts .....	56
2.1. Introduction .....	56
2.2. Materials and Methods.....	61
2.2.1. Materials .....	61
2.2.2. Tablet Manufacturing Process .....	62
2.2.3. Blend Assay .....	63
2.2.4. Experimental Design .....	64
2.2.5. Tablet Porosity .....	66
2.2.6. Terahertz Time of Flight Spectroscopy .....	66
2.2.7. Terahertz Based Porosity Modeling Methods .....	68
2.3. Results and Discussion .....	71
2.4. Summary and Conclusion.....	86
Chapter 3: Development of refractive index based radial tensile strength model .....	87
3.1. Introduction .....	87
3.2. Materials and Methods.....	90
3.2.1. Materials .....	90
3.2.2. Experimental Design .....	91
3.2.3. Tablet Porosity .....	92
3.2.4. Terahertz Time of Flight Spectroscopy .....	92
3.2.5. Radial Tensile Strength .....	93
3.3. Results and Discussion .....	93
3.4. Summary and Conclusion.....	99

Chapter 4: Development of refractive index based hardness model for intra tablet mechanical strength assessment.....	100
4.1. Introduction .....	100
4.2. Materials and Methods.....	104
4.2.1. Materials .....	104
4.2.2. Experimental Design .....	104
4.2.3. Indentation Hardness Measurements .....	106
4.2.4. Terahertz Time of Flight Spectroscopy .....	107
4.3. Results and Discussion .....	108
4.4. Summary and Conclusion.....	116
Chapter 5: Investigation of the relationship between terahertz pulse reflections at the layer to layer interface to axial tensile strength for bilayer tablets.....	118
5.1. Introduction .....	118
5.2. Materials and Methods.....	121
5.2.1. Materials .....	121
5.2.2. Experimental Design .....	122
5.2.3. Terahertz Time of Flight Spectroscopy .....	124
5.2.4. Axial Tensile Strength.....	124
5.3. Results and Discussion .....	125
5.4. Summary and Conclusion.....	140
Chapter 6: Conclusion .....	142
Appendix: Terahertz Time of Flight Spectroscopy as a Coating Thickness Reference Method for Partial Least Squares Near Infrared Spectroscopy Models .....	146
Abstract.....	146
A.1. Introduction .....	147
A.2. Materials and Methods .....	150
A.2.1. Core Tablet .....	150
A.2.2. Coating Solution.....	151
A.2.3. Tablet Coating Process .....	151
A.2.4. Terahertz Based Coating Thickness .....	152
A.2.5. Weight Gain Based Coating Thickness.....	153
A.2.6. Near Infrared Spectral Collection .....	155
A.2.7. Experimental Design .....	155
A.3. Results and Discussion.....	156
A.4. Summary and Conclusion .....	164

## LIST OF FIGURES

Figure 1.1: Schematic of light refracting in a denser medium.....	6
Figure 1.2: Schematic of light refracting in a denser medium.....	7
Figure 1.3: prism deviation method (a) and the corresponding angle of deviation versus angle of incidence plot (b) .....	12
Figure 1.4: Michelson interferometer schematic .....	17
Figure 1.5: Fabry Perrot interferometer schematic .....	19
Figure 1.6: Linearly polarized light (a) and elliptically polarized light (b) .....	21
Figure 1.7: Photometric ellipsometer schematic.....	21
Figure 1.8: Advantest’s terahertz pulsed spectroscopy in transmittance setup .....	26
Figure 1.9: Terahertz transmittance time domain spectra of air (a) and tablet sample (b) .....	28
Figure 1.10: Terahertz absorption and refractive index spectrum of Apo-ranitidine <sup>80</sup> .....	28
Figure 1.11: The measured versus calculated refractive index plots associated with Einshour (a), Vogel R <sub>d</sub> (b), and Vogel M <sub>nd</sub> (c) empirical methods for literature surveyed compounds <sup>98</sup> .....	33
Figure 1.12: The measured versus calculated refractive index plots associated with Einshour (a), Vogel R <sub>d</sub> (b), and Vogel M <sub>nd</sub> (c) empirical methods for Pfizer APIs <sup>98</sup> .....	34
Figure 1.13: Refractive index versus inverse temperature of polystyrene film developed using ellipsometric method <sup>106</sup> and of poly(oxyethylene) using terahertz spectroscopy <sup>107</sup> .....	39
Figure 1.14: Refractive index spectra of 4-component tablets (grey) along with pure component tablets (black) measured with terahertz spectroscopy <sup>20</sup> .....	43
Figure 1.15: Terahertz measurements of peak position, peak THz electric field, and time delay (appropriately color coded) versus temperature for carbamazepine with the specific solid states appropriately labeled <sup>108</sup> .....	45
Figure 1.16: Terahertz absorption and refractive index spectra of theophylline’s polymorph I (top) and II (bottom) along with their combination. The polymorph forms were controlled by adjusting materials storage time in 523 K environment <sup>79</sup> .....	46
Figure 1.17: Refractive index versus porosity trend. The numbers in the figure represent each tablet’s thickness value in millimeters <sup>87</sup> .....	47
Figure 1.18: Effective refractive index versus disintegration time (a) and amount of drug dissolved (b) trends <sup>2</sup> .....	48
Figure 1.19: Effective refractive index versus disintegration time (a) and amount of drug dissolved (b) trends <sup>2</sup> .....	50
Figure 2.20: Experimental Design .....	65
Figure 2.21: Porosity versus compression force trend.....	72
Figure 2.22: Time domain signal of reference (red) and of sample (blue).....	73
Figure 2.23: Frequency domain refractive index spectra of the calibration tablets.....	74
Figure 2.24: Correlation between refractive values from time domain method and frequency domain method.....	75
Figure 2.25: Porosity versus time domain refractive index .....	75
Figure 2.26: Intrinsic refractive index of each chemical composition design using the zero porosity approximation and Bruggeman models .....	78
Figure 2.27: Zero point approximation model predicting test sets including process parameter variation (a) and chemical composition variation (b).....	79

Figure 2.28: Bruggeman model predicting test set including process parameter variation (a) and chemical composition variation (b) .....	80
Figure 2.29: Linear regression model predicting test set including process parameter variation (a) and chemical composition variation (b).....	82
Figure 2.30: The latent variables (a), predictions on test set 1 (b), and model predictions on test set 2 (c) of the PLS terahertz based porosity model .....	84
Figure 3.31: Experimental design .....	91
Figure 3.32: Porosity versus effective refractive index trend.....	94
Figure 3.33: Porosity versus radial tensile strength (a) and ln(radial tensile strength) (b) trends	95
Figure 3.34: The trend between RTS(MPa) and effective refractive index and between ln(RTS) and effective refractive index.....	95
Figure 3.35: Model relating ln(RTS ) to effective refractive index generated according to global approach.....	97
Figure 4.36: Linear models relating ln(RTS) to effective refractive index for chemical design 1 (a), 2 (b), 3 (c), and 4 (d) according to hierarchal approach .....	98
Figure 4.37: Mean absorbance spectrum of all tablets (a) and the mean refractive index spectra of each tablet appropriately color coded according the applied compression force (b).....	109
Figure 4.38: Refractive index images at 0.5 THz of the five tablets produced with varying compression force .....	110
Figure 4.39: Compression profile during indentation of lactose monohydrate tablet produced at 4000 lbs compression force. The blue trend represents the compression trend while the red trend represents the extrapolation performed to determine indentation depth.....	111
Figure 4.40: Indented lactose monohydrate tablet produced at 4000 lbs compression force (a) and the corresponding pixels selected (b) for development of refractive index based model.....	112
Figure 4.41: Truncated refractive index spectra (a) used for model development. The resulting latent variable (b), scores (c), and model results (c) plots for the developed PLS model between refractive index spectra and indentation hardness. ....	113
Figure 4.42: Refractive index image at 0.5 THz (a) for a new tablet produced at 4000 lbs compression force converted into a hardness image (b) using the refractive index based hardness model.....	114
Figure 4.43: Lactose monohydrate produced at 3000 lbs with no external lubrication (a and b) and with external lubrication (c and d). ....	115
Figure 4.44: Hardness distribution and QQ plot for non-lubricated (a and c) and lubricated lactose (b and d) monohydrate tablets .....	116
Figure 5.45: Pure lactose monohydrate and MCC raw average time domain signal (a and b) and preprocessed with frequency filter (b and d) .....	126
Figure 5.46: Mean time domain signal of monolithic MCC (a) and MCC/lactose mixture (b) tablets and bilayer MCC-MCC (c) and MCC-Lactose (d) tablets. ....	127
Figure 5.47: Mean time domain signal of MCC-Lac bilayer tablets with tamping force of 0 (a), 1 (b), 3 (c), 5 (d), and 7 (e) kN and MCC side of the tablet facing the terahertz source and detector. ....	129
Figure 5.48: Layer interface reflection intensity maps of MCC-Lac bilayer tablets with tamping force of 0 (a), 1 (b), 3 (c), 5 (d), and 7 (e) kN and MCC side of the tablet facing the terahertz source and detector. ....	130

Figure 5.49: Mean time domain signal of MCC-Lac bilayer tablets with tamping force of 0 (a), 1 (b), 3 (c), 5 (d), and 7 (e) kN and lactose monohydrate side of the tablet facing the terahertz source and detector. ....	131
Figure 5.50: Layer interface reflection intensity maps of MCC-Lac bilayer tablets with tamping force of 0 (a), 1 (b), 3 (c), 5 (d), and 7 (e) kN and MCC side of the tablet facing the terahertz source and detector. ....	131
Figure 5.51: Mean time domain signal of MCC-MCC bilayer tablets with tamping force of 0 (a), 1 (b), 3 (c), 5 (d), and 7 (e) kN.....	133
Figure 5.52: Layer interface reflection intensity maps of MCC-MCC bilayer tablets with tamping force of 0 (a), 1 (b), 3 (c), 5 (d), and 7 (e) kN.....	133
Figure 5.53: Terahertz pulse reflection shape of refractive change in media from low to high (a) and high to low (b).....	134
Figure 5.54: Simulated individual reflection shapes (a, c, d) and the overall combined reflection shapes (b, d, f) at the interface for MCC-MCC, MCC facing MCC-Lac, and lactose facing MCC-Lac bilayer tablets, respectively.....	137
Figure 5.55: Refractive index spectra of pure lactose monohydrate and MCC tablets. ....	138
Figure 5.56: Surface images of the bottom half of the MCC-Lac bilayer tablets with tamping force of 0 (a), 1 (b), 3 (c), 5 (d), and 7 (e) kN tamping force after the tensile strength test .....	138
Figure 5.57: Surface images of the bottom half of the MCC-Lac bilayer tablets with tamping force of 1 (a), 3 (b), 5 (c), and 7 (d) kN tamping force after the tensile strength test.....	139
Figure 5.58: Breaking force versus tamping force and reflectance versus tensile strength for both MCC-Lac and MCC-MCC bilayer tablets. ....	140
Figure A.59: Coating thickness images of one tablet at each sampled coating time point measured by terahertz .....	157
Figure A.60: Weight gain based coating thickness and terahertz based coating thickness trend with coating time. Error bars represent lab uncertainty.....	158
Figure A.61: Raw NIR spectra (a) and SNV processed NIR spectra (b) compared with offset pure HPMC and lactose monohydrate NIR spectrum.....	161
Figure A.62: First two latent variables for the terahertz based coating thickness model compared with offset pure HPMC and lactose monohydrate NIR spectrum .....	162
Figure A.63: Weight gain based coating thickness model without moisture correction (a), weight gain based coating thickness with moisture correction (b), and terahertz based coating thickness (c) models.....	163
Figure A.64: Averaged weight gain based coating thickness model without moisture correction (a), weight gain based coating thickness with moisture correction (b), and terahertz based coating thickness (b) models .....	164

## **Chapter 1: Introduction**

### **1.1. Statement of the problem**

The pharmaceutical industry produces a wide range of drug products; however, the tablet remains the most prevalent dosage form. The tablet manufacturing process often includes unit operations that generate pharmaceutical compacts (i.e. roller compaction and tablet compaction). The critical quality attributes (CQA) of these compacts are generally characterized during processing to enhance product quality and improve process understanding. A measure of the ability of the compact to withstand mechanical stress (i.e. mechanical strength) is an important CQA. The mechanical strength of a pharmaceutical compact often influences the dissolution and disintegration times of the final product.<sup>1-5</sup> In addition, an appropriate level of mechanical strength is required for tablets to withstand shipping, handling, and downstream processing. This study investigated the measurement of refractive index as an indicator of mechanical strength.

Refractive index is an optical property that describes the relative speed of light through a medium. This property is potentially correlated to mechanical strength due to its dependence on porosity.<sup>6</sup> The most common technique used to measure refractive index is a refractometer. However, this technique is primarily applicable to liquid systems. Refractive index measurements for pharmaceutical solids are more challenging owing to their complexity (*i.e.* dimension, solid state, crystal form, number of components, *etc.*). Recent advancements in terahertz time of flight spectroscopy (THz-TOF), however, provides potential process analytical technology (PAT) capabilities for measuring refractive index.<sup>7-9</sup>

Terahertz time of flight spectroscopy operates in the far-infrared region of the electromagnetic spectrum (300 GHz–3 THz or 10-100  $\text{cm}^{-1}$ ). In this technique, the solid sample is impinged with a coherent terahertz pulse. A time gated detector collects either the reflected or transmitted time domain signal based on the mode of operation. The refractive index spectrum is then obtained with appropriate application of Fourier transform followed by normalization with frequency and sample thickness.

A number of pharmaceutical applications<sup>2, 10-23</sup> benefit from refractive index measurements from THz-TOF; however, there are few literature examples<sup>24, 25</sup> for mechanical strength. Most traditional mechanical strength methods (i.e. tensile strength tests, hardness, friability) require application of mechanical stress, often until mechanical failure. Therefore, further material testing is precluded. In addition, the destructive and often timely nature of traditional methods eliminate the capability for real-time monitoring. The objective of this thesis was to demonstrate that rapid and non-destructive refractive index measurements from THz-TOF can indicate mechanical strength measurements from various destructive tests. Achieving this goal with complex tablet systems provided further support for THz-TOF as a potential PAT tool for roller and tablet compaction unit operations.

## 1.2. Hypothesis and Specific Aims

The central hypothesis of this dissertation is the following:

*Refractive index measurements from terahertz time of flight spectroscopy are directly related to porosity; therefore, these nondestructive measurements are able to correlate to the mechanical strength of pharmaceutical compacts.*

To test this hypothesis, four specific aims were performed.

Specific Aim 1: Evaluate robustness of a refractive index based porosity model against chemical composition and process parameters

This thesis investigated the relationship between refractive index and mechanical strength.

However, this relationship is based on the dependence of refractive index to porosity. Therefore, this specific aim further confirmed this basis with evaluating multicomponent tablet systems with chemical and process parameter variations.

Specific Aim 2: Development of refractive index based radial tensile strength model.

The radial tensile strength of a tablet is a common measurement which determines the mechanical strength. These measurements are generally performed using a destructive diametrical compression test. This specific aim demonstrated that nondestructive refractive index measurements are able to correlate with radial tensile strength for multicomponent tablet systems having a constant chemical composition.

Specific Aim 3: Development of refractive index based hardness model for intra tablet mechanical strength assessment

Indentation hardness is another measurement determining an aspect of mechanical strength of pharmaceutical compacts. These measurements are advantageous due to its capability of providing intra tablet assessment of mechanical strength. This specific aim demonstrated the first example of generating hardness maps nondestructively with spatially resolved refractive index measurements for pure component tablets.

Specific Aim 4: Investigation of the relationship between terahertz pulse reflections at the layer-to-layer interface and axial tensile strength for bilayer tablets.

Mechanical failure in a bilayer tablet often occurs at the layer-to-layer interface. Axial tensile strength tests are an option to evaluate the interfacial strength. This specific aim evaluated the refractive index changes at the layer-to-layer interface and related them to axial strength test.

### **1.3. Literature Review**

Refractive index is an optical property that describes the relative speed of light through a medium. The density and crystalline structure of the material dictate its refractive index, thus, allowing for correlation with physicochemical properties.<sup>6</sup> As a result, multiple pharmaceutical applications benefit from refractive index analyses of both pharmaceutical liquid<sup>10-17</sup> and solid<sup>18-21</sup> systems.

For liquid systems, the primary method used for measuring the refractive index is refractometry. Refractometers measure the degree an incident light bends when traveling through a liquid sample. A common refractometer is the Abbe refractometer. It uses a sodium D line light source at a wavelength of approximately 589 nm, however, other types of liquid refractometers also exist.<sup>26</sup> Liquid refractometry is also a very common high performance liquid chromatography detector.<sup>27-31</sup> The wide availability and ease of use of these refractometers has expanded refractive index applications for liquid systems ranging from counterfeit drug detection<sup>11, 13</sup> to biomaterial analysis<sup>12, 17</sup>.

In contrast, refractive index measurements of pharmaceutical solids are more challenging owing to their complexity (*i.e.* dimension, solid state, crystal form, number of components, *etc.*). This thesis added new refractive index measurement applications for assessing the mechanical strength of complex pharmaceutical solids with THz-TOF. This chapter reviews additional refractive index measurement methods for pharmaceutical solids and evaluates existing pharmaceutical applications for refractive index of solids in literature.

### **1.3.1. Theory**

#### **1.3.1.1. Refractive Index Definition**

Refractive index is a measure of the amount of deviation a ray of light undergoes as it impinges upon a new medium. Figure 1.1 shows an incident ray being refracted inside a new medium. According to Snell's law, if the angle of incidence ( $\theta_i$ ) and the angle of refraction ( $\theta_r$ ) is known then the refractive index ( $n$ ) is defined by Equation 1. In addition to a change in angle, the light velocity also changes between two media/phases, therefore, refractive index is also expressed as

the ratio of phase velocity of the first medium ( $v_i$ ) to phase velocity of the second medium ( $v_r$ ) (Equation 2). Generally, one medium is ambient air in which the phase velocity is approximately the speed of light ( $c$ ), thus yielding Equation 3 where ' $v_p$ ' is the phase velocity of the second medium. Snell's law applies to optically isotropic systems such as gases, liquids, amorphous solids, and crystalline materials having cubic symmetry, as the phase velocity and refractive index is equal in all directions.

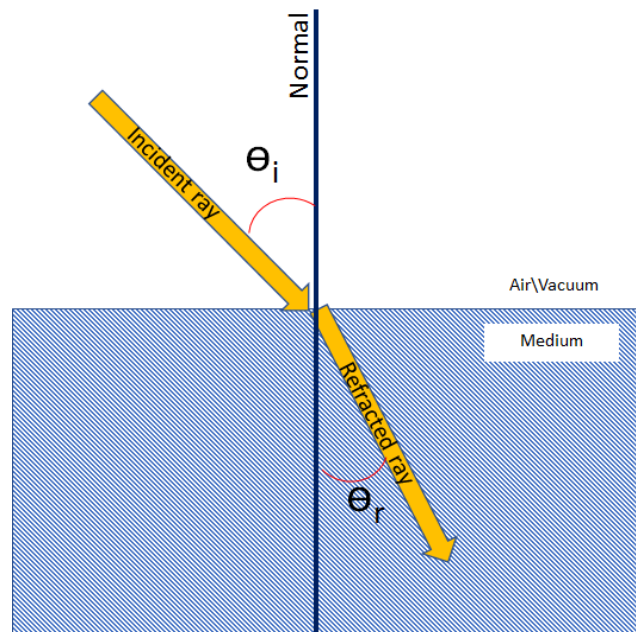


Figure 1.1: Schematic of light refracting in a denser medium

$$n = \frac{\sin \theta_i}{\sin \theta_r} \quad (1)$$

$$n = \frac{v_i}{v_r} \quad (2)$$

$$n = \frac{c}{v_p} \quad (3)$$

### 1.3.1.2. Refractive Index in Optically Anisotropic Systems

The refracted rays produced in optically anisotropic systems have direction dependent phase velocities. Considering a crystal having trigonal symmetry (*i.e.* calcite) in Figure 1.2, the refraction of the unpolarized light yields two rays: the ordinary ray and the extraordinary ray. Ordinary rays vibrate perpendicular to the optical axis and obey Snell's law, while extraordinary rays vibrate in the same direction of the optical axis and do not obey Snell's law, as the phase velocity is dependent on the direction. The optical axis is defined as the direction in which all the possible refracted rays travel in the same direction with the same speed. Crystals with trigonal, hexagonal, and tetragonal symmetries have only one optical axis and are referred to as optically uniaxial. However, almost all pharmaceutically relevant materials (*i.e.* small molecule organic crystals) are biaxial crystals. Optically biaxial crystals (*i.e.* orthohombic, monoclinic, and triclinic crystals) include two optic axes. In contrast to optically uniaxial crystals, optically biaxial crystals yield two extraordinary rays after the incident light undergoes refraction.<sup>32</sup>

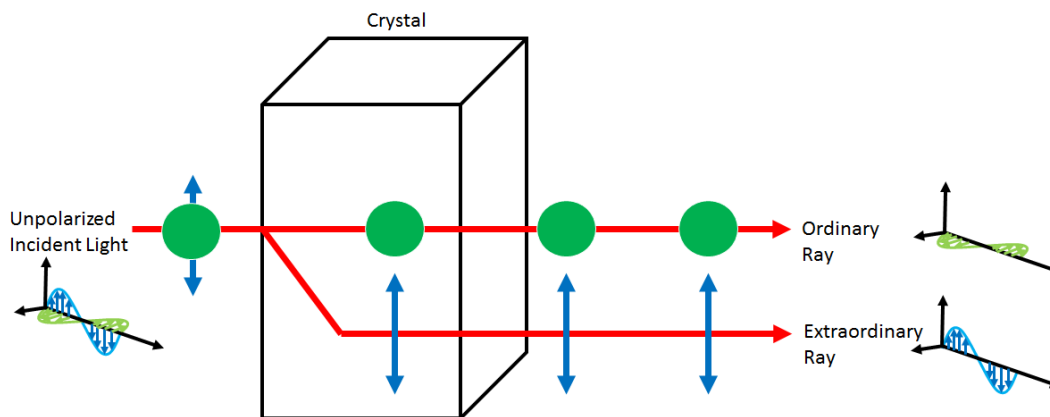


Figure 1.2: Schematic of light refracting in a denser medium

The double refraction caused by optically anisotropic systems introduces challenges in calculating one refractive index value for the medium. In optically uniaxial crystals, there is a refractive index representative of both the ordinary ray ( $n_o$ ) and the extraordinary ray ( $n_e$ ). The difference between these refractive indices is referred to as birefringence. For optically biaxial crystals there are two extraordinary rays, however, there are three principal refractive indexes ( $n_\alpha$ ,  $n_\beta$ , and  $n_\gamma$ ).<sup>32</sup> This is due to the presence of three different principal planes in which one plane incorporates the optical axis. According to Batsanov *et al.*<sup>6</sup>, the average refractive index for both optically uniaxial ( $\bar{n}_{OU}$ ) and optically biaxial ( $\bar{n}_{OB}$ ) crystals can be calculated by Equation 4 and Equation 5.

$$\bar{n}_{OU} = \sqrt[3]{n_e n_o^2} \quad (4)$$

$$\bar{n}_{OB} = \sqrt[3]{n_\alpha n_\beta n_\gamma} \quad (5)$$

### 1.3.1.3. Refractive Index Based on Electromagnetic Parameters

The refractive index is also defined in terms of the electromagnetic parameters of the material.<sup>33</sup>

The electric field strength ( $\vec{E}$ ) of an electromagnetic plane wave propagating through a material in the 'z' direction is given in Equation 6. This traveling wave is defined by an amplitude ( $\vec{E}_0$ ), an angular frequency ( $\omega$ ), and a propagation constant ( $k$ ). According to Equation 2, refractive index is the ratio of phase velocities. The phase velocity is related to the propagation constant and angular frequency by Equation 7.

$$\vec{E} = \vec{E}_0 e^{i(\omega t \pm kz)} \quad (6)$$

$$v_p = \frac{\omega}{k} \quad (7)$$

The conductivity ( $\sigma$ ), permittivity ( $\epsilon$ ), and permeability ( $\mu$ ) of the material dictates the phase velocity of the wave. Permittivity and permeability represent the alignment of the electric and

magnetic dipoles respectively in a material with respect to an applied electric field. Conductivity is indicative of the electric current flow through the material, which is zero for dielectric materials and in free space. These coefficients (electromagnetic parameters) relate the material to electric and magnetic fields through material equations shown in Equations 8-10; where ' $\vec{J}$ ', ' $\vec{D}$ ', ' $\vec{B}$ ', and ' $\vec{H}$ ' are the current density, electric flux density, magnetic flux density, and magnetic field strength respectively.

$$\vec{J} = \sigma \vec{E} \quad (8)$$

$$\vec{D} = \epsilon \vec{E} \quad (9)$$

$$\vec{B} = \mu \vec{H} \quad (10)$$

The phase velocity defined in terms of electromagnetic parameters is seen in Equation 11. The permittivity ( $\epsilon_0$ ) and permeability ( $\mu_0$ ) of free space are constant having values of  $8.854 \times 10^{-12}$  F/m and  $4\pi \times 10^{-7}$  H/m, respectively. Substituting these constants into Equation 11 results in the phase velocity of free space or speed of light (Equation 12).

Refractive index is then defined by Equation 13 after appropriate substitution of Equation 3 with Equation 11 and Equation 12. Electromagnetic parameters are more commonly represented as relative to free space as seen in Equation 14 and 15 where ' $\epsilon_r$ ' and ' $\mu_r$ ' are relative permittivity and relative permeability respectively. Refractive index definition in terms of relative permittivity is seen in Equation 16 assuming the medium is non-magnetic (relative permeability equals one).<sup>34</sup>

$$v_p = \frac{1}{\sqrt{\epsilon\mu}} \quad (11)$$

$$c = \frac{1}{\sqrt{\epsilon_0\mu_0}} \quad (12)$$

$$n = \sqrt{\frac{\epsilon\mu}{\epsilon_0\mu_0}} \quad (13)$$

$$\epsilon_r = \frac{\epsilon}{\epsilon_0} \quad (14)$$

$$\mu_r = \frac{\mu}{\mu_0} \quad (15)$$

$$n = \sqrt{\epsilon_r} \quad (16)$$

Electromagnetic parameters are also complex; therefore, refractive index is further represented in complex form. Equation 17 provides the complex form for both relative permeability and refractive index ( $\tilde{n}$ ), where ' $\epsilon_r$ ' and ' $n_r$ ' are the real parts, while ' $\epsilon_i$ ' and ' $n_i$ ' are the imaginary parts of the permittivity and refractive index, respectively. The real part of the refractive index represents the speed of light through the medium, while the imaginary part represents light absorption; thus, both parts provide complimentary optical information of solid samples.

$$\tilde{n} = n_R - in_i = \sqrt{\epsilon_R - i\epsilon_i} \quad (17)$$

#### 1.3.1.4. Dispersion Effect on Refractive Index

The amount of refraction occurring when light interacts with a sample is dependent on the frequency/wavelength of the light (*i.e.*, dispersion). Cauchy established an empirical dispersion

law (Equation 18) relating refractive index with the wavelength of light ( $\lambda$ ) by a set of empirical parameters (A, B, C).<sup>35, 36</sup> Other empirical models for refractive index also exist.<sup>37-40</sup> A major limitation of these models is the lack of physical meaning behind the empirical parameters. In addition, they are not generally applicable to metals and semiconductors.

$$n(\lambda) = A + \frac{10^4 B}{\lambda^2} + \frac{10^9 C}{\lambda^4} \quad (18)$$

The refractive index and the frequency of light is also related to electronic theory (*i.e.*, Drude model).<sup>6, 33</sup> This model defines the square of the refractive index in terms of electron density (N), the electron charge ( $q_e$ ), the electron mass ( $m_e$ ), the electron's resonant frequency within the material ( $\omega_0$ ), and the frequency of the light ( $\omega$ ) (Equation 19). The assumptions of this model include no interaction between electrons and that the velocity/direction change of an electron after collision is only dependent on temperature and not previous motion of the electron.

$$n^2(\omega) = 1 + \frac{Nq_e^2}{\epsilon_0 m_e (\omega_0^2 - \omega^2)} \quad (19)$$

## 1.3.2. Methods to Determine Refractive Index of Solids

### 1.3.2.1. Prism Methods

Measurements of refractive index can be precisely made on a prism. Figure 1.3 shows a prism with a ray of light directed towards one face. The incident light is refracted once it enters the prism due to the refractive index change from ' $n_m$ ' to ' $n$ ' (Figure 1.3). The refracted light

changes direction again, while exiting the prism. One option of measuring refractive index is by setting the angle of incidence ( $\theta_i$ ) and exit angle ( $\theta_e$ ) equal. This results in the angle of deviation ( $\theta_d$ ) to be at a minimum (angle of minimum deviation ( $\theta_{md}$ )). The angle of minimum deviation is determined by plotting different angle of incidence, controlled precisely with goniometer, against angle of deviation and locating the minimum (Figure 1.3b). The prism angle ( $\theta_p$ ) and angle of minimum deviation is used to determine the refractive index of the prism by Equation 20 assuming the outside medium is air ( $n_m$  equal to 1).<sup>41-46</sup>

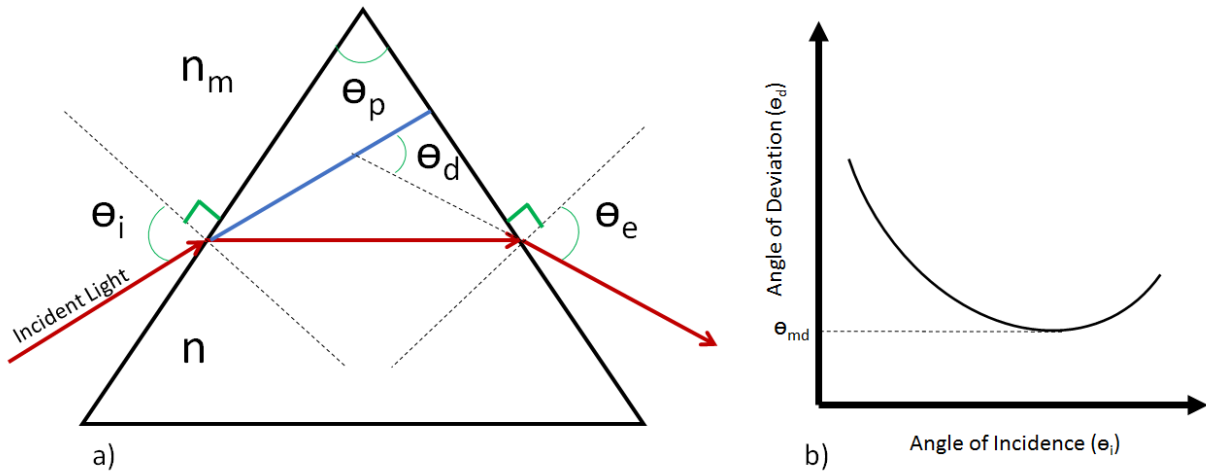


Figure 1.3: prism deviation method (a) and the corresponding angle of deviation versus angle of incidence plot (b)

Angle of deviation, however, can be experimentally challenging to measure. Therefore, Bass *et al.*<sup>42</sup>, proposed to calculate refractive index with angle of incidence, prism angle, and exit angle measurements (Equation 21). In addition, the authors claimed that least-squares method determines the refractive index accurately by measuring multiple angle of incidences along with their respective exit angles.

$$n = \frac{\sin\left(\frac{\theta_p + \theta_d}{z}\right)}{\sin\left(\frac{\theta_p}{z}\right)} \quad (20)$$

$$\theta_e = \sin^{-1}\left(n * \sin\left(A - \left(\sin^{-1}\left(\frac{\sin(\theta_i)}{n}\right)\right)\right)\right) \quad (21)$$

These two prism methods for determining refracted index are based on analysis of the transmitted light ray through the prism. The measurement accuracy of these methods is affected adversely by internal reflections. Therefore, an alternate approach to measuring refractive index is by using the specific angle of incidence that results in a 90 degrees refracted angle (critical angle of incidence (Equation 22)).<sup>47-49</sup> Analysis of the reflected beam power is an option to determine this critical angle. Refractive index of the sample is defined in terms of the critical angle of incidence by Equation 23. Detailed derivation is found in literature.<sup>47</sup>

$$\theta_i^{crit} = \sin^{-1}(n) \quad (22)$$

$$n^2 = \frac{4}{3}\left(1 + \sin(\theta_i^{crit}) + \sin^2(\theta_i^{crit})\right) \quad (23)$$

Refractive index of both isotropic and anisotropic crystals can be measured with these prism methods. Isotropic crystals require no special prism orientation unlike anisotropic crystals. For uniaxial crystals the plane of the prism that the light is incident upon must contain the optical axis. This orientation causes the incident light to refract into ordinary and extraordinary rays. Measurements of the deviation angle for each of the two rays is then used to determine the two principle refractive indices. To simplify this procedure, the incident light is polarized before

contacting the prism to allow only one of the refracted rays to be present. For biaxial crystals, refractive index measurements are more challenging as refractive index measurement of more than one prism is needed, where each prism is oriented along a different coordinate plane with respect to the incident light. In the literature<sup>42, 43</sup>, refractive index values of several isotropic and anisotropic crystals with prism methods are available.

Prism methods have major limitations in addition to challenges associated with measuring anisotropic crystals. A significant limitation is that the sample needs to be in the form of a prism. In addition, the prism angle needs to be less than the critical prism angle (Equation 24) at which the incident light does not pass through the prism (*i.e.*, total internal reflection), thus, creating a size limitation for the sample.<sup>42</sup> Therefore, there is little flexibility in the shape and size of the sample for refractive index measurements.

$$\theta_p^{crit} = 2\sin^{-1}\left(\frac{1}{n}\right) \quad (24)$$

Two options of overcoming the shape and size limitations are sample immersion or prism coupling. Bass *et al.*<sup>42</sup>, immersed solid prism samples into a liquid medium to allow for greater prism size flexibility. The increase in prism size range is due to the increase in refractive index (compared to atmospheric air) of the immersed liquid medium. As a result, the critical prism angle increases according to Equation 24. The authors successfully measured Ni<sub>2</sub>SiO<sub>4</sub> crystals using the prism immersion approach. Watanabe *et al.*<sup>18</sup> also used an immersion-based approach to determine refractive index of multiple crystalline drugs such as aspirin. The prism size concern is addressed with the immersion methods; however, it does not fully consider restriction of sample shape.

The prism coupling method improves samples shape flexibility, thus, providing measurements of bulk samples.<sup>50</sup> The procedure for this method includes mounting the polished side of a sample material onto a tent-shaped prism of known refractive index. A light beam is then directed towards the non-mounted prism face. The light beam is refracted into the prism and then internally reflected at the base where the solid material is mounted. This reflected light is again refracted once it encounters the other non-mounted surface and exits the prism. A photo-detector is located on the side of the prism where the light beam exits. The angle of incidence is adjusted until total reflection occurs at the prism and sample interface. This is determined by monitoring the power of the light that exits the prism with the photo-detector. The refractive index is determined with Equation 25 where ‘ $\alpha$ ’ and ‘ $\varepsilon$ ’ are the specific angle of incidence and exit angle at which this total prism base reflection occurs, and ‘ $n_p$ ’ is the known refractive index of the prism. The refractive index measurement accuracy from the prism coupling approach is comparable to the minimum deviation method. However, intimate contact needs to be maintained with sample and prism and total internal reflection needs to occur at sample and prism interface (*i.e.*, no light loss due to sample) for accurate measurements.

$$n = \sin \alpha \cos \varepsilon + (n_p^2 - \sin^2 \alpha)^{0.5} \sin \varepsilon \quad (25)$$

Prism methods offer a means to accurately measure refractive index of solids with a relative error of approximately  $10^{-6}$ .<sup>6</sup> However, pharmaceutical solids are complex, as many are anisotropic crystals requiring additional effort to obtain accurate refractive index measurements based on prisms. In addition, it is difficult to meet the size and shape requirements for most of

these methods. Therefore, additional methods may need to be considered based on the complexity of the solid system.

### **1.3.2.2. Interferometric Methods**

Applications for interferometers include measurement of refractive index and sample thickness. These measurements are made by analysis of interference (fringe) patterns.<sup>51</sup> The Michelson interferometer is commonly used for this purpose.<sup>6, 52</sup> A schematic of this instrument is illustrated in Figure 1.4. The instrument includes a light source, beam splitter, compensation plate, two mirrors, and a charge couple detector (CCD) detector (or screen).

The procedure for obtaining refractive index measurements with a Michelson interferometer involves first sending a ray of light to the beam splitter (Figure 1.4). The beam splitter refracts the incident light. The light exiting on the opposite side of the beam splitter travels towards Mirror 1 (arm 1). There is also some light which undergoes internal reflection inside the beam splitter. This internally reflected light travels toward Mirror 2 (arm 2). The two mirrors reflect the light back towards the beam splitter where the two light rays interact before they reach the detector. There is a compensation plate in between the beam splitter and Mirror 1 to account for the additional distance traveled by the internally reflected light in the beam splitter from arm 2.

The solid sample is placed in between Mirror 2 and the beam splitter. The refractive index is assessed by analysis of fringe patterns from the detector.

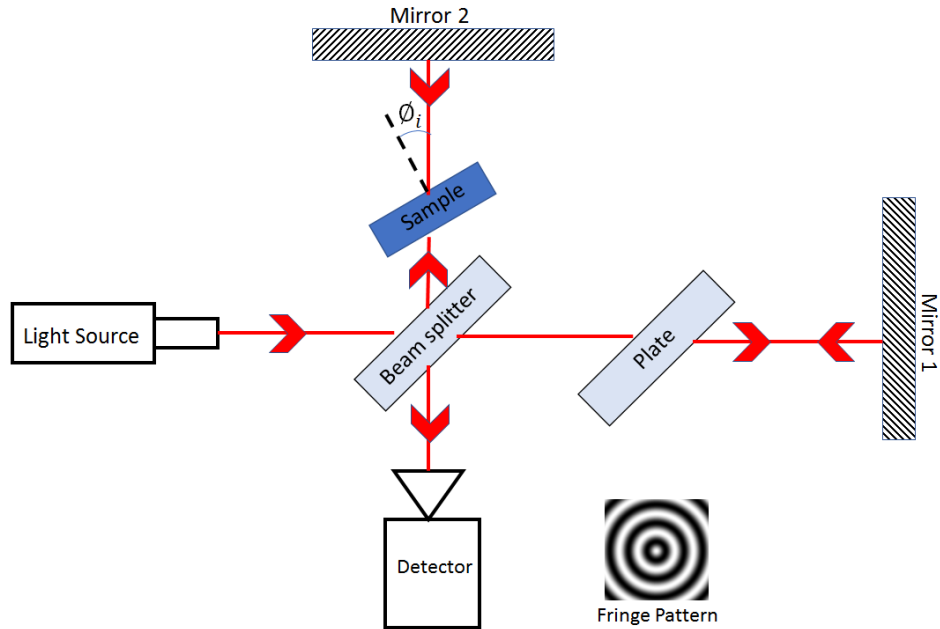


Figure 1.4: Michelson interferometer schematic

An example of a fringe pattern is also shown in Figure 1.4. These patterns vary with phase change in both arms of the interferometer.<sup>52</sup> The phase change in arm 1 and arm 2 is defined in Equation 26 and 27 respectively in terms of the sample thickness ( $d$ ), the angle formed between light coming from mirror 2 and surface of sample (incidence angle ( $\phi_i$ )), the angle the light refracts inside the sample (refraction angle ( $\phi_r$ )), the wavelength of light ( $\lambda$ ), and the refractive index of the sample ( $n$ ). Since there is no sample in arm 1, there is no light refraction that occurs, as indicated in Equation 27. The phase difference ( $\Delta$ ) between the two split rays is then defined as the difference between the phase change in each arm (Equation 28). A factor of two is present in Equation 28 to account for the light ray passing through the beam splitter twice. The incident angle and the refraction angle are zero when the sample is mounted normal with respect to the light ray. This results in an initial phase difference ( $\Delta_0$ ) defined in Equation 29. The number of

fringes ( $m$ ) indicates the change in phase difference between sample set at specified incidence angle and sample oriented normal to the light ray (Equation 30).

The number of fringes is used to calculate refractive index. Equation 31 defines the number of fringes in terms of the sample thickness, the wavelength of light, the refractive index of the sample, the incidence angle, and the refraction angle. The refraction angle is defined in terms of the incidence angle and the refractive index of the sample according to Snell's law (Equation 32). After appropriate substitution of the refraction angle in Equation 29, the refractive index is solved numerically.

$$PhaseChangeArm1 = \frac{2\pi d \cos(\phi_i - \phi_r)}{\lambda \cos(\phi_i)} \quad (26)$$

$$PhaseChangeArm2 = \frac{2\pi nd}{\lambda \cos(\phi_i)} \quad (27)$$

$$\Delta = 2(PhaseChangeArm1 - PhaseChangeArm2) \quad (28)$$

$$\Delta_0 = 2\left(\frac{2\pi nd}{\lambda} - \frac{2\pi d}{\lambda}\right) \quad (29)$$

$$\Delta - \Delta_0 = 2\pi m \quad (30)$$

$$m = \frac{2d}{\lambda} \left[ n \left( \frac{1}{\cos(\phi_r)} - 1 \right) + 1 - \frac{\cos(\phi_i - \phi_r)}{\cos(\phi_r)} \right] \quad (31)$$

$$\sin(\phi_i) = n \sin(\phi_r) \quad (32)$$

The Michelson interferometer has been used to measure refractive index of several different solids.<sup>53-56</sup> This method has advantages over the prism methods based on internal reflections because there is no concern of loss of light due to absorption from sample.<sup>6</sup> This is because the path length of the light for interferometric method is measured. However, the relative error of the Michelson interferometer method (approximately  $10^{-3}$ ) is orders of magnitude higher than prism method potentially owing to environmental perturbations.<sup>6</sup>

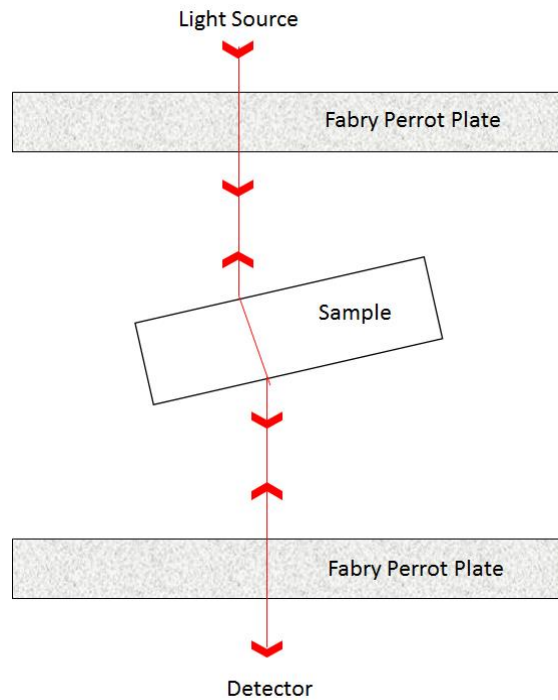


*Figure 1.5: Fabry Perrot interferometer schematic*

One option to enhance measurement accuracy is by using Fabry Perrot interferometer.<sup>57, 58</sup> The clarity of the fringe patterns created by Michelson interferometer are sensitive to environmental conditions such as moisture and air flow. However, Fabry Perrot interferometer typically produces more stable fringe patterns that are less susceptible to environmental perturbations, due to path length duplication. The setup of a Fabry Perrot interferometer (Figure 1.5) involves placing solid sample between two Fabry Perrot plates. The light source and detector are placed

on opposite ends. Reflections from the Fabry Perrot plate allow portions of the light ray to re-enter and exit the sample again. Phase difference between these multiple reflections is then used to calculate the refractive index. Results from Coppola *et al.*<sup>59</sup> showed that the Fabry Perrot interferometer determined refractive indices with a relative error of approximately  $10^{-4}$ . Choi *et al.*<sup>60</sup> demonstrated further improvement of relative error to approximately  $10^{-5}$  using Fabry Perrot interferometer modified to include two lasers. In addition, the combination of Fabry Perrot and Michelson interferometers have also been studied for improving refractive index measurements.<sup>56</sup> Fabry Perrot interferometers improve refractive index measurements, however, the relative error is still higher than prism methods ( $\sim 10^{-6}$ ).

All interferometric methods for refractive index measurements have additional common sources of error. These measurements are highly sensitive to sample thickness and require transmittal of light through the sample. Therefore, the interferometric methods are appropriate for transparent plate shaped solid samples with a precisely characterized thickness.

### **1.3.2.3. Ellipsometric Methods**

Ellipsometry is a technique for measuring thickness and optical constants (*i.e.*, refractive index) of thin films. These measurements are also made using an interferometer. However, ellipsometers allow refractive indices to be measured without sample thickness information and with a relative error of approximately  $10^{-3}$ .<sup>61</sup> In addition, ellipsometers measures refractive index of much thinner films (<10 nm) than interferometers.<sup>62, 63</sup> These advantages arise from analysis of light reflection from a sample.

Ellipsometry is specifically the analysis of the change in polarization of light that occurs before and after sample reflection.<sup>63</sup> Initially, the light from the source is linearly polarized with a polarizer. The linearly polarized light is an electric field vector containing two components. These two components are waves that are parallel ( $\pi$ -wave) and perpendicular ( $\sigma$ -wave) to the plane of incidence. The linearly polarized light reflects from the sample causing shifts in the  $\pi$ -wave and  $\sigma$ -wave (Figure 1.6). The resulting reflected light is elliptically polarized. An analyzer is present after the light reflection to convert the elliptically polarized light back to linearly polarized light. A detector at the end records the intensity of the light. This specifically described ellipsometer is a photometric ellipsometer shown in Figure 1.7;<sup>63</sup> other types of ellipsometers are also used.<sup>64</sup>

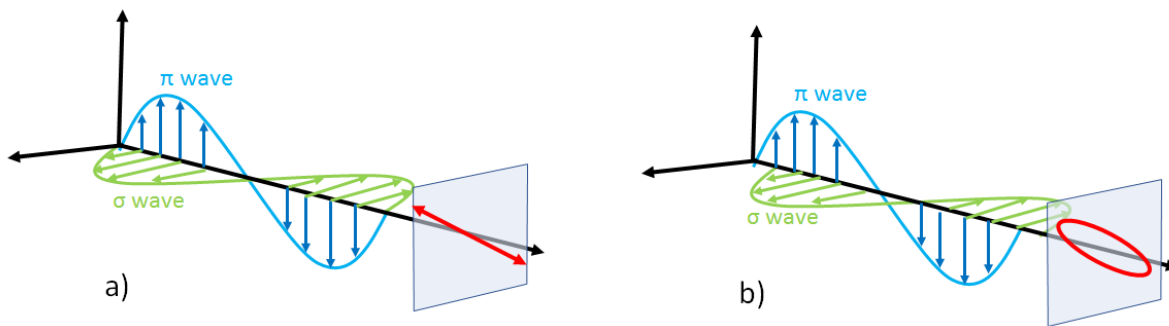


Figure 1.6: Linearly polarized light (a) and elliptically polarized light (b)

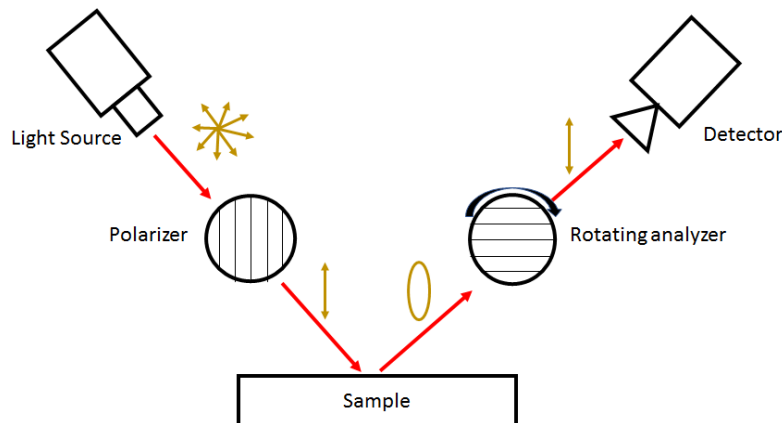


Figure 1.7: Photometric ellipsometer schematic

The primary information obtained from an ellipsometer is the amplitude ratio ( $\Psi$ ), phase difference ( $\Delta$ ), and polarization change ( $\rho$ ). The amplitude ratio and phase difference are with respect to the  $\pi$ -wave and  $\sigma$ -wave associated with the reflected elliptically polarized wave. The polarization change of the light before and after surface reflection is defined in terms of the amplitude ratio and phase difference by Equation 33. The refractive index is determined from these ellipsometric parameters.<sup>63, 64</sup>

$$\rho = \tan(\Psi)e^{j\Delta} \quad (33)$$

$$\rho = \frac{\rho_\pi}{\rho_\sigma} \quad (34)$$

The refractive index is linked to polarization change by considering Fresnel reflection coefficients. These coefficients represent the reflection power of the incident light due to the sample for  $\pi$ -wave ( $\rho_\pi$ ) and  $\sigma$ -wave ( $\rho_\sigma$ ) and their ratio defines the polarization change (Equation 34). The definitions of these coefficient are shown in Equations 35 and 36 where ' $\theta_0$ ', ' $\theta_1$ ', ' $\tilde{n}_0$ ', and ' $\tilde{n}_1$ ' are the angle of incidence, the angle between transmitted light and normal, the complex refractive index of initial medium (air), and the complex refractive index of the sample respectively. Complex refractive index of the sample is solved using Equation 37; which is derived from Equations 33-36 and Snell's law. The calculated complex refractive index is wavelength specific.<sup>63</sup>

Alternatively, amplitude ratio can be plotted against phase difference at unique incident angles, polarizer setting, and/or analyzer setting to determine refractive index. Researchers have demonstrated refractive index and thickness estimations through fitting these ellipsometric parameters with empirical models.<sup>62, 65</sup> These empirical models include Cauchy model and

Lorentz oscillator model, in which the Lorentz oscillator model is more accurate at higher wavelength range.<sup>65</sup>

$$\rho_{\pi} = \frac{\tilde{n}_1 \cos(\theta_0) - \tilde{n}_0 \cos(\theta_1)}{\tilde{n}_0 \cos(\theta_0) + \tilde{n}_1 \cos(\theta_1)} \quad (35)$$

$$\rho_{\sigma} = \frac{\tilde{n}_0 \cos(\theta_0) - \tilde{n}_1 \cos(\theta_1)}{\tilde{n}_0 \cos(\theta_0) + \tilde{n}_1 \cos(\theta_1)} \quad (36)$$

$$\tilde{n}_1 = \frac{\tilde{n}_0 \sin(\theta_0) \sqrt{1 - 4 \sin^2(\theta_0) \tan(\Psi) e^{j\Delta} + 2 \tan(\Psi) e^{j\Delta} + \tan^2(\Psi) e^{j\Delta}}}{\cos(\theta_0) [1 + \tan(\Psi) e^{j\Delta}]} \quad (37)$$

Refractive index of several thin films has been measured with ellipsometers.<sup>62, 65-69</sup> Lariviere *et al.*<sup>69</sup> used an ellipsometer to assess refractive index inhomogeneity throughout a film. For their system, a titanium dioxide film was deposited onto a transparent glass substrate. The reflection of light occurring at multiple interfaces (*i.e.*, air-to-film interface and film-to-substrate interface) was used to determine refractive index distribution throughout the film with the assumption of a linear refractive index gradient for a homogenous film. This information can be used to optimize the film preparation process (*i.e.*, substrate temperature) to achieve optically homogenous films. Synowicki *et al.*<sup>65</sup>, further demonstrated the sensitivity of this technique to material structure by examining indium tin oxide films. This specific material was studied because the film forms with a complex graded microstructure. The study showed a means to optimize transparency of the film by using experimentally fit models (Cauchy model) to determine the appropriate film thickness and refractive index with an ellipsometer. These studies utilized ellipsometric measurements for assessment of the structure of the material; however, the surface structure can have critical effect towards refractive index measurements.

The effect of surface roughness on ellipsometric measurements was studied by Fenstermaker *et al.*<sup>70</sup> In this study, a range of roughness values (0-500Å) along with six substrate materials (glass, silicon, chrome, mercury, gold, and silver) were studied. The authors concluded that large measurement errors were found at roughness values as low as 50Å. Therefore, smooth surfaces are desired to enhance surface reflection and improve ellipsometric measurements.

The light absorption coefficient is also a critical factor to consider before conducting ellipsometric measurements. A study by Al-Ani S *et al.*<sup>67</sup>, reported refractive index and thickness values for vanadium pentoxide. There was a high measurement error attributed to the high absorption coefficient of the material. This measurement error was potentially a result of violating the assumption that the light is not absorbed and therefore only undergoes refraction and reflection, as required by traditional ellipsometry.

Another potential source of error for refractive index measurements of bulk solids with ellipsometry is that this method is primarily a surface measurement. An inhomogeneous solid may have a refractive index gradient within the solid sample. This gradient would not be appropriately characterized by surface measurements from ellipsometry. For bulk refractive index measurements, light transmittance methods are more appropriate.

Ellipsometry is a useful technique to measure refractive index of thin films without knowledge of the thickness of the material. However, these methods provide information of only the sample surface and requires the sample material to reflect appropriately the incident light (without

absorption). Therefore, the ellipsometric measurement accuracy and utility are restricted by the chemical (*i.e.* absorption coefficient) and physical (*i.e.* thickness) properties of the sample.

#### **1.3.2.4. Terahertz Methods**

Optical constants (*i.e.*, refractive index and absorption coefficient) are also measured directly using spectroscopy. Spectrometers assess the change in an incident electric field due to the presence of sample in the beam path. Both Fourier transform spectroscopy (FTS) and terahertz spectroscopy have been used and compared for measurement of optical constants.<sup>71-77</sup> FTS measures the change in field strength (power transmittance/reflectivity) due to the sample. The resulting field strength is directly related to the absorption coefficient. When combined with the Kramers-Kronig relationships, the refractive index is calculated.<sup>78</sup> In contrast, terahertz spectroscopy provides a more direct measurement of the refractive index of a sample.

Terahertz radiation is in the far-infrared region of the electromagnetic spectrum (300 GHz–3 THz or 10-100  $\text{cm}^{-1}$ ). The low frequency radiation induces crystalline phonon vibrations, intermolecular bond vibrations (hydrogen-bonding), and torsion vibrations in samples.<sup>7, 73, 79</sup> These modes make terahertz spectroscopy a powerful tool for characterizing the crystalline properties of solid materials such as polymorphism and crystallinity.<sup>80-82</sup> Technological advancements in terahertz instrumentation have further enhanced the use of this technique.<sup>74</sup> Terahertz pulsed spectroscopy (TPS) utilizes coherent ultrashort (femtosecond time scale) laser pulses allowing for rapid spectral acquisition. The coherent nature of the laser combined with time-gated signal detection enables extraction of both the electric field strength (amplitude) and the field phase information. The additional phase change information of the electric field allows

direct determination of refractive index of the sample; thus, offering an advantage over FTS. Additional advantages of terahertz spectroscopy over FTS are also provided in literature.<sup>71</sup>

Terahertz pulsed spectroscopy in transmittance mode (TAS 7500 IM Advantest, San Jose, CA) is shown in Figure 1.8.<sup>83</sup> This instrument operates by initially producing 1560 nm laser pulse of 50 fs frequency from Laser 1. The laser pulses are directed to a photoconductor, which generates an incident 500 fs pulse. This pulse is directed at the sample where it can be reflected, transmitted, absorbed, or scattered. Another photoconductor collects the transmitted signal along with 1560 nm pulses from Laser 2. Laser 1 and Laser 2 are synchronized with Laser 2 undergoing variable time delay. Another approach to terahertz spectroscopy is to establish the delay by adjusting light path length. Time domain signal is collected when the second photoconductor is simultaneously contacted by the transmitted terahertz pulse and the 1560 nm pulse from Laser 2. Additional modes of setup (*i.e.* reflectance setup) are also available.<sup>7, 73, 84</sup>

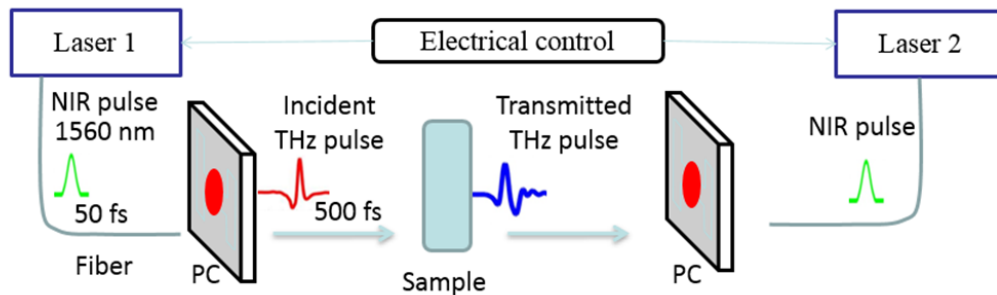


Figure 1.8: Advantest's terahertz pulsed spectroscopy in transmittance setup

The time domain signal obtained from the terahertz spectrometer is a representation of the modification to the electric field by the sample. The electric field at specific time ('t') and light frequency (' $\omega$ ') is defined in terms of the complex refractive index (' $\tilde{n}$ ') and thickness ('x') of the sample according to Equation 38; where  $\vec{E}_0$  is a constant (amplitude).<sup>33</sup> The sample time

domain signal is required to be calibrated before performing further analysis. The calibration process is performed by taking a reference measurement without sample (or air) in the transmittance mode. For the reflectance mode, the reference measurement is performed with a reflective mirror placed at the same position as the sample. An example of sample and reference measurements is shown in Figure 1.9 for transmittance mode. The sample in this Figure is a measurement of a multi component tablet comprising of acetaminophen, microcrystalline cellulose, lactose monohydrate, starch, and magnesium stearate, while the reference is a measurement of air. Time domain signal associated with the tablet is delayed in time due to the large refractive index changes between the air and the tablet and has a lower intensity (compared to the reference signal) due to light absorption, reflection, and scattering. The time delay of the first major peak from the sample data is used to calculate the effective refractive index (Equation 39). The effective refractive index is a measure of the phase delay of the waveguide and is defined in terms of sample thickness, speed of light, and time delay of first peak. Refractive index versus frequency spectrum is determined by taking the ratio of the electric field of the sample ( $E_s$ ) and the reference ( $E_r$ ), which completes the calibration process.

$$\vec{E} = \vec{E}_0 e^{i\omega\left(\frac{x\tilde{n}}{c} - t\right)} \quad (38)$$

$$n_{eff} = \frac{c\Delta t}{H} + 1 \quad (39)$$

The electric field ratio is also defined in terms of the refractive index and absorption coefficient through Equation 40, where ' $\alpha$ ', ' $x$ ', ' $n$ ', and ' $c$ ' are the absorption coefficient, sample thickness, sample refractive index, and speed of light respectively. Converting the time domain electric field signal into frequency domain by Fourier transform simplifies the extraction of refractive index and absorption coefficient. In the frequency domain, an amplitude and a phase angle are

associated with each frequency. The frequency specific amplitude and phase from both the sample and air is used to determine the absorption coefficient and refractive index with Equations 41 and 42 respectively. An example of absorption coefficient and refractive index over multiple frequencies (absorption and refractive index spectrum) is shown in Figure 1.10 where Taday *et al.*<sup>81</sup> characterized the crystal form of apo-ranitidine with terahertz spectroscopy.

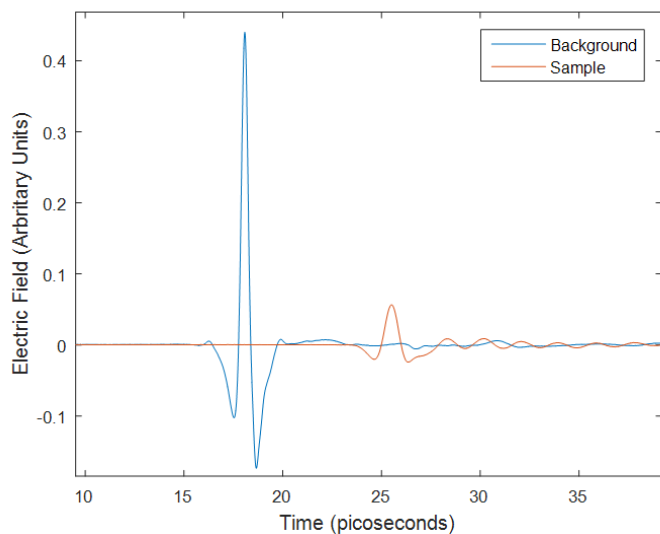


Figure 1.9: Terahertz transmittance time domain spectra of air (a) and tablet sample (b)

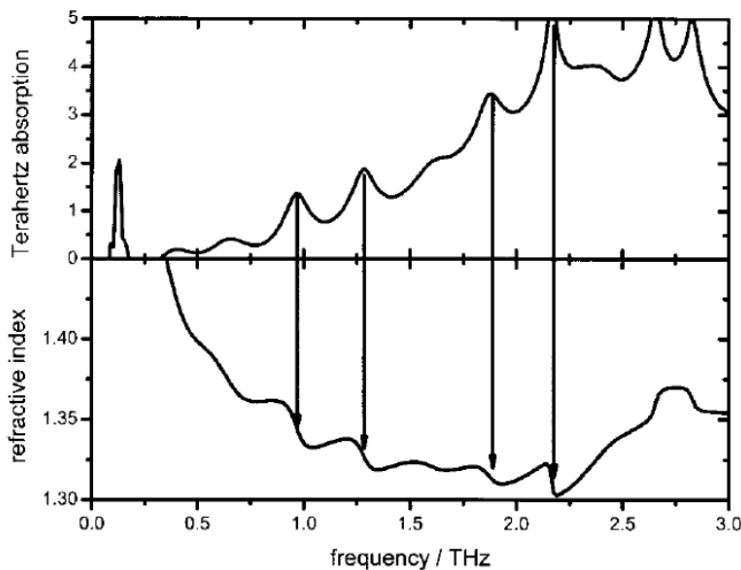


Figure 1.10: Terahertz absorption and refractive index spectrum of Apo-ranitidine<sup>81</sup>

$$\frac{E_s}{E_r} = e^{-\left(\frac{\alpha x}{2} + \frac{i\omega x n}{c}\right)} \quad (40)$$

$$\alpha(\omega) = -\frac{20}{x} \log\left(\frac{|E_{s0}|}{|E_{r0}|}\right) \quad (41)$$

$$n(\omega) = 1 + \frac{c}{x\omega}(\vartheta_{s0} - \vartheta_{r0}) \quad (42)$$

Terahertz spectroscopy offers additional advantages for characterizing solid materials. The low frequency radiation of terahertz waves allows high sample penetration in most media except metals and water.<sup>7</sup> Therefore, terahertz spectrometers are able to measure samples that range in thickness from thin films<sup>85-87</sup> to pharmaceutical tablets.<sup>2, 20, 21, 88, 89</sup> The signal to noise ratio is also very high due to coherent signal detection.<sup>90</sup> In addition, the fast scanning (< 100 ms) time and non-destructive nature allows terahertz spectroscopy to be used for rapid screening and at-line process assessment. These advantages have enhanced the potential for use of terahertz spectroscopy in multiple applications including the pharmaceutical industry.<sup>74</sup>

Terahertz spectroscopy requires specific environmental, sample, and instrument considerations to perform accurate measurements. Most spectroscopic techniques are influenced by sample and environmental moisture.<sup>7, 91, 92</sup> In terahertz spectroscopy, environmental moisture causes critical light absorption and incoherence in the beam path before and after the sample. The presence of water decreases the signal to noise ratio and data interpretability. Therefore, the beam path is purged with dry air or nitrogen.<sup>7</sup> Another option to account for the environmental moisture is placing the terahertz generator and detector close to the sample (minimizing the opportunity to interact with ambient moisture).<sup>93</sup> Current terahertz spectroscopy places limitations on the sample properties. An accurate measurement of sample thickness is required for refractive index

calculations. For optically thick samples (those which the optical density causes too much absorption), transmittance mode is not effective. For these types of samples, reflectance modes are appropriate. Careful consideration is required when taking reference measurements in this mode. The reference spectrum is collected using a reference mirror. The face of the reference mirror must be placed at the exact same position as the face of the sample. Misalignments of as small as 1  $\mu\text{m}$  have the potential to induce significant errors in measurements.<sup>73, 94</sup> Another source of error in transmittance and reflectance terahertz measurements is multiple reflections. During a terahertz scan, a sequence of reflection events occurs; at the terahertz generation and detection region, at the optical window, and at the sample. The resulting time domain signal is a collection of main pulse along with all the reflected pulses. The presence of these multiple reflections decreases the interpretability of a terahertz measurement, especially in the frequency domain. Data processing techniques are available to decrease, but not eliminate, the impact of multiple reflections.<sup>95-98</sup>

Terahertz spectroscopy is a recently developed method to determine refractive index. Advances in instrumentation and data processing facilitate the measurement of the refractive index of samples by terahertz spectroscopy, despite the potential challenges to collecting representative terahertz data. As a result of these advances, combined with the rapidity with which terahertz data is collected, there are a substantial number of applications of refractive index measurements in the pharmaceutical industry.

### 1.3.2.5. Predictive Methods

Refractive indices of many pharmaceutical solids, measured with the previously defined methods, are available in literature (sec 3.1-3.4). However, new compounds are constantly being discovered, which have limited or no available literature values for refractive index. This lack of experimental data leads to investigation of empirical (predictive) relationships to estimate refractive index based on knowledge of the material properties.

Several relationships are available which relate refractive index to density.<sup>6, 99-101</sup> One of the more commonly applied relationship is the Lorenz-Lorentz equation (Equation 43), which assumes a homogenous material with isotropic conductivity. This equation defines specific refraction ('r') of a compound in terms of refractive index ('n') and density ('ρ'). However, it is more practical to represent specific refraction in terms of molecular weight ('M') and molar refraction ('R<sub>D</sub>') as seen in Equation 44. Molar refraction is determined based on the atomic and structural group contributions by summing the product of refraction ('R<sub>i</sub>') and number of atoms ('m<sub>i</sub>') of each element in the compound's chemical formula (Equation 45). A list of element refractions is provided in literature by Eisenlohr<sup>101</sup>. This list was further revised by Vogel<sup>102</sup> to include additional function groups. The Lorenz-Lorentz equation can be rearranged to calculate refractive index in terms of molecular weight, density, and molar refraction (Equation 46).

$$r = \frac{n^2 - 1}{(n^2 + 2)\rho} \quad (43)$$

$$r = \frac{R_D}{M} \quad (44)$$

$$R_D = \sum_i m_i R_i \quad (45)$$

$$n = \sqrt{\frac{M + 2\rho R_D}{M - \rho R_D}} \quad (46)$$

Accurate density measurements are essential to utilize the Lorenz-Lorentz equation. Specifically, the crystal/true density is required. These density values are obtained from calculations or measurements.

For crystal density calculations, crystallographic data such as number of formula units in the crystal unit cell ('Z'), the unit cell volume ('V'), and molecular mass ('M') is used according to Equation 47.<sup>100</sup> However, crystallographic data for new compounds are not routinely available. Therefore, the crystal density is assessed through empirical methods<sup>103</sup> or measured by helium pycnometry.<sup>104</sup>

$$\rho = \frac{1.661ZM}{V} \quad (47)$$

Helium pycnometry measures the pressure difference of helium gas in test cell with and without sample to determine true density. This technique is widely used for determining true density at ambient temperature. However, moisture in the sample introduces measurement error. As a result, the true density measurement accuracy for hydrates and other solid systems containing water is severely reduced. A method based on modified Heckel equation is available to address this moisture concern.<sup>105</sup>

Alternatively, Vogel *et al.*<sup>106</sup> created an empirical approach to determine refractive index without the need of density. For this approach, refraction coefficients for atom and groups (' $M_{n_i}$ ') were listed to determine the total refraction coefficient (' $M_{n_D}$ ') shown in Equation 48. The refractive index was then defined as the ratio of refraction coefficient and molecular mass (Equation 49).

$$M_{nD} = \sum_i m_i M_{n_i} \quad (48)$$

$$n = \frac{M_{nD}}{M} \quad (49)$$

The accuracy of empirical models for refractive index was evaluated by Cao *et al.*<sup>99</sup>. In this study, literature survey was done to locate refractive index of 424 pharmaceutical solids. A subset of 37 compounds were used to compare the mean refractive index of each compound from literature to empirically calculated refractive values from three empirical methods. Variations of the Lorenz-Lorentz equation (Equation 25) were used. The difference in the two methods was the means by which the molar refraction values were calculated; these methods are referred to as the Eisenlohr and Vogel  $R_d$  method. The third empirical method was based on the refraction coefficient (Equation 49) and referred to as the Vogel  $M_{nd}$  method. The model error was evaluated for each empirical method.

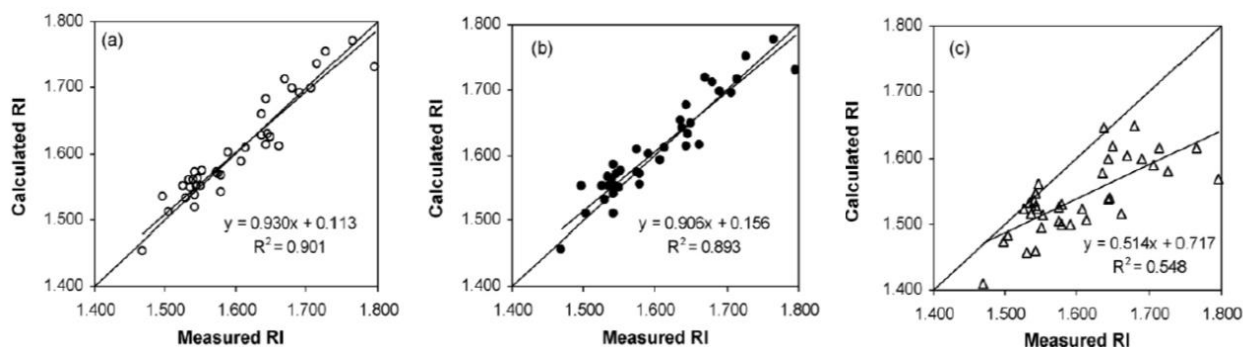


Figure 1.11: The measured versus calculated refractive index plots associated with Einshour (a), Vogel  $R_d$  (b), and Vogel  $M_{nd}$  (c) empirical methods for literature surveyed compounds<sup>99</sup>

The results of each model in the form of predicted versus measured refractive index plots are seen in Figure 1.11. The root mean square error (RMSE) for both the Eisenlohr and Vogel  $R_d$  method were relatively low (0.024 and 0.026 respectively) and were statistically insignificant under 95% confidence interval. However, the Vogel  $M_{nd}$  method, which does not consider density, had an RMSE that was approximately four times greater (0.082) than both the Eisenlohr and Vogel  $R_d$  method. These results imply that density is an important parameter, if not required, for determining refractive index.

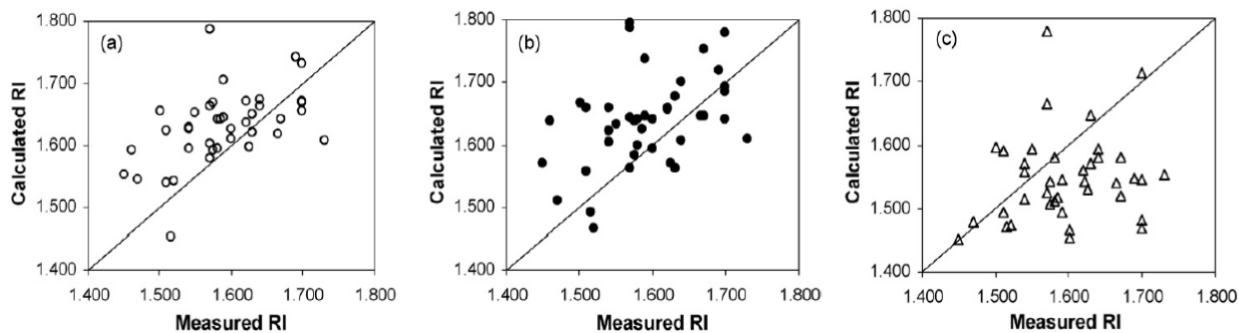


Figure 1.12: The measured versus calculated refractive index plots associated with Einshour (a), Vogel  $R_d$  (b), and Vogel  $M_{nd}$  (c) empirical methods for Pfizer APIs<sup>99</sup>

In addition, Cao *et al.*<sup>99</sup> also evaluated the refractive indices of a number of Pfizer's active pharmaceutical ingredients (API). First, the refractive index of 87 APIs were measured with polarized light microscopy using prism method. A subset of 41 APIs were chosen for empirical modeling.

The model performance for the Pfizer APIs was contradictory to the previous results on compounds, based on the literature survey illustrated in Figure 1.12. The Eisenlohr, Vogel  $R_d$ , and Vogel  $M_{nd}$  method all showed high RMSE values of 0.074, 0.089, and 0.099 respectively.

Vogel  $M_{nd}$  still had the highest RMSE, however, it was statistically similar compared to Vogel  $R_d$  according to the 95% confidence interval.

The high model error for these methods could be attributed to errors in both the measured and calculated refractive indices. The measured refractive index is required to be accurate for modelling purposes. However, the refractive index measurements of Pfizer's API could potentially not be representative. These were exploratory drugs thus their crystal structure and purity may not be well controlled. In addition, only one measurement was made per compound while multiple measurements at different orientations were available for literature survey compounds. Thus, one measurement may not be appropriate as the refractive index measurement is dependent on the orientation for anisotropic crystals. Therefore, the measurement error could be potentially improved by improved controls over the experimental conditions and repeated measurement of the samples.

In addition to model error associated with the measured refractive index, the empirically calculated refractive index can also introduce error. Two out of the three empirical refractive index methods rely on crystal density. According to the Cao's study<sup>99</sup>, a 5% density measurement error results in approximately 3% error in refractive index calculations. This 3% error is significant as it is approximately 0.05 for the refractive index range used in this study (~1.4 to 1.8). The density for all the literature survey compounds were measured while about 40% of the Pfizer APIs had empirically calculated density. There could be higher error associated with empirically determined density, which would cause an increased RMSE in refractive index for the Eisenlohr and Vogel  $R_d$  methods associated with Pfizer APIs. Therefore,

the accuracy of the crystal density values used in these empirical methods could be evaluated to improve model performance.

Predictive methods can quickly provide refractive index estimates for compounds of interest. However, these empirical methods require homogenous samples. Many pharmaceutical solid samples, especially solid mixtures, are not entirely homogenous, limiting the use of these empirical methods. Accurate crystal density values are also required which may not always be obtainable. However, the dependence of refractive index on density according to Lorenz-Lorentz equation creates a fundamental base for using refractive index measurements for characterization of density related material attributes (see sec 1.3.3).

#### **1.3.2.6. Summary of Refractive Index Methods**

Different methods exist for measuring refractive index of solids. Table 1.1 lists few of the available options. In this Table, reflectance methods refer to ellipsometric methods, while transmittance methods refer to interferometric and terahertz methods. Selecting the right refractive index method depends on the type/form of solid material being measured, and consideration of each methods advantages and disadvantages.

Refractive index characterization of crystalline solids is of interest to multiple industries including pharmaceutical industry (see sec 1.3.3.). For quick estimation of the refractive index of these solids, predictive methods can be employed. However, these methods are empirical and require accurate knowledge of the material properties. Alternatively, the refractive index can be measured with all the previously defined refractive index measurement methods. Prism based

methods provides the most accurate measurements (lowest relative error) for crystalline solids. However, strict sample restrictions are required for performing these measurements.

Transmittance methods addresses this concern as both crystalline and amorphous components of tablets can be characterized with terahertz spectroscopy. The transmittance methods, however, have a higher relative error than prism based methods.

Methods	Applications	Relative Error	Advantages	Disadvantages
Prism	Crystalline solids <sup>18, 43, 50</sup>	$10^{-6}$ ( <sup>6</sup> )	Low uncertainty	Sample size and shape limitations
Reflectance	Thin films <sup>62, 65-69, 107</sup>	$10^{-3}$ ( <sup>61</sup> )	Little to no sample information required	Requires smooth sample surface and assumes no light absorption
Transmittance	Thin films <sup>55, 85, 86, 108</sup> , crystalline/amorphous solids <sup>19, 22, 80, 81, 109</sup> , tablets <sup>20, 21, 23, 24, 88, 89, 110, 111</sup>	$10^{-5}$ ( <sup>60</sup> )	Can measure pharmaceutical compacts	Sample thickness required. Sensitive to moisture in environment
Predictive	Crystalline solids <sup>99, 100</sup>	$10^{-2}$ ( <sup>99</sup> )	Provides quick refractive index estimates	Based on empirical relationships that requires accurate crystal density information

*Table 1.1: Comparison of different refractive index measurement methods*

Another type of solid material that is important to characterize are films. The interferometric, ellipsometric, and terahertz methods can be used to measure refractive index of thin films. Interferometric methods are applied mostly to transparent samples as the light is required to pass through the sample in order to detect phase delay. Terahertz spectroscopy uses light pulse with approximate frequency range of 300 GHz – 3 THz, which allows light penetration through opaque and relatively thick samples. However, the disadvantage of these transmittance techniques is that the sample thickness needs to be known and the measurement are susceptible to moisture in the environment. In contrast, reflectance methods such as ellipsometry requires no

sample information and can measure much thinner films. However, the ellipsometric methods require sample to have smooth surface and little to no light absorption.

Multiple refractive index methods are discussed in this paper. The type of solid is an important aspect in the selection of the refractive index method. The complexity of most solids has primarily limited the refractive index method to terahertz spectroscopy. Even though this method is still not widely accessible, the ability of this technique to measure wide range of solids has increased the application of refractive index. Specific pharmaceutical applications are discussed in the subsequent section.

### **1.3.3. Pharmaceutical Applications of Refractive Index**

Refractive index characterization of pharmaceutical solids has been used in multiple applications to improve understanding of pharmaceutical drug products. The types of solids measured in these applications include thin films, crystalline/amorphous solids, and pharmaceutical compacts. The refractive index measurement method typically employed for each sample type is listed in Table 1, along with a summary of their major advantages and disadvantages. Information contained in refractive index measurements has generated pharmaceutical applications including characterization of the solid state<sup>107-109, 112</sup>, the crystalline form<sup>18-20, 22, 80, 81, 111</sup>, and the density<sup>20, 21, 23, 88</sup> of the material.

The solid form of most drugs and excipients is crystalline throughout the drug development process, however, development of active ingredients in the amorphous state is becoming more common. Amorphous solids are materials containing short-range molecular order without a

defined lattice structure. These solids are thermodynamically less stable than their crystalline counterparts. The lower stability of the amorphous state is certainly a disadvantage; however, co-amorphous formulations provide an opportunity to enhance dissolution and bioavailability for poorly water soluble drugs.<sup>113</sup>

Refractive index measurements can potentially be used to characterize the amorphous solid. Considering a specific volume versus temperature plot for an amorphous solid transition, decreasing the temperature below the glass transition temperature significantly reduces the molecular mobility. This phenomenon results in a transition of the material from a super cooled liquid to an amorphous solid. Therefore, knowledge of the glass transition temperature reflects changes to critical material parameters such as molecular mobility and flexibility of the amorphous solids. According to the study by Beaucage *et al.*<sup>107</sup>, refractive index measurements can facilitate in determining the glass transition temperature for assessment of the amorphous state.

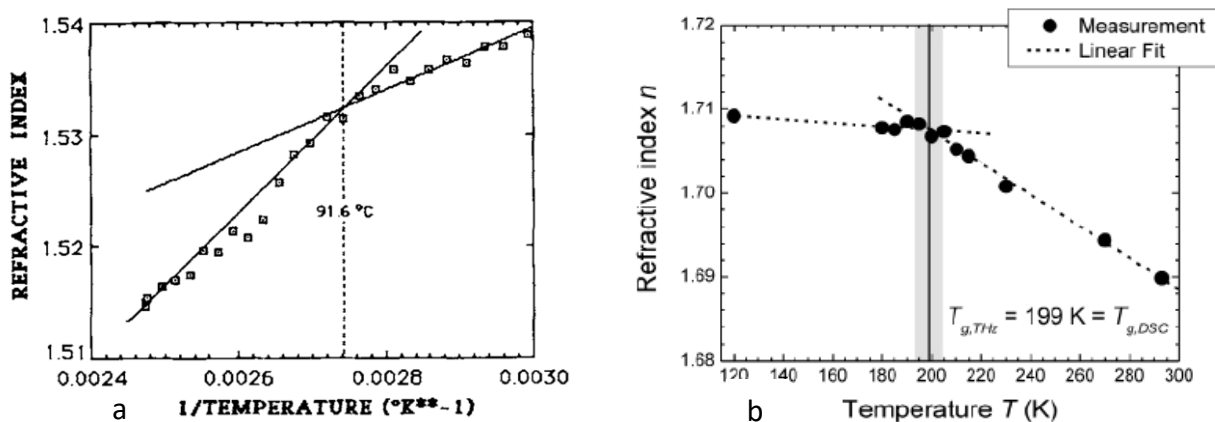


Figure 1.13: Refractive index versus inverse temperature of polystyrene film developed using ellipsometric method<sup>107</sup> and of poly(oxymethylene) using terahertz spectroscopy<sup>108</sup>

The glass transition temperature is obtainable by analysis of temperature dependent refractive index data. In the study by Beaucage *et al.*<sup>107</sup>, the glass transition temperature of polystyrene films was determined. The ellipsometric method was used to measure the refractive index of the thin films. Figure 1.13a shows the plot of refractive index versus inverse of temperature in which two distinct regions were identified based on slope difference. Slope change is potentially associated with the volume expansion and density change associated with the change in amorphous state. The temperature corresponding to the specific refractive index at which the slope change occurs is considered the glass transition temperature. According to Figure 1.13a, the glass transition temperature associated with the polystyrene film is 91.6 °C, which falls in the glass transition temperature range (85 to 110 °C) of polystyrene from other reported studies<sup>114</sup>. A concern with using ellipsometric methods is that only information from the surface of the of film is provided. Therefore, the bulk glass transition temperature is not measured. In addition, the authors<sup>107</sup> stated that these results matched closely with measurement from differential scanning calorimetry (DSC), however, the DSC results were not provided, thus the entire glass transition temperature range was not verified for this specific case.

A similar study by Wietzke *et al.*<sup>108</sup> addresses these concerns. In this study the glass transition temperature of the polymer, poly(oxymethylene), was measured with terahertz spectroscopy and verified with DSC. In contrast with the study by Beaucage *et al.*<sup>107</sup>, the entire glass transition range is provided from DSC. This range, highlighted in Figure 1.13b, included the temperature associated with the inflection point of their refractive index versus temperature plot (Figure 1.13b). In addition, terahertz spectroscopy offers the additional advantage of providing bulk information of the material assuming the sample thickness is provided.

The application of refractive index for determining the glass transition temperature can be further strengthened by considering additional factors. The measurement of glass transition temperature, a kinetic parameter, is dependent on the experimental conditions. For example, the temperature ramp rate and quench time during DSC measurements results in differing glass transition temperature ranges. Therefore, it would be important to consider the effect of experimental conditions on refractive index based glass transition measurements. Also, most of the reported studies with using refractive index to estimate glass transition temperature, report a single value. The glass transition temperature corresponds to the temperature range in which the supercooled liquid transitions into amorphous solid. Therefore, the full glass transition may not be captured by refractive index based glass transition measurements. Thus, the advantages and disadvantages of extracting a single value for glass transition temperature can be further considered. Refractive index measurements has been shown to be promising complimentary tool in determining the glass transition temperature of polymers and potentially other pharmaceutical amorphous solids.

Applications of refractive index measurements for crystals may attract higher interest due to most drugs existing in crystalline form. Different drugs can vary in their crystalline structure. In addition, one drug can exist in multiple polymorphic forms, where each form often drastically varies the physicochemical properties (*i.e.* solubility, stability, and bioavailability) of the drug.<sup>115</sup> Therefore, it is important to characterize the crystalline structure of the drug and excipients to improve the manufacturability and the final product performance of the solid dosage form.

Refractive index measurements were used to assess the crystalline form of the drug. A study by Watanabe *et al.*<sup>18</sup> indicated that refractive index measurements was able to differentiate crystal systems. Even within a crystal system, refractive index measurements were able to differentiate the crystal habit. The traditional prism method was used to measure crystals with low uncertainty, however, owing to the size and shape limitations, the authors measured several different drugs with different crystal systems by immersing samples in oils with specified refractive index and using a microscope. Specifically, key refractive index, defined as unique and reproducible refractive index measurements, were obtained for each crystal. Results showed that different drugs had unique key refractive indices and the number of key refractive index obtained for each crystal had potential high correlation to the crystal system.

The results provided by Watanabe *et al.*<sup>18</sup> suggest a link between refractive index and crystal structures, however, statistical evaluation of both single and multiple component samples can strengthen this relation. Measurement error and standard deviation for refractive index was not reported by Watanabe *et al.*<sup>18</sup>, which are required to determine statistical significance between measurements. Therefore, validation of refractive index relation to different drugs and their crystal structure can be further achieved through more comprehensive statistical analysis.

The relationship between refractive index and crystalline structure can be further enhanced by considering additional sample sets. Only pure samples with specific crystal form were measured by Watanabe *et al.*<sup>18</sup>, however, measurements of multi component samples, including drug and excipients, that resemble the final drug product can also increase the application of refractive index measurements. In addition, pharmaceutical products may include multiple polymorphs of

the drug especially if the drug has undergone partial physical degradation. Establishing quantitative models relating refractive index to drug amount and the respective fraction of each polymorph present provides an opportunity to assess assay and physical stability.

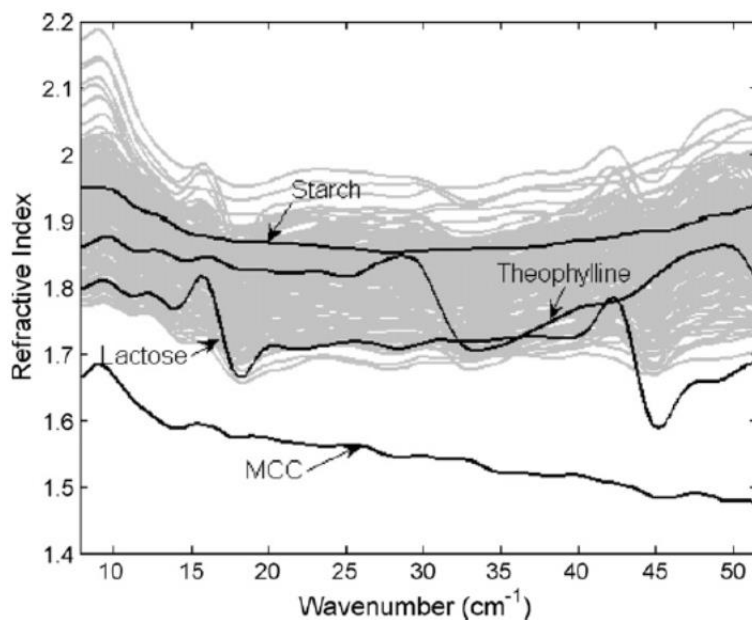


Figure 1.14: Refractive index spectra of 4-component tablets (grey) along with pure component tablets (black) measured with terahertz spectroscopy<sup>20</sup>

A study by Palermo *et al.*<sup>20</sup> investigated drug assay with refractive index measurements for multi component tablet system. The refractive index was measured rapidly and non-destructively with terahertz spectroscopy. Other studies are also available in literature<sup>22, 111</sup> demonstrating refractive index measurements from terahertz spectroscopy as a means for drug assay, however, the study by Palermo *et al.*<sup>20</sup> challenged previous methods by assessing complex pharmaceutical samples. The measurements were made on a set of tablets containing combination of amorphous (microcrystalline cellulose and starch) and crystalline (theophylline and lactose monohydrate) components. These tablets had varying density and concentration of each ingredient according to

a quaternary mixture design. Figure 1.14 shows the refractive index spectrum of each pure component along with all the four component tablet spectra. The crystalline components have finger print regions at wave numbers corresponding to strong absorption due to dispersion effects. In contrast, refractive index spectra of pure amorphous components are generally featureless potentially due to reduced phonon vibrations from lack of long-range order. A partial least square (PLS) model was generated from the refractive index spectrum of each tablet for predicting theophylline weight fraction (w/w). The prediction error of the best model was approximately 0.054 w/w. This study showed that accurate quantitative models for crystalline drug content was developed with refractive index measurements for complex tablet systems.

Characterization of the physical stability of drugs requires quantitative methods to characterize the various potential crystalline forms. The study by Watanabe *et al.*<sup>18</sup> measured the refractive index of different polymorphs of multiple drugs including bromovalerylurea for identification purposes. However, studies performed with terahertz spectroscopy include identification and quantification of polymorphs. An example is a study by Zeitler *et al.*,<sup>109</sup> in which the transition of carbamazepine from the amorphous state to the crystalline state was monitored with terahertz spectroscopy. The solid form transitions were induced by carefully controlled temperature changes. Figure 1.15 shows three different measurements (peak electric field, peak position, and terahertz pulse time delay) from terahertz spectrometer plotted against temperature. In addition, the graph identifies the state of the solid (glassy, rubbery, crystal form III, crystal form I) along with the transitional phases (glass transition, crystallization, and crystal phase transition). The peak electric field corresponds to the terahertz absorption and as expected the absorption is higher for the crystalline state than the amorphous state due to phonon vibrations. The time delay

and the peak position correspond to changes in the phase of the pulse that directly impacts the refractive index. In general, the peak position increases as the carbamazepine transitions from amorphous to crystalline. An increase in peak position results in a higher phase change causing the refractive index to increase. Therefore, each solid state has a specific refractive spectrum.

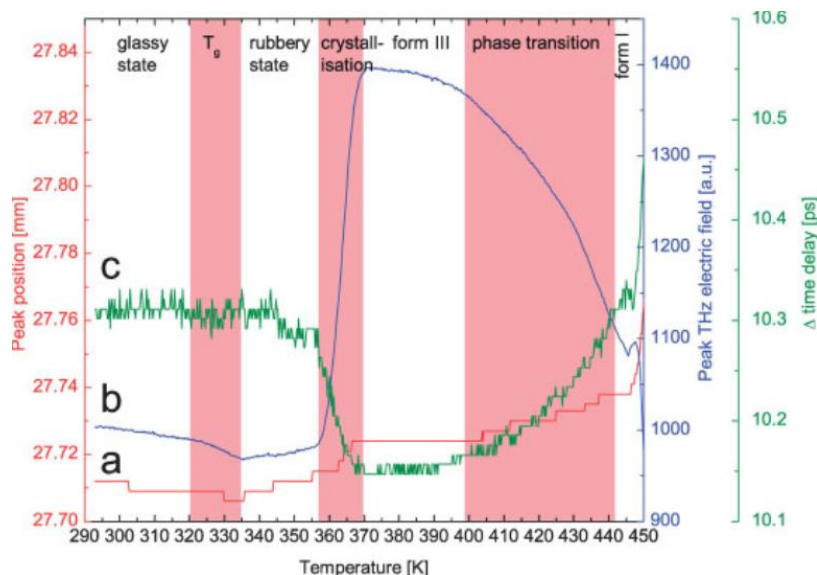
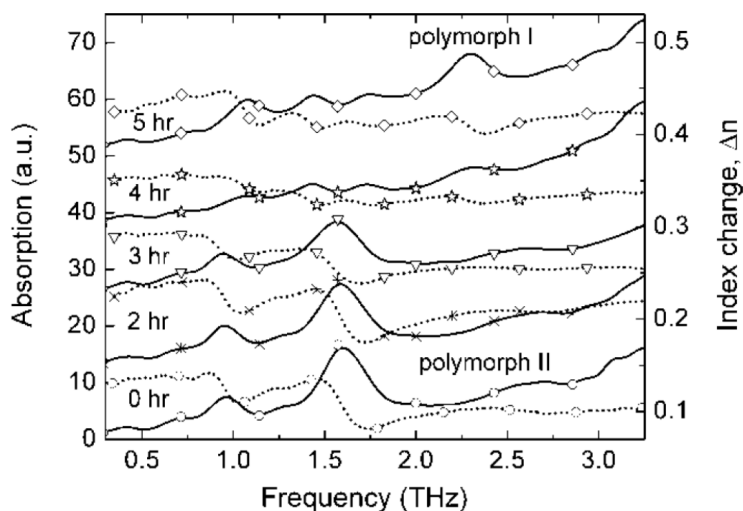


Figure 1.15: Terahertz measurements of peak position, peak THz electric field, and time delay (appropriately color coded) versus temperature for carbamazepine with the specific solid states appropriately labeled<sup>109</sup>

The concept of relating terahertz spectral information with the solid state is further visualized through another study by Upadhy et. al.<sup>80</sup> Theophylline samples were stored at high temperature for different amounts of time to achieve different degrees of polymorphism in this study. Figure 1.16 shows terahertz absorption and refractive index spectrum of theophylline polymorph I and II along with spectra of their mixtures. At locations of high absorbance, there is a sharp decrease in refractive index due to dispersion. The absorbance and refractive index spectrum for both polymorphs are unique, thus, the spectral data are able to be used for quantification of chemical concentration similar to Palermo *et al.*<sup>20</sup>. Most polymorph identification and quantification studies found in literature<sup>20, 81, 82, 111, 116-118</sup> using terahertz spectroscopy utilize the absorbance

spectrum, however, due to the previously mentioned connection between absorbance and refractive index, it can be inferred that refractive index spectrum may be similarly useful in future research. This terahertz spectroscopy application can potentially be extended to other more common and widely accessible refractive index measurement methods, thus, allowing identification and quantification of polymorphs to be done in a feasible and efficient manner.



*Figure 1.16: Terahertz absorption and refractive index spectra of theophylline's polymorph I (top) and II (bottom) along with their combination. The polymorph forms were controlled by adjusting materials storage time in 523 K environment<sup>80</sup>*

In addition to crystal form, refractive index is also dependent on the density and porosity of the sample. Pharmaceutical compact density is a critical quality attribute for most solid oral dosage products owing to its relationship to friability, disintegration, and dissolution. Both refractive index and effective refractive index measured with terahertz spectroscopy have been shown to be highly correlated to the relative density of compacts.<sup>2, 20, 21, 88</sup> Figure 1.17 shows the results from a study by Ervasti *et al.*<sup>88</sup> in which a linear relationship between refractive index and porosity was demonstrated. For their study, pure microcrystalline cellulose (MCC) tablets were produced with similar thickness and varying porosities. It was determined that the minimum porosity

change detectable with terahertz refractive index measurements was approximately 0.49 % over an approximate porosity range of 22 to 40 %. A study by Bawuah *et al.*<sup>21</sup> further verified this linear relationship for MCC tablets and reported a porosity error estimate of approximately 1 %. To challenge the refractive index and density relationship further, the study by Palermo *et al.*<sup>20</sup> used multicomponent tablets, which were compacted at different compression forces. A PLS model was generated between refractive index spectra and measured tablet density. The prediction error for the model was approximately 0.011 g/cm<sup>3</sup>. These studies demonstrate that terahertz spectroscopy provides a rapid non-destructive alternative to techniques such as mercury porosimetry.

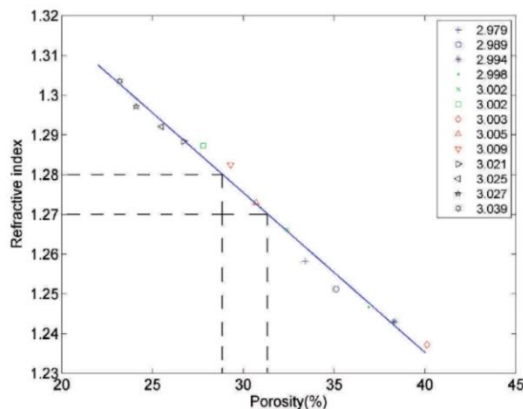


Figure 1.17: Refractive index versus porosity trend. The numbers in the figure represent each tablet's thickness value in millimeters<sup>88</sup>

However, the relationship between refractive index and porosity is material specific. A refractive index-based porosity model built on a tablet system typically does not apply to another tablet system consisting of an altered formulation. This is because the refractive index is dependent on the porosity and the crystalline structure. Therefore, each tablet system requires appropriate calibration samples to calculate a model for refractive index and tablet porosity based on terahertz measurements.

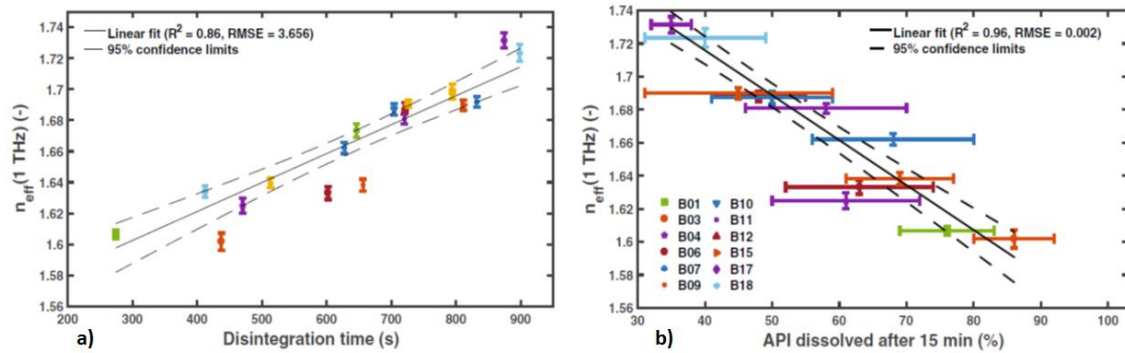


Figure 1.18: Effective refractive index versus disintegration time (a) and amount of drug dissolved (b) trends<sup>2</sup>

Tablet porosity influences tablet disintegration and dissolution, depending on the drug release mechanism. Refractive index measurements are used to assess these density dependent critical attributes. A recent study by Markl *et al.*<sup>2</sup> analyzed tablets containing a poorly water soluble drug product manufactured using high shear wet granulation, fluid bed drying, and compaction. Tablets were produced according to a design, which varied wet granulation and compaction process parameters. The correlation coefficient and root mean square error were determined to be 0.86 and 3.656 seconds for disintegration time and 0.96 and 0.002 % for amount of drug dissolved (Figure 1.18). The results suggest a strong correlation between refractive index and both disintegration time and dissolution amount. However according to Figure 1.18b, the drug dissolution has large standard deviations for each set of measured tablets. This could be the result of tablet inhomogeneity for each same set due to inadequate powder mixing. Generally, tablet dissolution is not only dependent on compact density but also additional factors such as the chemical formulation, tablet homogeneity, and particle density. Figure 1.18a results also show no standard deviation for disintegration time. This was because disintegration time variation was not assessed as the authors considered the traditional disintegration test method to be inaccurate and suggested the use of alternative disintegration methods to further strengthen the model between

refractive index and the propensity for the tablet to disintegrate upon contact with aqueous solutions. This study among others<sup>24, 25, 89, 110</sup> demonstrate the utility of terahertz spectroscopy for rapid at-line determinations of density related critical quality attributes of tablets.

Potential future applications associated with refractive index and terahertz spectroscopy include not only assessment of advanced solid oral dosage forms (*i.e.*, bilayer tablets<sup>25</sup>) but also development of on-line measurement strategies<sup>119</sup>. A study by Niwa *et al.*<sup>25</sup>, evaluated the adhesion integrity between two layers for bilayer tablets with terahertz spectroscopy. Reflectance terahertz measurements were used to obtain interface index, which represented the magnitude of change in refractive index at the layer interface but not the actual refractive index. Figure 1.19 displays a 2D interface index color map and their respective histogram of three different tablets with varying adhesion strength. The adhesion strength was primarily varied by setting the final compression pressure to 6, 10, and 14 kN while holding the precompression pressure constant at 0.6kN. Higher final compression pressure was associated with lower adhesion strength, thus, resulting in a higher interface index. The higher interface index was potentially due to presence of larger internal fractures. However, only one chemical system was studied, therefore, the robustness with respect to chemical constituents of each layer was not considered in this study. The chemical constituent of each layer contributes to the overall layer terahertz absorption and refractive index. Certain components, especially crystalline materials, have strong absorption in the terahertz region. These strong absorbers can limit the amount of reflected or transmitted terahertz signal for appropriate spectral analysis. Along with the terahertz absorption, the inter layer refractive index difference is also important since it dictates the magnitude of light reflection and refraction at the interface. These reflection and refraction events are critical in

determining the interface index. Therefore, measurement of refractive index of bilayer tablets can be used to determine the adhesion integrity.

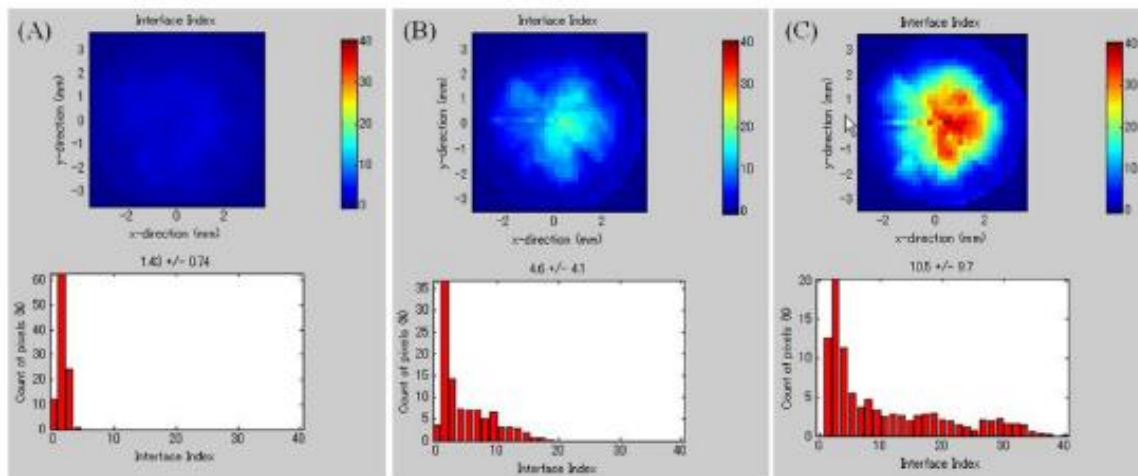


Figure 1.19: Interface index map and their respective histogram plots for tablets produced at 6 (a), 10 (b), and 14 (c) kN final compression force<sup>25</sup>

The location and size of the fractures present in multi layered tablets also affect the terahertz measurements. The study by Niwa *et al.*<sup>25</sup> created a bilayer tablet system in which the major fractures occurred at the interface. However, inter layer fractures also influence the terahertz measurements and overall mechanical strength of bilayer tablets. Performing both reflectance and transmittance terahertz measurements can facilitate in determining the mechanical strength of the tablet. Reflectance measurements can potentially provide depth assessment of the fractures, while transmittance measurements can provide average intra tablet density information. Further supporting work with consideration of material and process parameter variation including work with both reflectance and transmittance terahertz spectroscopy can establish refractive index as a factor indicating the mechanical strength of multi layered tablet systems.

Real time monitoring with terahertz spectroscopy in pharmaceutical compaction based unit operations is also a potential application for refractive index measurements. Terahertz spectroscopy offers rapid, non-destructive, and non-invasive refractive index measurements, which is ideal for real time monitoring. A study by May *et al.*<sup>119</sup>, demonstrated real-time monitoring of tablet coating process with reflectance terahertz spectroscopy for coating thickness measurements. Similarly, transmittance terahertz spectroscopy can be potentially applied for real time density analysis of pharmaceutical compaction processes such as tableting and roller compaction. However, applying terahertz spectroscopy in-line introduces challenges. Terahertz spectroscopic measurements are highly sensitive to moisture; therefore, it can be difficult to completely control the measurement area in a real time setting. In addition to the interference of moisture, dust generated from the respective unit operation can also interfere with the measurement. With consideration of these limitations, real time density assessment of tablets and ribbons from compaction-based unit operation can ensure the drug product is manufactured with the desired product quality, especially meeting disintegration and dissolution specifications.

Current refractive index methods have shown the capability to enhance formulation development and manufacturing quality of solid drug products with off-line measurements. However, terahertz spectroscopy potentially provides the extra advantage of rapid and routine assessment of pharmaceutical solids. Further, this technique has potentially at-line, in-line, and/or on-line measurement capabilities. Thus, possible future applications of refractive index measurements include real time monitoring of physical attributes, such as porosity and mechanical strength, for compaction based unit operations with terahertz spectroscopy.

#### **1.3.4. Summary**

Refractive index is an important optical parameter for many different materials. It is defined in terms of the angle of an incident light upon a new medium and the angle of light refraction inside the new medium. In addition, the refractive index is also defined in terms of the ratio of the speed of light within the two media. The wavelength of the impinging light and material properties both effect the measured refractive index. Empirical models and electronic theory both show that the refractive index is dependent on the wavelength/frequency of light. In addition, the crystal structure, density, permittivity, and permeability of the solid material also impact refractive index. Refractive index relation to these material properties can be used to improve understanding of pharmaceutical solids.

Multiple methods are available to determine refractive index. This review article highlights the following methods: prism methods, interferometric methods, ellipsometric methods, terahertz methods, and predictive methods. If the physical and chemical properties of the solid crystalline material is well characterized, then predictive methods based on empirical relations is able to be used to quickly estimate the refractive index of the material. These empirical relations are based on the Lorenz-Lorentz equation, which relates refractive index to molecular weight, density, and molar refraction. However, not all pharmaceutical solids have physicochemical properties that are accurately characterized, and thus require methods which require refractive index measurements.

Prism methods were among the first measurement methods for refractive index. These traditional methods are based on measuring light transmission through a prism shaped sample. However, it

is often impractical to obtain prism shaped samples. These methods have been modified by immersing solid samples into liquids with known refractive index to reduce sample restrictions. In general, prism methods have the lowest relative error for refractive index measurement. However, shape and size sample restrictions limit the pharmaceutical applications of these methods.

Transmittance and reflectance methods are also available for measuring refractive index.

Transmittance methods include interferometric methods and terahertz methods, while reflectance methods include ellipsometric methods. Ellipsometry involves analysis of the polarization change due to light reflecting from the surface of the sample. Refractive index is determined with the polarization change information applied to Fresnel reflection coefficients. This method is used to measure thin films and requires minimal sample information. However, these methods assume no absorption of light from the samples and requires optically smooth ample surface for accurate measurements. In addition, ellipsometric methods only measure the refractive index of the surface of the sample and not the bulk. In contrast, transmittance methods analyze the light transmitted through the sample, thus, resulting in a bulk measurement. Interferometric methods assess light interference (fringe) patterns from light travelling through the sample and light traveling in absence of sample. These fringe patterns are used to determine refractive index. Interferometric methods rely on analysis of transmitted light, thus, mostly are applicable to transparent cylindrical solids. For opaque samples, terahertz spectroscopy, another transmittance method, can be used. Visually opaque samples are often relatively transparent to the terahertz region of the electromagnetic spectrum. This allows rapid transmittance measurements of such samples. This advantage has allowed terahertz spectroscopy to measure a wide range of solid

samples from thin films to tablets. However, limitations of these transmittance methods include reduction of measurement accuracy in the presence of environmental moisture and requirement of sample thickness measurements.

The available refractive measurement methods, especially terahertz spectroscopy, have opened opportunity for several applications in the pharmaceutical industry. These applications include solid state characterization, crystal form identification and quantification, and mechanical strength assessment of solid oral dosage forms. Specifically, refractive index measurements have been shown to differentiate between the amorphous and crystalline states. The glass transition temperature is an important parameter for characterizing the amorphous state; and has been determined by analyzing refractive index versus temperature trends. For the crystalline state, both the crystal form and the quantity of the crystalline forms present in tablets have been determined with refractive index spectrum. Additionally, the strong correlation between refractive index and porosity, allows determination of pharmaceutical compact density and density related critical quality attributes.

Potential future applications for refractive index include real time assessment of pharmaceutical compact density and mechanical strength assessment of multi layered tablet systems. Real time refractive index measurements are possible with terahertz spectroscopy. In-line reflectance terahertz measurements has previously shown to measure tablet coating thickness. However, no literature examples of utilizing in-line refractive index measurements from transmission terahertz spectroscopy for pharmaceutical compact density assessment in compaction based unit operations have been published. In addition, to real time assessment, there are potential

opportunities for utilizing both reflectance and transmittance terahertz spectroscopy for non-destructive mechanical strength assessment of multi layered tablet systems.

Refractive index measurements can potentially improve formulation development and manufacturing of pharmaceutical solid dosage forms by complimenting additional material characterization measurements and/or providing critical quality attributes of intermediate/final solid products. This literature review highlights current methods for refractive index measurements. Continued improvements in these methods can potentially expand pharmaceutical applications of refractive index measurements.

## **Chapter 2: Evaluating the Robustness of Terahertz Based Porosity Models Against Chemical Composition and Process Parameter Variations for Multicomponent Pharmaceutical Compacts**

### **2.1. Introduction**

Roller compaction and tablet compression are two important unit operations of solid oral dosage manufacturing in which pharmaceutical compacts are produced through compression of solid particulate blends. Roller compaction, a dry granulation process, involves converting primary solid particles into granules to improve material flowability. The procedure for this granulation process involves feeding the primary material between two rollers to produce compacted ribbons, which are later milled to produce granules. Similarly, in a tablet compression process, two punches are used to consolidate the solid material into compacts. The porosity of the pharmaceutical compacts produced in both of these unit operations is often considered as a critical quality attribute (CQA) owing to its significant influence on mechanical strength<sup>120-123</sup>, disintegration time<sup>1,2</sup>, and dissolution time<sup>2-4</sup> of tablets, the most widely used dosage form.

Porosity is defined as the fraction of the void space with respect to the bulk volume.

Conventional measurements methods for porosity include mercury porosimetry, gas adsorption, and calculations using bulk and true density measurements.<sup>124</sup> However, mercury porosimetry and gas adsorption are often undesirable. These techniques are time consuming and require sample intrusion with either a gas or liquid mercury, thus causing concerns of sample contamination.

Calculating porosity with bulk density and true density is a more common approach. Bulk density is obtained by using the dimensions and weight of the tablet, while true density is assessed with a helium pycnometer. The ratio of bulk density to true density of the tablet is the solid fraction, where the complement of this fraction is porosity. This method is non-destructive and non-intrusive with regard to the tablet sample. However, performing rapid intra tablet and intra ribbon porosity measurements during the tablet manufacturing and roller compaction processes remains a challenge due to required information of mass and dimensions of the sample. According to the US Food and Drug Administration's promoted quality by design methodology described in the guidance for process analytical technology (PAT)<sup>125</sup>, it is important to monitor and control CQAs such as porosity during the process in a timely manner, as opposed to at the end of process (end product testing). Thus, PAT methods are highly desirable for porosity assessment.

Multiple types of PAT methods exist for assessing the porosity and density of pharmaceutical compacts. One common type of PAT method used for this purpose is near infrared spectroscopy (NIRS) utilized in reflectance mode. Both tablet<sup>126-130</sup> and ribbon<sup>131-137</sup> porosity have been characterized with NIRS due to the sensitivity of this technique to scattering. An increase in porosity causes more light scattering due to an increase in the area of interfaces between solid and air within the compact. This phenomenon results in an increase in the slope and baseline in the NIR spectrum. Alongside NIRS, Raman spectroscopy<sup>130, 138-140</sup> has also been used for compact porosity assessment. According to the study by Shah et al.<sup>130</sup>, porosity was highly correlated with the intensity change at most all wave numbers of the Raman spectra. However, this relationship is still not clear as a contradictory study by Peeters et al.<sup>138</sup> has shown no effect

of porosity on Raman spectra. These two vibrational techniques are popular PAT methods; however, they are generally unable to capture bulk information of the sample. This is a consequence of these techniques primarily operating in a reflectance geometry combined with a limited depth of penetration. Other transmission based PAT methods for compact porosity include ultrasound<sup>141</sup> and gamma ray<sup>142</sup> transmission, however, these techniques require intimate sample contact or carcinogenesis. Terahertz time of flight spectroscopy (THz-TOF) is a potentially alternative PAT method that allows for safe, non-destructive, non-contact, and rapid measurements in transmission mode.

Terahertz time of flight spectroscopy operates in the far-infrared region (approximately 300 GHz–3 THz or 10-100  $\text{cm}^{-1}$ ). This specific range of low frequency induces crystalline phonon vibrations, intermolecular bond vibrations (hydrogen bonding), and torsion vibrations in pharmaceutical samples. The operation of the THz-TOF instrument in the transmission mode involves converting a NIR coherent ultrashort (femtosecond time scale) laser pulse into a terahertz pulse with a photoconductor. This terahertz pulse is then directed towards the solid sample. A time gated detector on the opposite side of the sample records the time domain signal of the transmitted terahertz pulse. Calibrating the time domain signal of the sample against the time domain signal with no sample (reference time domain signal) allows extraction of important physicochemical properties such as absorption coefficient and refractive index.

Refractive index is of particular interest for pharmaceutical compacts as its strong correlation to porosity has been frequently reported in the past decade. A study by Ervasti *et al.*<sup>88</sup>, observed a linear trend between refractive index and porosity with a high sensitivity. According to their

results, a refractive index change of 0.0041 corresponded to a porosity change of 0.01 for microcrystalline cellulose tablets. Additional studies have further developed univariate<sup>21, 23, 124, 143-149</sup> and multivariate<sup>20</sup> linear models for predicting porosity with refractive index based information from THz-TOF. Univariate methods include models based on zero porosity approximation<sup>146, 149</sup> and effective medium approximation<sup>21, 149, 150</sup> *i.e.*, Bruggeman model<sup>151</sup>, which define porosity in terms of effective refractive index of the solid matrix and the intrinsic refractive index of the solid. The most widely used univariate models for porosity were all recently compared and were shown to have similarly high correlation coefficients of approximately 0.99 and low root mean square errors of approximately 0.002 for a multicomponent tablet system.<sup>149</sup> The high accuracy of these univariate models suggests THz-TOF as a promising PAT tool, however, further work demonstrating model robustness is required for regulated pharmaceutical applications. In addition to these univariate models, a multivariate partial least squares (PLS) model using frequency domain refractive index spectra collected with THz-TOF in reflectance mode was also developed by Palermo et. al.<sup>20</sup> This model had a high correlation coefficient of 0.937 and a low prediction error of approximately 0.011. However, the accuracy of this reported PLS model may potentially be improved by using refractive index spectra from transmission measurements which is evaluated for the first time herein.

The present study further advances the understanding of the accuracy and robustness of both univariate and multivariate terahertz based porosity models for the applications of process monitoring and control of a roller compaction or a tablet compression unit operation. It is desirable for these porosity models to be accurate and robust against common variations in the

process such as process parameters and chemical composition variations. These variations are important to consider especially for a system with an implemented control strategy. For example, a study by Singh et al.<sup>152</sup> implemented a combined feed-forward and feed back control system for tablet manufacturing process. In their system, a feed-forward loop was used to account for raw material variation such as bulk density by adjusting the fill depth. In addition, multiple feed-back loops were used for controlling compression force, tablet weight, and tablet hardness. During the process multiple process parameters are constantly adjusted to account for any process deviations. Thus, for use in a control strategy, it is important for the porosity method to be robust against these process variations and material variability.

Previous studies<sup>21, 23, 88, 143, 144</sup> have included process parameter variations such as compression force and fill weight into consideration during model development; however there are limited studies<sup>20, 146, 148</sup> addressing the chemical composition variation. Chemical composition variation causes the intrinsic refractive index of the solid to change, thus, potentially reducing the model predictive capability for different formulations. Two recent studies<sup>146, 148</sup> investigated the effect of the change in the active pharmaceutical ingredient (API) weight fraction and porosity on effective refractive index for a binary tablet system comprising of indomethacin and microcrystalline cellulose. These studies concluded that porosity had a more dominant impact on effective refractive index than the API weight fraction for approximate porosity range of 28 to 50 % and API range from 0 to 15 wt%. The present study expands on these two previous studies by evaluating chemical composition change in a more pharmaceutically relevant tablet system comprising of five components.

The objective of this study was to compare terahertz based porosity models by evaluating their robustness with specific test sets. These test sets are comprised of new process parameter and chemical composition variations which were within the model space. To achieve this objective, pharmaceutical compacts were manufactured with variations in compression force, compression speed, fill weight, and chemical composition. The tablets were split into a calibration set and test sets. The calibration set was used to develop both univariate and multivariate models and included only a few tablets which covered the required porosity range. This study investigated if these few calibration tablets were sufficient to produce a porosity model that is both accurate and robust. Thus, this study provides further steps toward method validation by evaluating the prediction error of both the univariate and multivariate models for porosity from using appropriate test sets. These test sets demonstrated that terahertz based porosity models perform as intended with expected process variations, thus, further establishing the strong potential of THz-TOF as a reliable PAT tool for roller compaction and tablet compression processes.

## **2.2. Materials and Methods**

### **2.2.1. Materials**

In this study terahertz based porosity models were generated for a five-component tablet system. Acetaminophen (APAP, Mallinckrodt Inc., Raleigh, NC, USA), the model drug for these tablets, was blended with appropriate excipients and compressed into tablets. The excipients included lactose monohydrate (Foremost Farms, Rothschild, WI, USA), microcrystalline cellulose (MCC, Avicel PH-102, FMC BioPolymer, Mechanicsburgh, PA, USA), starch (EMD Chemicals, Inc., Gibbstown, NJ), and magnesium stearate (MgSt, ThermoFisher Scientific, Waltham, MA, USA). Lactose monohydrate, MCC, and starch acted as diluents, with starch additionally functioning as a disintegrant. Magnesium stearate was used as a lubricant to facilitate in tablet ejection during

the tablet compression process. The materials were used directly from their originally packaged containers with no additional characterization or processing.

### **2.2.2. Tablet Manufacturing Process**

Tablets were manufacturing using a direct compression procedure in which the five components were blended and then compressed into tablets. All powder blends were produced by placing appropriately weighed components into small plastic containers with an approximate fill volume of 40 percent. The powders were then blended by securing these containers inside a 5.5 L Bohle bin blender (L.B. Bohle, Ennigerloh, Germany) and then rotating for 30 minutes at a speed of 15 rpm. The total batch size of each blend was approximately 10 g. The completed blends were analyzed with ultraviolet-visible spectroscopy (UV-Vis, Hewlett Packard 8453 UV-Visible Spectrophotometer, Agilent Technologies, Santa Clara, CA, USA) to confirm adequate content uniformity (see sec 2.2.3.). Samples from these blends were then compressed into tablets.

Tablet compression was performed using a laboratory press (Instron universal testing system model 5869; Instron Corporation, Norwood, MA, USA) tooled with 13mm flat faced punch and die set. This particular tablet press allows for precise control of process parameters such as compression speed and compression force. Thus, these process parameters and tablet weight were appropriately adjusted for each produced tablet according to the specified experimental design (see sec 2.2.4.). No further experimental controls were applied. All the tablets were stored in a sealed container for one week to allow for viscoelastic recovery before performing any necessary measurements.

### 2.2.3. Blend Assay

Blend content uniformity was assessed with a UV-Vis method for APAP. This UV-VIS method involved generating a linear model between absorbance at a wavelength specific to APAP (243 nm) and concentration of APAP solutions. Seven calibration solutions were produced with APAP concentrations of 4, 6, 7, 8, 9, 10, and 12  $\mu\text{g/mL}$ . Preparation of these solutions involved dissolving 200 mg of APAP with 15 mL of methanol in a 100 mL volumetric flask and then diluting with 18 M $\Omega$  deionized water. This solution was diluted with deionized water by a factor of 10 by transferring a 10 mL aliquot to a 100 mL volumetric flask and q.s.'ing with water. Aliquots of this stock solution were further diluted in 100 mL volumetric flask to produce concentrations within the approximate absorbance range of 0.2 to 0.7 at 243 nm wavelength. At each concentration, three replicate UV-VIS measurements were taken for repeatability analysis. Reproducibility was assessed by obtaining UV-VIS measurement of high, medium, and low concentrations produced on three separate days. The relative standard deviations for the repeatability study were 0.01, 0.01, and 0.07% and for the reproducibility study were 0.21, 0.63, and 0.45% at high, medium, and low concentrations, respectively. The calibration model resulted in a correlation coefficient of 0.9993 and an intercept statistically including zero within the 95% confidence interval.

The developed UV-VIS calibration model was used to predict APAP concentration of solution made from 500 mg samples. Three samples were obtained from each of the blends. Sampling protocol involved removing a sample from the surface of the container. The container was rotated between each sampling to increase the probability of selecting representative samples from different locations. The procedure to analyze these samples involved dissolving the APAP

in the sample with 15 mL of methanol and diluting with deionized water in a 100 mL volumetric flask. This flask was sonicated (Branson 8210 Ultrasonic Cleaner, Branson Ultrasonics Corp., Danbury, CT, USA) for five minutes to further facilitate in the dissolving process. This solution was diluted 10 times with deionized water and then an aliquot of 5 mL was further diluted 20 times to create the final solution. The calibration model was used to predict the APAP from the UV-Vis absorbance value at 243 nm wavelength of the final solution. All the blends were concluded to have an appropriate level of content uniformity according the FDA guidelines<sup>153</sup> as the relative standard deviation of the content in each blend was less than 5%.

#### **2.2.4. Experimental Design**

Tablets were created according to two experimental designs, which varied factors to simulate common variations during a roller compaction and tablet compression process. The first experimental design was a full-factorial design with 4 levels of chemical composition, 2 levels of compression speed (2.4 and 240 mm/min), and 5 levels of compression force (4.5, 7, 10, 13, and 18 kN) as shown in Figure 2.20. The four levels of chemical composition were achieved by producing four blends that independently varied APAP, MCC, and lactose monohydrate according to a mixture design (Figure 2.20). In this mixture design, the levels of these three components were varied by 10 % (w/w). Small chemical variations may occur due to poor local powder mixing and/or segregation during roller compaction and tablet compression processes; thus, this variation is important to consider during method development. In addition to chemical composition, process parameters were also varied to create a range of porosities for the tablets. One tablet was made for each design point, including additional two replicate tablets at the center

point of the design to further assist in statistical analysis. All the tablets for the first experimental design was produced with a tablet weight of 500 mg.

Additional tablets with a second experimental design were also manufactured. This design also used a full factorial design with 2 levels of tablet weight (450 and 550 mg) and 4 levels of chemical composition (Figure 2.20). The same chemical composition levels were used as in the first experimental design, however, this design added tablet weight variation. The was done to account for collinearity between tablet weight and thickness. One tablet was manufactured at each of these design points.

Design Point	APAP (wt fraction)	MCC (wt fraction)	Lactose (wt fraction)	Starch (wt fraction)	MgSt (wt fraction)
1	0.373	0.355	0.207	0.06	0.005
2	0.273	0.255	0.307	0.16	0.005
3	0.273	0.455	0.207	0.06	0.005
4	0.273	0.355	0.207	0.16	0.005

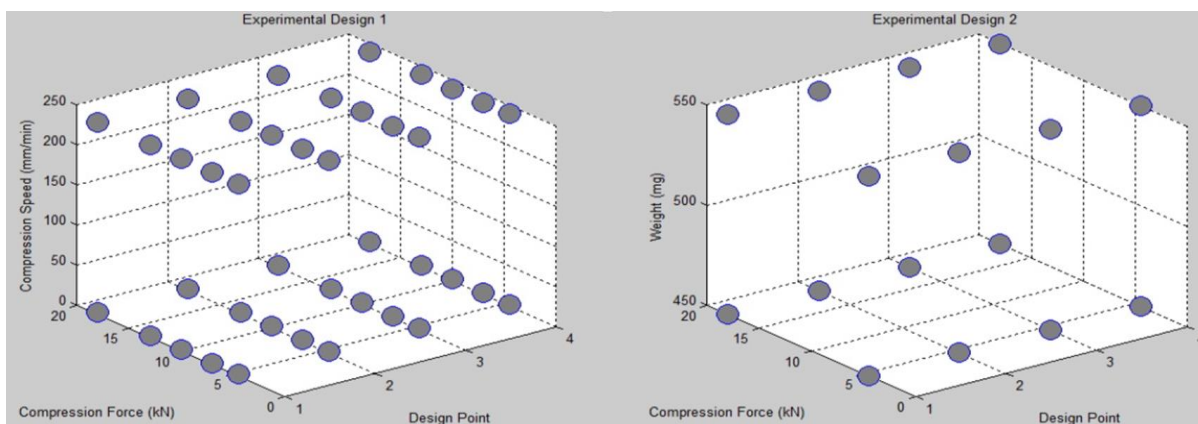


Figure 2.20: Experimental Design (the highlighted Design Point 4 was the center of the chemical mixture design)

The manufactured tablets were split into a calibration set and two test sets. Terahertz based porosity models were developed with the calibration set which included all tablets with the center point chemical composition design (DP4) and fast speed (240 mm/min). The quantitative model built with this calibration set was evaluated for robustness using the two test sets. The first

test set included new process parameter information that were not included in the calibration set. In particular, all the tablets with DP4 chemical composition design and slow speed (2.4 mm/min) was used; therefore, the first test set assessed the model robustness to compression speed. The second test set included new chemical composition and process parameter variance by including all tablets produced with chemical composition design of DP1, DP2, and DP3. The root mean square error of prediction was extracted from the application of the calibration model to the test sets to assess the model robustness to chemical composition and process parameter variance.

### 2.2.5. Tablet Porosity

Tablet porosity ( $\varphi$ ) was calculated by using the diameter ( $d$ ), thickness ( $l$ ), weight ( $m$ ), and true density ( $\rho_{true}$ ) of the tablet according to Equation 50. The dimensions of the tablet were measured with a digital caliper (model CO 030150; Marathon, Richmond Hill Ontario, Canada). The true density of the tablet was determined using the sum of the pure component true densities weighted to its respective weight fraction. The true density of the pure components were measured in powder form with a helium pycnometer (Quantacrhome Instruments stereopycnometer SPY-6DC, Boynton Beach, Florida). These porosity measurements were used to improve the understanding of the refractive index to mechanical strength relationship.

$$\varphi = 1 - \frac{4m}{\pi d^2 l \rho_{true}} \quad (50)$$

### 2.2.6. Terahertz Time of Flight Spectroscopy

Terahertz time of flight spectroscopy in transmittance mode was used to measure refractive index of tablets. This instrument operates by initially producing 1560 nm laser pulse of 50 fs frequency from Laser 1. The laser pulses are directed to a photoconductor, which generates an

incident 500 fs pulse. This pulse is directed at the sample where it can be reflected, transmitted, absorbed, or scattered. Another photoconductor collects the transmitted signal along with 1560 nm pulses from Laser 2. Laser 1 and Laser 2 are synchronized with Laser 2 undergoing variable time delay. Time domain signal is collected when the second photoconductor is simultaneously contacted by the transmitted terahertz pulse and the 1560 nm pulse from Laser 2.

There are two methods to determine refractive index from the obtained time domain signal: the time domain method and the frequency domain method. Both these methods require a time domain signal measured with no sample (reference time domain signal). In the time domain method, the pulse time delay between the sample time domain signal and reference time domain signal is used to determine refractive index. Assuming the tablet sample is homogeneous and the refractive index is similar across all terahertz frequencies, the effective refractive index (time domain refractive index,  $n_{eff,TD}$ ) is defined in terms of the tablet thickness ( $l$ ), speed of light ( $c$ ), and time delay ( $\Delta t$ ) as seen in Equation 51. This method provides one effective refractive index value for a tablet and was used for development of univariate terahertz based porosity models.

$$n_{eff,TD} = \frac{c\Delta t}{l} + 1 \quad (51)$$

Alternatively, the frequency domain method provides an effective refractive index at all terahertz frequencies ( $\omega$ ). This is achieved by converting both the sample and reference time domain signal into frequency domain signal with Fourier transform. The frequency domain signal provides the amplitude and phase information for each of the present terahertz frequencies. The effective refractive index at each of these frequencies (frequency domain refractive indices,  $n_{eff,FD}(\omega)$ ) is then calculated using the phase differences between the sample frequency

domain signal ( $\vartheta_{s0}$ ) and the reference frequency domain signal ( $\vartheta_{r0}$ ) according to Equation 52. The time domain refractive index is computational more efficient than frequency domain refractive index, however, it is susceptible to dispersion and absorption at terahertz frequencies. The frequency domain refractive index is more appropriate for materials that exhibit strong absorption as frequencies that are associated with dispersion can be often avoided. The frequency domain refractive index was used for the development of multivariate terahertz based porosity models.

$$n_{eff,FD}(\omega) = 1 + \frac{c}{l\omega}(\vartheta_{s0} - \vartheta_{r0}) \quad (52)$$

### **2.2.7. Terahertz Based Porosity Modeling Methods**

The extracted refractive index from the THz-TOF measurements were used to generate terahertz based porosity models. Three univariate and one multivariate models were evaluated. The univariate models were based on zero point approximation, Bruggeman approximation, and linear regression. These models involved generating a model with one independent variable; the time domain refractive index value from each tablet. One multivariate partial least squares model was also generated using frequency domain refractive indices associated with relevant terahertz frequencies from each tablet. All these models were developed and evaluated with MATLAB (Version R2016b, Mathworks Inc., MA, USA) and PLS toolbox (Version 821, Eigen-vector Research Inc., WA, USA).

#### **2.2.7.1. Zero Point Approximation**

The first univariate model used for predicting porosity is based on the zero porosity approximation (ZPA) approach.<sup>149</sup> This approach assumes a linear relationship between effective refractive index and porosity within the porosity range of 0 to 1 and effective refractive range of

1 to the intrinsic refractive index of the solid. The intrinsic refractive index of the solid is assumed to correspond to zero porosity. This linear model is illustrated in Equation 53 where the time domain refractive index is a function of porosity ( $f$ ) and intrinsic refractive index of the solid ( $n_{solid}$ ). The equation can be rearranged to solve for porosity (Eq. 54). The tablets from the calibration set were used to determine the intrinsic refractive index. This was achieved by fitting a linear model between the time domain refractive index and porosity and extracting the intercept. The time domain refractive index at zero porosity (*i.e.*, the intercept) was regarded as the intrinsic refractive index. In addition to linearity, this model assumes that the solid is a homogenous matrix composed of two phases (solid and air) and that light scattering due to the sample is negligible.

$$n_{eff,TD} = n_{solid} + (1 - n_{solid})f \quad (53)$$

$$f = \frac{n_{eff,TD} - n_{solid}}{1 - n_{solid}} \quad (54)$$

### 2.2.7.2. Bruggeman Approximation

The second univariate model for porosity used was the Bruggeman approximation. This approximation is based on the effective medium theory which hypothesizes that the average electric flux deviation through the medium is zero. Similar to zero point approximation, this method assumes a two phase system consisting of air and solid with negligible light scattering. Uniquely, this method considers the electric flux deviation through both the solid and pores separately and assumes the pores (inclusions) to be spherical. The porosity in terms of the time domain refractive index and the intrinsic refractive of the solid is defined by Equation 55 according to this theory. The calibration tablets were used to determine the intrinsic refractive index of the solid. Specifically, the intrinsic refractive index for each tablet was numerically

solved with the porosity and time domain refractive index information. The mean of the intrinsic refractive index of all the calibration tablets was, then, calculated and used as the final intrinsic refractive index.

$$f = \frac{1}{1 - \left(\frac{1 - n_{eff,TD}^2}{1 + 2n_{eff,TD}^2}\right)\left(\frac{n_{solid}^2 + 2n_{eff,TD}^2}{n_{solid}^2 - n_{eff,TD}^2}\right)} \quad (55)$$

### 2.2.7.3. Linear Regression

The third univariate model was developed by performing linear regression between porosity and time domain refractive index. The intrinsic refractive index is not required for this modeling approach. The form of this model is seen in Equation 56 where  $\beta_0$  and  $\beta_1$  are the regression coefficients. These regression coefficients were obtained by regressing porosity with time domain refractive index. This model assumes linearity and no correlation between the two variables.

$$f = \beta_0 + \beta_1 n_{eff,TD} \quad (56)$$

### 2.2.7.4. Partial Least Squares

The last quantitative model for porosity was a multivariate model using partial least squares (PLS). This PLS model was developed using frequency domain refractive index spectra. The PLS method reduces the multivariate dimension to extract only the information that corresponds to maximum covariance between frequency domain refractive indices and porosity. The refractive index spectra were truncated to remove areas of low sensitivity before performing this algorithm. In addition, the only other preprocessing performed was mean centering, a requirement for this algorithm to remove the covariance due to the mean spectral shape. This model assumes the

independent and dependent variables are linearly related. There is no need to determine the intrinsic refractive index for this model, however, calibration tablets with relevant variations and reference porosity measurements are required to generate the model.

### 2.3. Results and Discussion

In this study, THz-TOF was used to determine the porosity of pharmaceutical compacts. The compacts were manufactured using a laboratory tablet compression system at various different chemical composition, tablet weight, compression force, and compression speed. Therefore, a tablet set was generated with a wide range of porosity while incorporating potential variations that occur during a roller compaction or tablet compression process.

As illustrated in Figure 2.21, the porosity range was approximately 0.1 to 0.3. Analysis of variance (ANOVA) was also performed to determine the significance of the process parameter and chemical composition factors with respect to porosity. Results from the effects test from ANOVA, which tests the null hypothesis that all parameters are zero, showed only compression force to be significant to porosity at an alpha level of 0.05 (Table 2.2). However, the other factors may influence the THz-TOF measurements. Therefore, this study evaluated the effect of the process parameters and chemical composition on a terahertz based porosity model.

Variables	Sum of Squares	F Ratio	Prob > F
Chemical Design Point	0.00018	0.60	0.4414
Compression Force	0.25508	832.18	<.0001
Compression Speed	0.00046	1.50	0.2265
Tablet Weight	0.00005	0.17	0.6816

*Table 2.2: Results of effects test from analysis of variance*

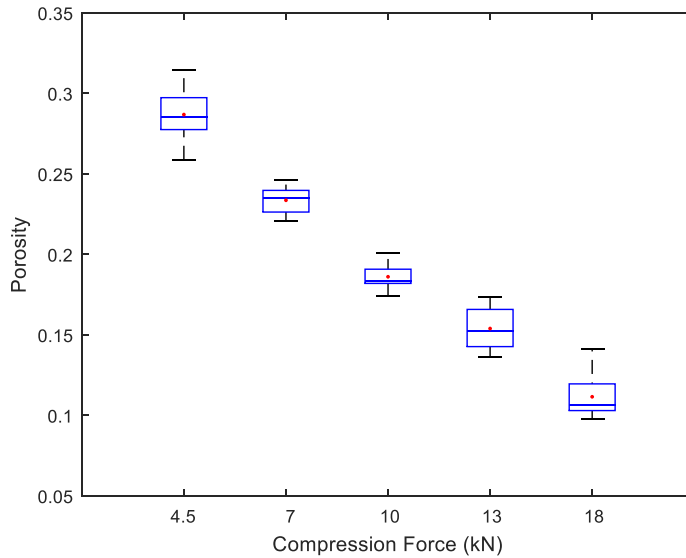


*Figure 2.21: Porosity versus compression force trend*

The manufactured tablets were scanned with THz-TOF to extract refractive index information for the development of terahertz based porosity models. The instrument provides time domain signal as seen in Figure 2.22. According to Equations 51 and 52 both sample and reference time domain signals were required to determine time domain refractive index and frequency domain refractive index.

Both the time domain and frequency domain refractive index were evaluated. The time-domain refractive index calculations were computational less intensive and required the time domain signal of reference and sample to determine the time delay. According to Figure 2.22, there exists a significant time delay between the sample and reference time domain signal due to the absorption, reflection, and/or scattering of the terahertz pulse when incident upon the sample. The time delay was determined by locating the peak maximum of the initial pulse and subtracting the associated time of the pulse. The sample time domain pulse includes additional

received signals after the initial pulse. This is potentially due to multiple reflection or dispersion effects which may reduce the accuracy of the effective refractive index from the time domain method. This issue might be resolved by using frequency domain refractive index.

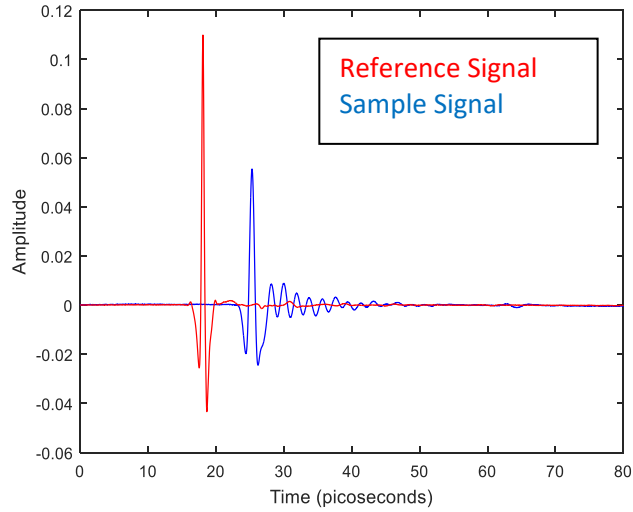


*Figure 2.22: Time domain signal of reference (red) and of sample (blue)*

The frequency domain refractive index was generated by converting the time domain signal into frequency domain using Fourier transform. The refractive index spectrum was then generated by calculating the phase difference between the sample and reference. The refractive index spectra of the calibration tablets are shown in Figure 2.23. Within this truncated frequency range, there was an increase in refractive index with a decrease in porosity. It is important to note that between the frequency range of 0.5 to 0.6 THz there is a sharp decrease in refractive index. This

is potentially attributed to a dispersion effect due to the strong absorption of lactose monohydrate in this region.

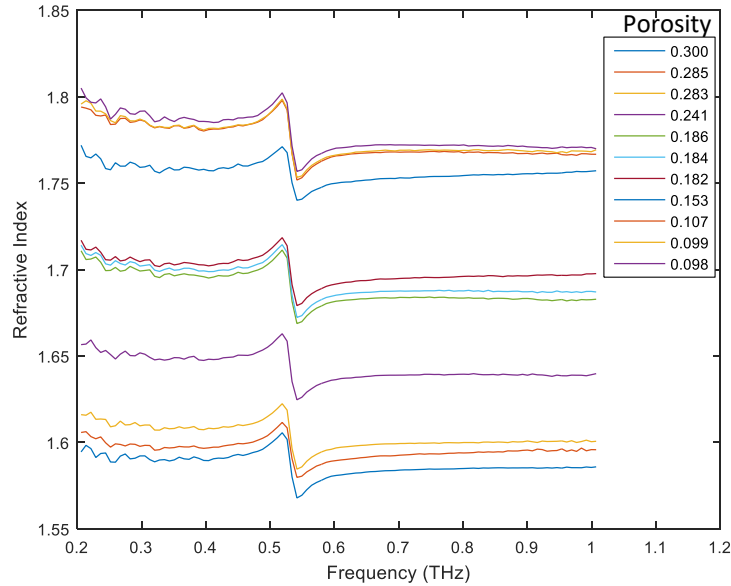


Figure 2.23: Frequency domain refractive index spectra of the calibration tablets

The impact of the dispersion effect on the time domain refractive index was investigated by comparison with the frequency domain refractive index. Since the time domain refractive index calculations generates one refractive index value for one tablet, one refractive index value was also obtained from the frequency domain refractive index method. This was achieved by taking the average frequency domain refractive index between 0.7 and 1 THz. The average of this region was used due to the absence of the dispersion effect and relative stability and consistency of the refractive index values. Figure 2.24 plots the effective refractive index values from both the methods against each other to determine their correlation and error. Results showed high correlation between these two methods with a correlation coefficient of 0.9964 and a low error between the two values of 0.007. Since the methods had good correlation, it was concluded that

the dispersion effect had minimal effect on the time domain refractive index values. Therefore, for development of all univariate refractive index based porosity models the time domain refractive index was chosen for its superior computational efficiency.

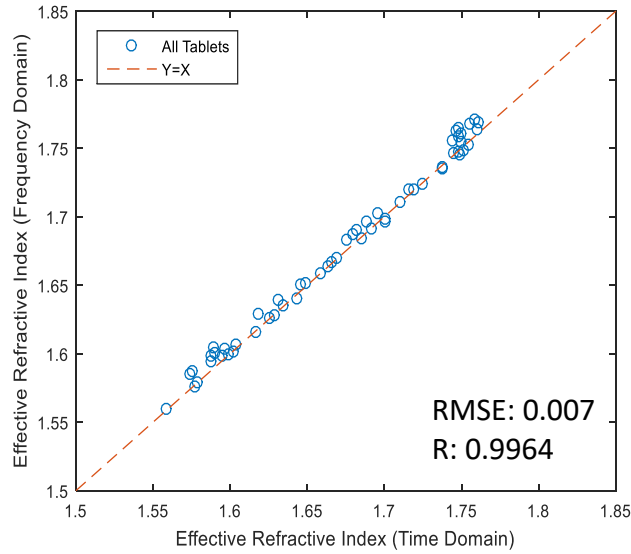


Figure 2.24: Correlation between refractive values from time domain method and frequency domain method

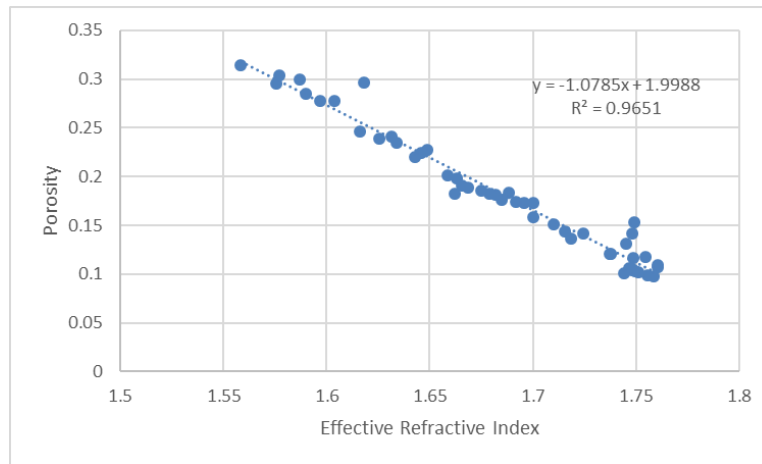
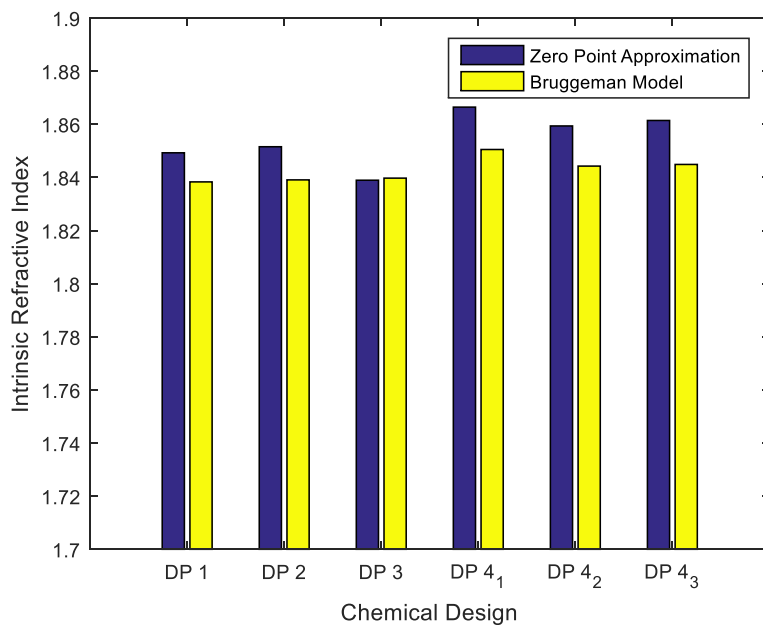


Figure 2.25: Porosity versus time domain refractive index

The time domain refractive index was used in the generation of three univariate porosity models. These models were generated to further evaluate the strong linear correlation between refractive index and porosity. Figure 2.25 confirms this correlation, showing a high correlation coefficient of approximately 0.97 between time domain refractive index and porosity when considering all the manufactured tablets.

Two out of the three univariate models considered the intrinsic refractive index. The intrinsic refractive index refers to the refractive index of a homogenous solid with a porosity of zero and is dependent on the chemical composition. Figure 2.26 shows the generation of intrinsic refractive index using the ZPA and Bruggeman models for each design point. Both the sample size and chemical composition effect on intrinsic refractive index was assessed. The sample size effect was assessed using the center point chemical design (DP4), thus, there are three values for chemical composition design point 4 (DP4<sub>1</sub>, DP4<sub>2</sub>, and DP4<sub>3</sub>) in Figure 2.26. The subscript of 1, 2, and 3 for the DP4 chemical design represents different sample sets used to generate the intrinsic refractive index. The DP4<sub>1</sub> set included 7 samples generated at all the compression force with low compression speed and tablet weight of 500 mg. Additional tablets with the low speed and the tablet weight variation were added to the DP4<sub>1</sub> set to generate the DP4<sub>2</sub> set of 11 samples. The DP4<sub>3</sub> set further included the tablets produced at low speed and, thus, represented the entire DP4 tablet set (15 samples). These results suggest the approximate 7 tablets that covered the required porosity range in the DP4<sub>1</sub> set was appropriate to determine the intrinsic refractive index of DP4 as addition of more samples caused minimal change (~0.01) in the calculated intrinsic refractive index for each model.

The chemical composition effect on intrinsic refractive index was also assessed. The intrinsic refractive index of the entire tablet set associated with the four chemical designs (DP1, DP2, DP3, and DP4<sub>3</sub>) was calculated and shown in Figure 2.26. The small chemical composition change across all the chemical composition design points produced only a small intrinsic refractive index change between approximately 1.84 to 1.87. Thus, the univariate models were hypothesized to be robust against these small chemical composition variations due to the low variation of intrinsic refractive index. It is important to note that the intrinsic refractive index values calculated from the ZPA model was generally higher than the values calculated from the Bruggeman model. The higher values from the ZPA model was potentially due to the pore structure of the tablets. The ZPA does not consider the pore shapes, thus, the model may overpredict the intrinsic refractive index. In contrast, the Bruggeman model considers the pore structure as homogeneously distributed spherical inclusions. Thus, the Bruggeman model may better represent the tablet systems of this study. This trend, however, was not observed for the chemical design DP3 as both the models generated very similar intrinsic values. This was potentially due to DP3 having the highest amount MCC in the formulation. Microcrystalline cellulose predominantly undergoes plastic deformation, therefore, was potentially able to fill in the void spaces more effectively. Thus, the effects of the pores size and structure was potentially reduced causing similar predictions for intrinsic refractive index from both models.



*Figure 2.26: Intrinsic refractive index of each chemical composition design using the zero porosity approximation and Bruggeman models*

Univariate models for predicting porosity were developed using ZPA and Bruggeman approximations. These models are shown in Figures 2.27 and 2.28. The calibration errors of these models were 0.0260 and 0.0159 void fraction for ZPA and Bruggeman, respectively. The Bruggeman model showed a lower error potentially due to a more accurate representation of the tablet system with effective medium theory. The decrease in relative error of the model in the porosity range of 0.1 to 0.3 from 13% for the ZPA model to 7.8% for the Bruggeman model further showed the superior accuracy of the Bruggeman model. The univariate model accuracy and robustness were further assessed by predictions on two different test sets. The first test set included tablets produced at lower speed with the same chemical composition as the calibration set. This test set was used to evaluate model robustness against new process parameter variation which in this case was compression speed. The prediction error of this test set was 0.0192 and

0.0088 for the ZPA and Bruggeman models, respectively. These results suggest that the both the models are robust against this process parameter variations due to the low prediction error with respect to the calibration error.

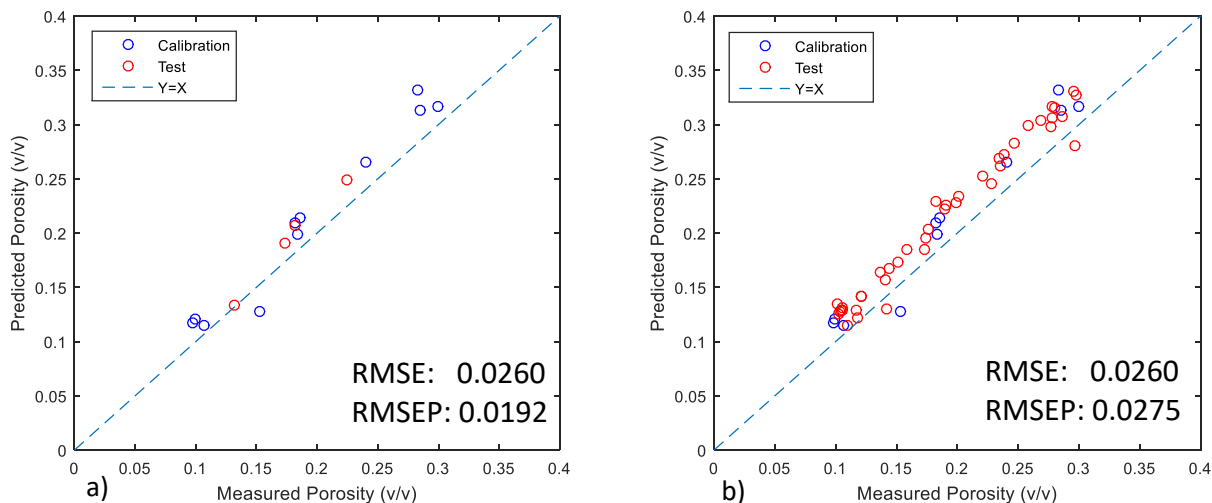


Figure 2.27: Zero point approximation model predicting test sets including process parameter variation (a) and chemical composition variation (b)

A second test set was used to evaluate the model robustness against chemical composition variation. This test set included tablets with three unique chemical compositions that were different than the calibration set. The prediction error had increased compared to the test set 1 result with 0.0275 for the ZPA model and 0.0126 for the Bruggeman model. This increase in prediction error is potentially a function of the large number of samples in this test set and the chemical composition difference between the calibration and test set samples. However, the prediction error is still relatively close to the calibration error, again suggesting that both the

models are robust against these chemical composition variations. In general, the Bruggeman model outperformed the ZPA model in prediction accuracy for both the test sets.

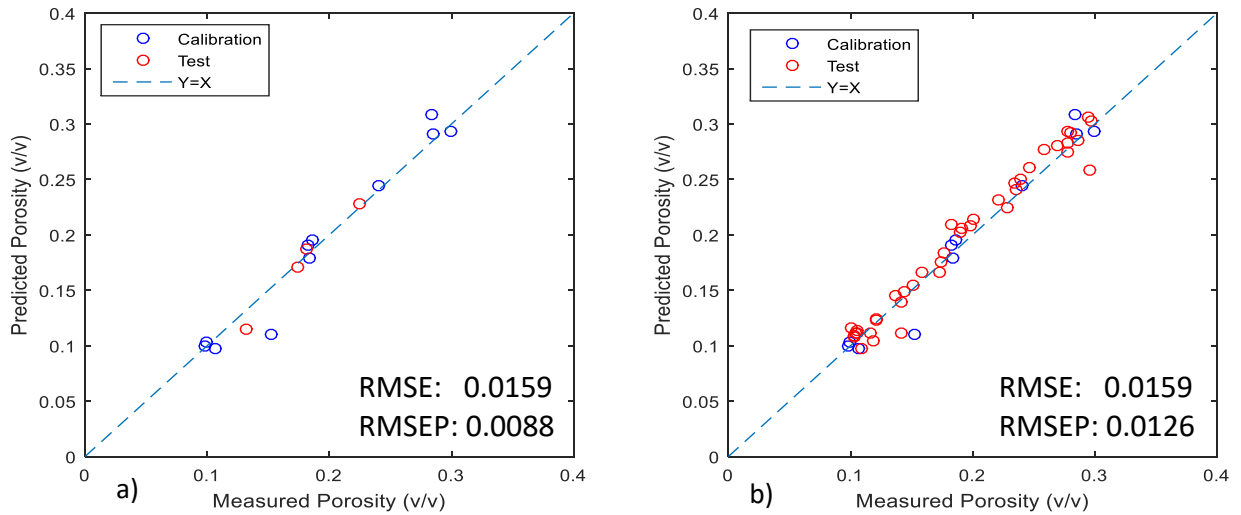


Figure 2.28: Bruggeman model predicting test set including process parameter variation (a) and chemical composition variation (b)

The robustness of these univariate models was shown to be adequate, however, the accuracy has a potential to improve, especially for the ZPA model. These model improvements may be achieved by considering the dispersion effect and the model assumptions. The dispersion effect, despite shown to have minimal contribution to time domain refractive index as previously explained with Figure 2.26, still may add to measurement error especially for the higher lactose monohydrate samples. The presence of the hydrate or moisture causes significant absorption and phase shift of the terahertz pulse at most frequencies.

In addition to dispersion effect, the model assumptions may be limiting the performance of ZPA and Bruggeman models. Both the models assume a two phase system comprising of solid and

void. However, the models differ in the interpretation of the two phases. For the ZPA model, the total volume of pores dictates the linear relationship between porosity and refractive index in a constrained range of 1 to the intrinsic refractive index and 0 to 1 for refractive index and porosity, respectively. Thus, this model does not consider the shape, size, and distribution of pores. The pore microstructure can also impact the model performance and could be a possible reason for the noticeable bias in the ZPA model. The Bruggeman model, in contrast, considers pore structure in the tablet to be spherical and uniformly distributed. Therefore, the Bruggeman model may represent the tablet system better than the ZPA model, especially for the higher porosity samples, in this study. The Bruggeman model has a potential for further improvement with consideration of an anisotropic Bruggeman model<sup>149</sup> which adds a shape factor in the Bruggeman model to allow for non-spherical pores. However, the tablet systems in this study seemed to be appropriately defined by the regular Bruggeman model. Another assumption for both the ZPA and Bruggeman model is that the refractive index is 1 at 100% porosity. Any moisture or particulates in the air during the terahertz measurements violates this assumption, thus adding bias to the model. Thus, appropriate purging of the air and environmental control at site of measurement is required to further mitigate the bias. In addition, applying bias correction methods may potentially account for these assumptions and causes for measurement error.

This study further investigated two additional models (linear regression and PLS). These models were purely empirical and did not require theoretical considerations of the tablet system as compared to ZPA and Bruggeman models. Thus, these models were considered to assist with further reducing the bias and error. The linear regression model was similar to the ZPA model, however, with no constraints in the range of refractive index and porosity. Therefore, the slope

was not dependent on the intercept for linear regression model. The model results are shown in Figure 2.29. The model has a calibration error of 0.138 which is significantly lower than the ZPA model and comparable to the Bruggeman model. Similarly, the prediction error on the test sets associated with process parameter variation and chemical composition are also low (0.0050 and 0.0128, respectively). These results suggest the bias and error associated with the ZPA model can either be reduced by considering a model that more appropriately represents the tablet system (*i.e.*, Bruggeman model) or a model that applies a purely empirical approach (*i.e.*, linear regression).

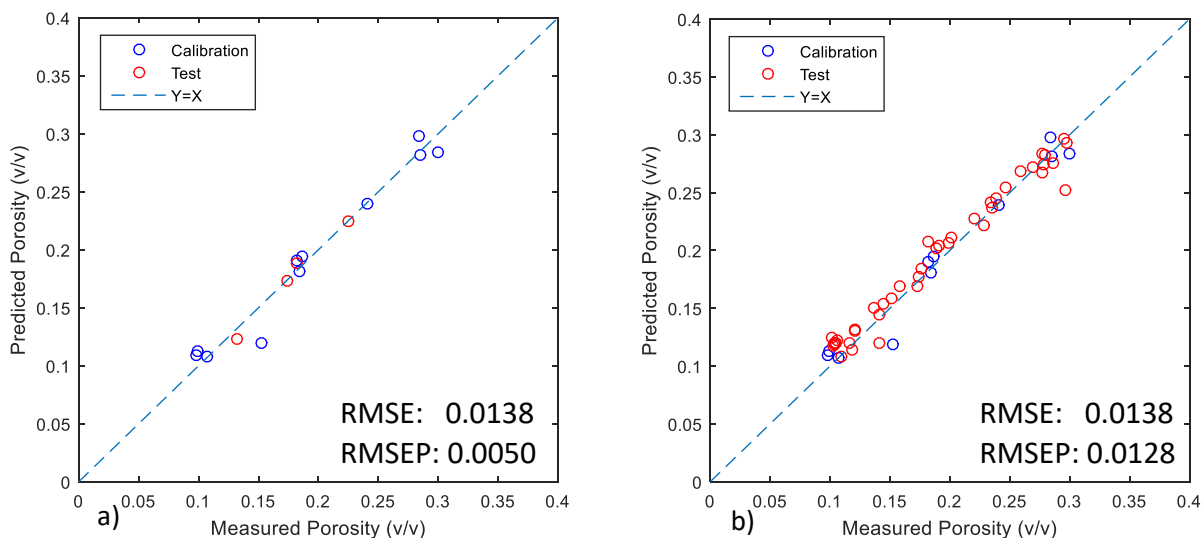


Figure 2.29: Linear regression model predicting test set including process parameter variation (a) and chemical composition variation (b)

The final refractive index based porosity model generated was a PLS model. This was a multivariate model developed with using the frequency domain refractive index spectra. This model was generated with effective refractive indices within the frequency range of 0.2 to 1 THz as this range shared covariance with porosity. No further preprocessing other than mean

centering was performed. Only two latent variables were used to develop the final model according to minimization of prediction error of both the test sets. It is important to include only the number of latent variables as required without exceeding the number of varying factors that are contributing to the orthogonal variations in the spectral dataset. The calibration set has chemical composition and various process parameter variations, therefore, including two latent variables is reasonable. Inclusion of a large number of latent variables leads to overfitting. The first two loadings are shown in Figure 2.30. These plots show the spectral shape associated with maximum covariance between refractive indices and porosity. The main spectral change associated with porosity is a baseline change shown by the first loading. The second loading highlights the dispersion effect which has very minor (0.06 %) covariance associated with porosity, potentially due to porosity effect on the degree of dispersion. Lower porosity means that the lactose monohydrate particles are tightly packed, allowing for the terahertz pulse to encounter more lactose monohydrate particles. This increased exposure of the terahertz to the crystalline material potentially results in a stronger dispersion effect.

The PLS model also significantly improved on the accuracy when compared to the ZPA model. The calibration error was 0.006, significantly lower than all the univariate models. The PLS model prediction error of both two sets was also low but comparable to both the Bruggeman and linear regression models (Figure 2.30). Specifically, for test set 1 the PLS model has the lowest prediction error (0.0046) when compared to all models. This is potentially due to the PLS model being more specific to chemical composition of the calibration set. The second test set prediction error was 0.0149 which was much higher than the calibration error. This suggests the model will operate appropriately in the current chemical composition range but may need to be updated for

larger chemical composition variations. The similarity of the prediction error from both the test sets for the PLS, Bruggeman, and linear regression models suggest that modeling with time domain or frequency domain refractive index yields similar results. However, for the multivariate modeling approach with frequency domain refractive index may perform better when the dispersion effects are more significant across a wider range of frequencies. This is owing to the ability to identify the refractive indices at the frequencies associated with high covariance to porosity and low effect from dispersion with multivariate techniques like PLS.

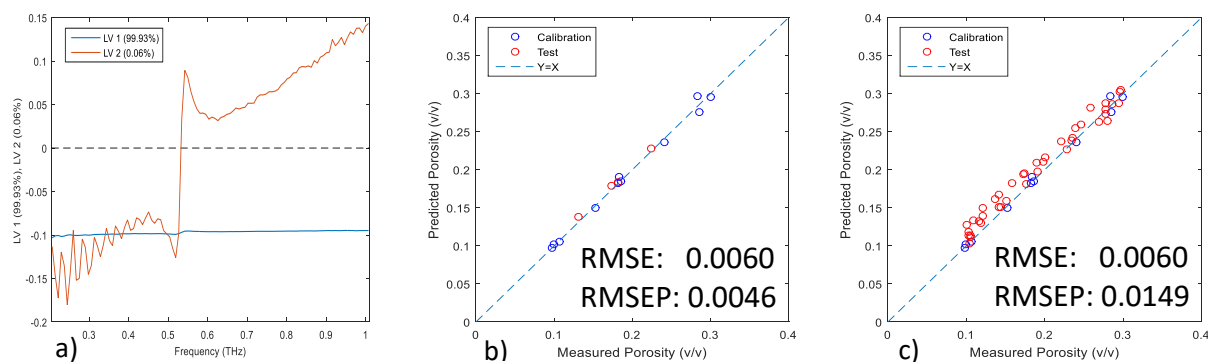


*Figure 2.30: MakeThe latent variables (a), predictions on test set 1 (b), and model predictions on test set 2 (c) of the PLS terahertz based porosity model*

The summary of the results is shown in Table 2.3 and suggests that all four generated terahertz based porosity models were robust against the process parameter and the small chemical composition variations in the range of this study. However, the prediction error increased when the models were applied on test set 2 with the new chemical composition variations. This may suggest that all the generated terahertz based porosity models may tend to fail at larger chemical composition variations. The PLS model showed the lowest prediction for test set 1 while the Bruggeman model showed the lowest prediction for test set 2. The univariate models offers a more computationally efficient means of generating the model using the time domain refractive

index. In addition, the theoretically based univariate models such as ZPA and Bruggeman model offer an increased understanding of the tablet system when the assumptions are followed. In contrast, the multivariate PLS model with frequency domain refractive indices is more complex, requiring Fourier transform of the original signal and knowledge of the appropriate chemometric methods. However, this model can be very accurate when the calibration set has all the relevant variation. In addition, the accuracy and noise can be potentially increased and reduced, respectively with appropriate frequency selection and removal. All the models are available to be used for PAT applications. The selection of the specific refractive index based porosity model is dependent on the model complexity and accuracy appropriate for the user and required for the intended PAT application.

Type of Model	RMSE	RMSEP (Process Parameter)	RMSEP (Chemical Design)
ZPA	0.0260	0.0192	0.0275
Bruggeman	0.0159	0.0088	0.0126
Linear Regression	0.0138	0.0050	0.0128
PLS	0.0060	0.0046	0.0149

*Table 2.3: Model summary (units of RMSE and RMSEP are in void fraction)*

## **2.4. Summary and Conclusion**

This study investigated the accuracy and robustness of four terahertz based porosity models on five component pharmaceutical compacts using two specific test sets associated with new process parameter and chemical composition variation respectively. Three of the models were univariate models based (ZPA, Bruggeman, and linear regression models) while the fourth model was a multivariate PLS model. The PLS model had the lowest prediction error for test 1 while the Bruggeman model had the lowest prediction error for test 2. The ZPA model had the highest error due to a potential high bias. This bias was reduced by theoretically assuming a more relevant tablet system (Bruggeman model) or by generating a purely empirical model (linear regression and PLS models). All the models showed robustness against the process parameter variation and small chemical composition variation. These models demonstrated accurate predictions within chemical range of this study. This study further demonstrated the strong potential of terahertz spectroscopy as a PAT tool for a roller compaction and tablet compression processes by assessing model robustness; a critical assessment in method validation.

## **Chapter 3: Development of refractive index based radial tensile strength model**

### **3.1. Introduction**

Pharmaceutical tablets are the most commonly used and widely preferred dosage forms. During tablet manufacturing, it is important to characterize the critical quality attributes (CQA) of the tablet to ensure that the product meets the required specifications for patient safety and efficacy. One such CQA for the tablet compaction process is mechanical strength. The mechanical strength is defined as the ability of the material to resist failure due to application of load in for example the compressive, shear, or tensile direction.<sup>154</sup> Tablets are required to be produced with an acceptable mechanical strength criterion to reduce tablet defects during tablet ejection (i.e. capping) and withstand post compression stages such as tablet coating, packaging, shipping, and handling. In addition, the mechanical strength indicates the bonding strength between the particles in a tablet.<sup>128</sup> The bonding strength often dictates the release kinetics of the drug and is a function of particle shape, particle size, elasticity/brittleness of the material, compression speed, and compression force.<sup>120-123</sup> Thus, important tablet properties such as the plasticity/elasticity<sup>24, 155-157</sup>, disintegration time<sup>1, 2, 5</sup>, and dissolution time<sup>3-5</sup> are also often characterized through mechanical strength testing. Therefore, implementation of reliable methods for quantifying the mechanical strength is essential for distinguishing between poor and acceptable quality products.

Multiple methods are available for determining the mechanical strength of tablets. One type of mechanical strength method involves applying a load until the material fails. This load is usually applied directly or indirectly in tension, the weakest failure direction, to obtain axial<sup>158, 159</sup> or radial<sup>154, 158-161</sup> tensile strength measurements, respectively. Other indicators of mechanical

strength include friability<sup>162, 163</sup> and hardness<sup>24, 129, 155-158</sup>. Both these methods do not require complete tablet failure; however, they still evaluate the resistance of the material to mechanical stress. Friability tests are designed to simulate the mechanical shock impinged upon tablets during post tableting stages (i.e. coating, shipping, and handling) with a rotating drum (friabilator). According to the United States Pharmacopeia<sup>162</sup>, a batch of tablets have acceptable friability when there is less than 1 % weight loss due to abrasion and friction after specified amount of drum rotations. However, many tablets (no less than 6.5 g) are required to perform this test. In contrast, hardness methods perform measurements on individual tablets. Hardness is a surface property which assesses the resistance of the material to plastic deformation. An indenter, with precise controls of load, speed, and depth of penetration, is usually used to produce an appropriate amount deformation to assess the bonding strength, plasticity/elasticity, and hardness of the tablet.<sup>155, 156</sup>

All the traditional mechanical strength methods, however, are destructive. Rapid and nondestructive methods are preferred to allow for further material testing and PAT capabilities. Previously reported PAT tools for mechanical strength include near infrared spectroscopy (NIRS)<sup>126, 132, 135, 136, 164-171</sup>, Raman spectroscopy<sup>139, 172</sup>, ultrasound<sup>173-175</sup>, and terahertz time of flight spectroscopy (THz-TOF)<sup>24, 25, 176</sup>. Studies for mechanical strength using NIRS and Raman spectroscopy operate on the principle of scattering loss due to porosity changes. A baseline shift in the spectra is an indication of this scattering loss and has been used to indicate mechanical strength. The surface features of the tablet also impact these spectroscopic measurements; which are primarily operated in reflectance mode. The reflectance is higher for harder and smoother tablet surfaces. Multivariate analysis is generally performed to extract features related to

mechanical strength (i.e. surface reflectivity and scattering) for quantitative method development. In contrast, ultrasound and terahertz time of flight often do not require the use of multivariate analysis; and primarily perform transmission measurements.

Transmission based PAT methods for mechanical strength are advantageous since they provide bulk material assessment. Both ultrasound and THz-TOF is able to measure the time of flight of a transmitted signal. However, the type of signal generated and transmitted through the tablet is different between these two techniques. Ultrasound transmits low intensity mechanical waves and measures the longitudinal speed of sound through the tablet. This speed of sound measurement can then be used to determine the Young's modulus of the sample. The Young's modulus has been shown to correlate with mechanical strength. However, this technique requires intimate contact with the tablet for effective transmission of the mechanical wave. This requirement does not apply to THz-TOF. Terahertz time of flight spectroscopy performs nondestructive and noncontact time of flight measurements of a transmitted terahertz pulse. The generated time domain signal contains information regarding absorption coefficient and refractive index at terahertz frequencies. Refractive index, a function of porosity, was also used to estimate Young's modulus.<sup>176</sup> This chapter further explored the relation between refractive index from THz-TOF and mechanical strength.

Pharmaceutical application for refractive index in solid oral dosage manufacturing has been increased with advancements in THz-TOF. Recent studies have used refractive index from THz-TOF to indicate porosity<sup>21, 23, 88, 145, 149</sup>, surface roughness<sup>110</sup>, disintegration time<sup>2</sup>, and dissolution time<sup>2</sup> for tablets. Measurements of mechanical strength such as breaking force and hardness have

also been characterized with THz-TOF.<sup>24, 176, 177</sup> However, the studies using THz-TOF for mechanical strength have primarily utilized the reflection mode of the instrument. To the current knowledge of the author, no studies have been reported using refractive index measurements from transmission THz-TOF to predict mechanical strength. Therefore, this study developed a refractive index based tensile strength model to further understanding the relationship amongst refractive index, porosity, and tensile strength. This model was developed on a pharmaceutically relevant multicomponent tablet system with variations in processing parameters and chemical composition. Thus, this study further expanded the application of refractive index measurements and showed the strong potential of THz-TOF as a PAT tool for tablet compaction.

## **3.2. Materials and Methods**

### **3.2.1. Materials**

A five component tablet system comprising of acetaminophen (APAP, Mallinckrodt Inc., Raleigh, NC, USA), microcrystalline cellulose (MCC, Avicel PH-102, FMC BioPolymer, Mechanicsburgh, PA, USA ), lactose monohydrate (Foremost Farms, Rothschild, WI, USA), starch (EMD Chemicals, Inc., Gibbstown, NJ), and magnesium stearate (MgSt, ThermoFisher Scientific, Waltham, MA, USA) was used for this study. Further details on these components and the manufacturing scheme are provided in sections 2.2.1. and 2.2.2. This tablet stem was chosen due to its resemblance to real pharmaceutical systems and to challenge the terahertz measurements with inclusion of a strong absorbing component (lactose monohydrate).

### 3.2.2. Experimental Design

Tablets were manufactured with the incorporation of process parameter and chemical composition variations. Specifically, two experimental designs using 4 levels of chemical composition, 5 levels of compression force (4.5, 7, 10, 13, and 18 kN), 2 levels of compression speed (2.4 and 240 mm/min), and 3 levels of tablet weight (450, 500, and 550 mgs) were used to create the tablets (Figure 3.31). A detailed description of the two experimental designs is provided in section 2.2.4. No further experimental controls were applied. Tablets were stored in a sealed container for one week to allow for viscoelastic recovery. Measurements of porosity, THz-TOF and radial tensile strength were then performed for the development of a refractive index based tensile strength model.

Design Point	APAP (wt fraction)	MCC (wt fraction)	Lactose (wt fraction)	Starch (wt fraction)	MgSt (wt fraction)
1	0.373	0.355	0.207	0.06	0.005
2	0.273	0.255	0.307	0.16	0.005
3	0.273	0.455	0.207	0.06	0.005
4	0.273	0.355	0.207	0.16	0.005

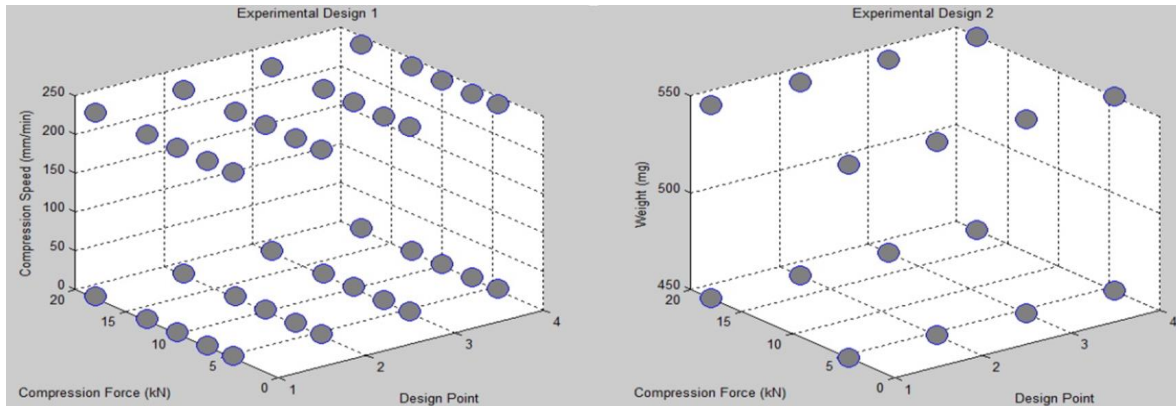


Figure 3.31: Experimental design

### 3.2.3. Tablet Porosity

Tablet porosity ( $\varphi$ ) was calculated by using the diameter ( $d$ ), thickness ( $l$ ), weight ( $m$ ), and true density ( $\rho_{true}$ ) of the tablet according to Equation 57. The dimensions of the tablet were measured with a digital caliper (model CO 030150; Marathon, Richmond Hill Ontario, Canada). The true density of the tablet was determined using the sum of the pure component true densities weighted to its respective weight fraction. The true density of the pure components were measured in powder form with a helium pycnometer (Quantacrhome Instruments stereopycnometer SPY-6DC, Boynton Beach, Florida). These porosity measurements were used to improve the understanding of the refractive index to mechanical strength relationship.

$$\varphi = 1 - \frac{4m}{\pi d^2 l \rho_{true}} \quad (57)$$

### 3.2.4. Terahertz Time of Flight Spectroscopy

Refractive index measurements were performed on the manufactured tablets using THz-TOF. Specifically, effective refractive index was extracted from the time domain signal. The time domain signal contains time of flight information of the terahertz pulse. The time delay between the transmitted pulse time domain signals with and without sample ( $\Delta t$ ), the speed of light ( $c$ ), and the tablet thickness ( $l$ ) were used to determine time domain refractive index (Equation 58). Effective refractive index is closely related to porosity, therefore, its capability to indicate mechanical strength was investigated. Frequency domain refractive index can also be calculated, however, according to chapter 2 both time domain and frequency domain were similarly related to porosity with this dataset. Therefore, this study only used time domain refractive index due to its superior computational efficiency.

$$n_{eff,TD} = \frac{c\Delta t}{l} + 1 \quad (58)$$

### 3.2.5. Radial Tensile Strength

Mechanical strength measurements were performed after the THz-TOF measurements. A diametrical compression tester (PTB 111E, Pharma Test Apparatebau AG, Germany) was used to determine the breaking force (F) required to cause tensile failure. The breaking force along with the diameter and thickness of the tablet were used to calculate the radial tensile strength (RTS,  $\sigma$ ) according to Equation 57. The RTS measurements were used to represent mechanical strength.

$$\sigma = \frac{2F}{\pi dl} \quad (59)$$

### 3.3. Results and Discussion

The relationship between refractive index and mechanical strength was investigated in this study. Refractive index is a measure of the speed of light in a sample relative to a vacuum. The ratio of the different types of medium (*i.e.* air and solid) present in the sample affects this relative speed. Therefore, refractive index is dependent on the porosity. Porosity is also a contributing factor for mechanical strength. A lower porosity results in greater particle-to-particle contact. Thus, interparticle bonds are more prevalent at lower porosities, resulting in a stronger tablet. Therefore, refractive index and mechanical strength were hypothesized to have a strong correlation due to their codependence on porosity.

The direct relation between refractive index and porosity was first confirmed. Time domain refractive index measurements were performed with THz-TOF. Figure 3.32 shows the trend between effective refractive index and porosity. There exists a strong linear relationship with a correlation coefficient of approximately 0.97 between these two factors. In addition, the root mean square error for the generated linear model is low with a value of approximately 0.01 void to tablet volume ratio. It is important to note that this strong linear trend exists across the process parameter and chemical composition variations achieved through the experimental design. Therefore, for this dataset the effective refractive index was able to appropriately define the porosity.

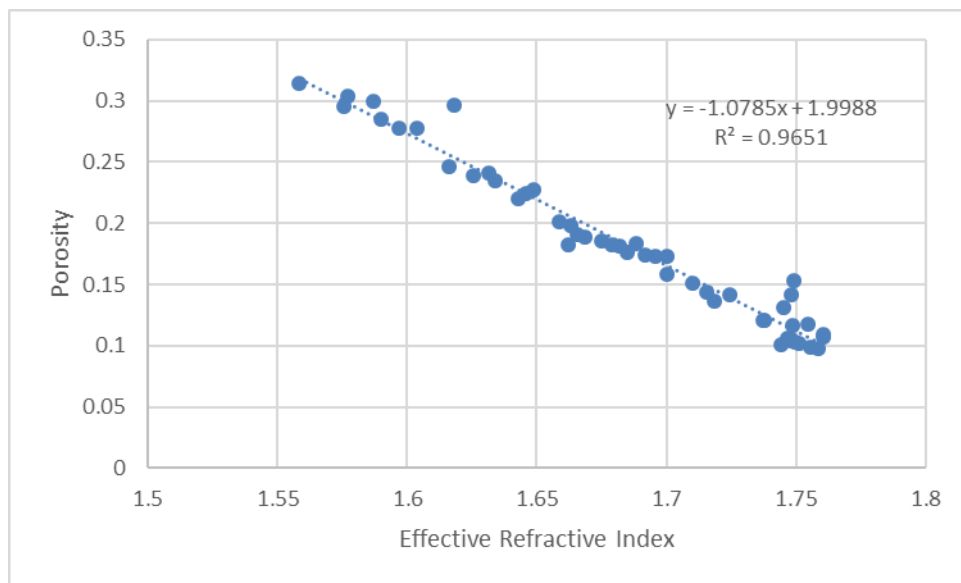


*Figure 3.32: Porosity versus effective refractive index trend*

Radial tensile strength measurements were performed to assess the relation between mechanical strength and time domain refractive index. The RTS values ranged from approximately 0.2 to 1.4 MPa. A few tablets were excluded from the dataset due to their low breaking strength being outside the instrument range. Figure 3.33 shows the trend between RTS and porosity, while

Figure 3.34 shows the trend between time domain refractive index and porosity. Both these trends are similar again showing the strong correlation between porosity and time domain refractive index. The general trend of RTS and porosity seems to be nonlinear. The RTS values were transformed by performing natural log to produce a more linear trend (Figure 3.2b). The results indicate a positive linear correlation between  $\ln(\text{RTS})$  and porosity. However, for both the transformed and non-transformed trend; there is a wide distribution of RTS and  $\ln(\text{RTS})$  at most time domain refractive index values.

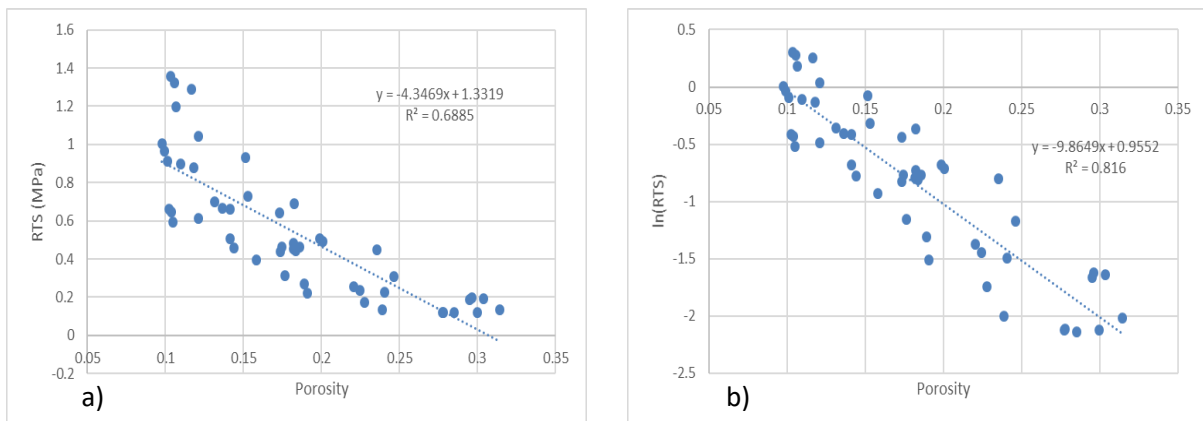


Figure 3.33: Porosity versus radial tensile strength (a) and  $\ln(\text{radial tensile strength})$  (b) trends

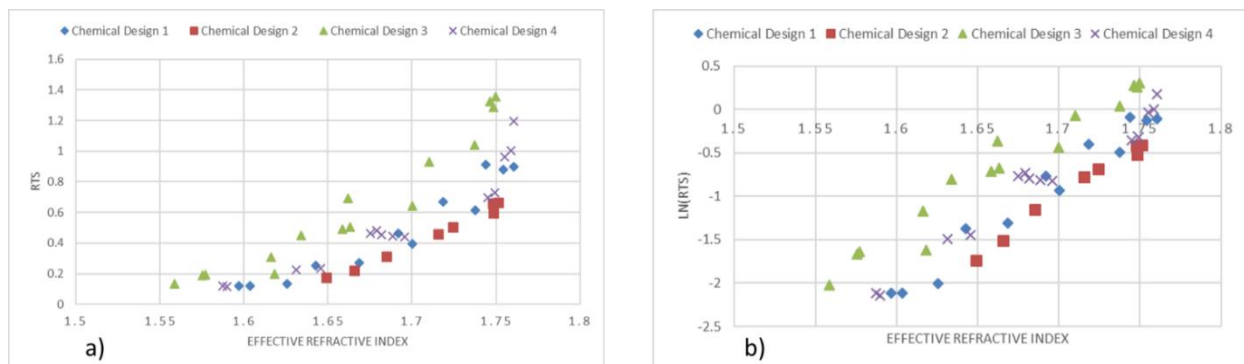


Figure 3.34: The trend between  $\text{RTS}(\text{MPa})$  and effective refractive index and between  $\ln(\text{RTS})$  and effective refractive index

The wide distribution RTS was potentially due to the chemical composition. The chemical composition did not affect the correlation between time domain refractive index and porosity; however, it is important factor for mechanical strength. Mechanical strength is not only dependent on the amount of interparticle bonds but also type of bonds and deformation behavior. The different chemical composition potentially varies the type bonds formed within the tablet. This was seen in Figure 3.34 as there is separation in the datapoints due to the chemical composition. The tablets manufactured with the composition associated with chemical design 3 produced the strongest tablets. In contrast, tablets from chemical design 2 produced the weakest tablets. This is primarily due to the variation in the MCC content. Chemical design 3 has the highest weight fraction (.455 w/w) of MCC while chemical design 2 has the lowest (0.255 w/w).

The amount of MCC in the tablet contributed significantly to the RTS due to its binding properties and deformation behavior. Microcrystalline cellulose is a linear chain of glucose allowing for efficient packing amongst the chains. Higher regions of contact allow for more opportunity for interparticle interactions. In particular, numerous hydrogen bonding occurs due to the many hydroxyl groups present in MCC. Therefore, the cohesivity between MCC particles is high resulting in enhanced binding capability. In addition to the strong binding capability, the deformation also contributes to the high mechanical strength of MCC tablets. Microcrystalline cellulose primarily deforms plastically, therefore, increasing the area for interparticle bonds.

Two modeling strategies were employed to account for the chemical composition effect on RTS. The first strategy was a global approach. One model encompassing all the samples variations was developed. For this global approach, a linear model was developed between the natural log transformed RTS and effective refractive index. This global model is shown in Figure 3.35 and was designed to be robust against the variations produced in this study. The model had a correlation coefficient of 0.81 and a root mean square error (RMSE) of 0.1783 MPa. The advantage of this global approach is that one model can be applied across a wide range of samples, reducing the user burden. This model has a reasonable accuracy with a relative error of approximately 15%. More accurate models may be required to distinguish poor quality products.

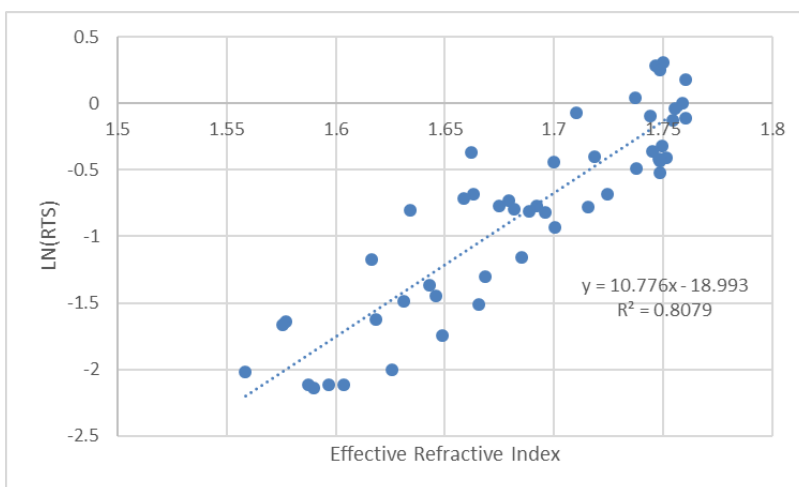


Figure 3.35: Model relating  $\ln(RTS)$  to effective refractive index generated according to global approach

The second strategy used was a hierarchical model approach. The tablet samples were separated into 4 classes associated with their chemical composition (chemical design). Four separate linear models were created between natural log transformed RTS and effective refractive index for each class. These models are shown in Figure 4.36. The procedure of using the hierarchical model involves first determining the chemical composition, then using the model specific to the chemical composition for prediction. All the models show strong linear correlation, with

correlation coefficients greater than 0.95. Therefore, these models suggest that the time domain refractive index and RTS are highly correlated across wide variety of process parameters but constant

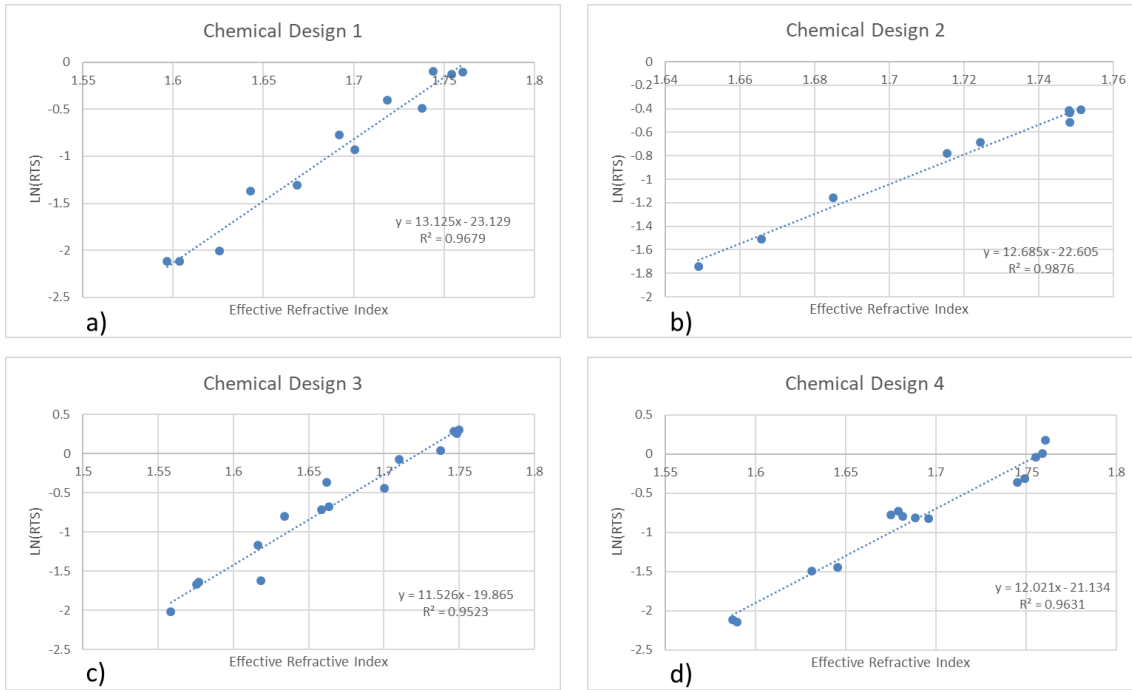


Figure 4.36: Linear models relating  $\ln(RTS)$  to effective refractive index for chemical design 1 (a), 2 (b), 3 (c), and 4 (d) according to hierarchal approach

chemical composition. The accuracy of the hierarchical model was significantly higher than the global model (0.0728 MPa RMSE and 6 % relative error). However, the hierarchical model approach is more complex than the global modeling approach, requiring development of multiple models and the extra effort of selecting the appropriate model. The decision for selecting between the two modeling approaches is dependent on the type of samples used and the required model performance (robustness vs accuracy). This study showed a strong correlation between

time domain refractive index and natural log transformed RTS which was significantly impacted by small chemical composition variations (10 % wt).

### **3.4. Summary and Conclusion**

Radial tensile strength measurements are commonly performed to determine the mechanical strength of tablets. These measurements, however, are destructive limiting any further tablet characterization. This study investigated using THz-TOF as a non-destructive method for measuring RTS. Terahertz time of flight spectroscopy is able to extract time domain refractive index which was shown to have strong linear correlation with natural log transformed RTS. With the chemical composition and process parameter variations presented in the tablet set used for this study, the generated linear model between time domain refractive index and  $\ln(\text{RTS})$  resulted in a correlation coefficient and RMSE of approximately 0.81 and 0.1783 MPa, respectively. The model error was improved by performing hierarchical modeling on the specific chemical composition. This approach improved the model from 0.1783 to 0.0728 MPa. This studied provided further support for THz-TOF as non-destructive and rapid tool for mechanical strength assessment.

## **Chapter 4: Development of refractive index based hardness model for intra tablet mechanical strength assessment**

### **4.1. Introduction**

Pharmaceutical tablets are the most commonly used and widely preferred dosage forms.<sup>178</sup> During tablet manufacturing, it is important to characterize the critical quality attributes (CQA) of the tablet to ensure that the product meets the required specifications for patient safety and efficacy.<sup>125</sup> One such CQA for the tablet compaction process is mechanical strength. The mechanical strength is defined as the ability of the material to resist failure due to application of load in for example the compressive, shear, or tensile direction. Tablets are required to be produced with an acceptable mechanical strength criterion to reduce tablet defects during tablet ejection (i.e. capping) and withstand post compression stages such as tablet coating, packaging, shipping, and handling.

Amongst the different aspects of mechanical strength (*i.e.*, tensile strength and hardness), indentation hardness enables both inter and intra tablet measurements. Intra tablet hardness is assessed by performing micro indentations at multiple locations of the surface.<sup>129, 155, 156</sup> Thus, hardness, an indicator of resistance to flow, is able to be mapped across the tablet surface. Assessment of the hardness gradient can be critical during research and development of tablets. A non-uniform hardness profile, caused by uneven stress distribution, increases the propensity of tablet defects during ejection.<sup>24, 128, 153, 179, 180</sup> Application of consistent compression force across the tablet and reducing the effect of die wall friction by appropriate lubrication strategies are critical to minimizing the occurrence of these defects.<sup>181, 182</sup> Therefore, the advantage of indentation hardness measurements to provide local mechanical strength information allows

pharmaceutical scientists to take appropriate formulation and processing decisions to improve physical quality and decrease tablet defects.

The limitations of the indentation hardness method, however, has reduced the widespread use of this technique in the pharmaceutical industry. The spatial resolution of this technique has a suggested lower limit of approximately 20 micrometers according to ASTM guidelines.<sup>183</sup> Often optical microscopy is used to verify the dimensions of the indentation, thus, further increasing the lower limit to the mm scale.<sup>155</sup> The spatial resolution is additionally affected with a minimum spacing between the indentations to reduce their interactions.<sup>183</sup> The measurement procedure is extensive, involving proper sample preparation and carefully controlled sample penetration. The sensitivity of indentation hardness measurement to dust at the surface, common in brittle materials, requires the sample to be appropriately polished to create smooth surfaces. After the tablet sample is appropriately prepared and properly secured, indentations are carefully performed with controlled force and speed. This procedure is repeated at multiple locations, often requiring optical microscopy images to determine the area of the indents for hardness calculations. The sensitive, timely and destructive nature of this method limits its use for routine measurements and process analytical technology applications. Therefore, alternative non-destructive methods of intra tablet mechanical strength are of particular interest.

Current options for non-destructive intra tablet mechanical strength methods include X-ray computed tomography (Xray CT)<sup>180, 184</sup>, near infrared chemical imaging (NIR-CI)<sup>128, 129, 185, 186</sup>, and terahertz time of flight imaging (THz-TOF)<sup>24, 25, 110, 187</sup>. The Xray CT method measures local X-ray attenuation coefficients of the sample at different orientation by sample rotation. These

coefficients are proportional to the density. Thus, three dimensional quantitative density images with high spatial resolution (approximately 0.1 to 10 micrometers) are able to be generated non-destructively with Xray CT. However, this method is still time consuming, thus, limiting its role as a process analytical technology (PAT) tool according to food and drug administration's guidelines<sup>125</sup>.

A commonly used PAT tool in most solid oral dosage processes is near infrared spectroscopy (NIRS). Intra tablet density and hardness is possible to assess with combining NIRS and imaging technologies (NIR-CI). Near infrared chemical imaging provides an NIRS spectrum at each pixel of the tablet image with a spatial resolution ranging from 10 to 200 micrometers.<sup>128</sup> This is a surface measurement technique as NIR-CI is generally performed in reflectance mode. Near infrared spectroscopy is sensitive to changes in density and hardness indicated by slope and baseline changes due to scattering.<sup>126</sup> Therefore, density and hardness maps are able to be rapidly and non-destructively created with NIR-CI. Another potential PAT tool for intra tablet mechanical strength assessment is THz-TOF imaging. This study further expands THz-TOF imaging application as a measure of indentation hardness. This technique has been utilized in reflective mode to obtain intra tablet surface refractive index (SRI) with spatial resolution as low as 0.1 micrometers.<sup>24</sup> The SRI values were shown to be highly correlated with crushing force.

Terahertz time of flight spectroscopy operates in the far-infrared region (approximately 300 GHz–3 THz or 10-100 cm<sup>-1</sup>). This specific range of low frequency induces crystalline phonon, intermolecular bond (hydrogen bonding), and torsion vibrations in pharmaceutical samples. The ability of this technique to extract refractive index of a solid sample has enabled unique

opportunities for characterizing physical properties. For examples, previous studies have shown density<sup>20, 21, 23, 88, 145, 148, 149</sup>, crushing strength<sup>24</sup>, and surface roughness<sup>110</sup> to be strongly correlated to refractive index related information from THz-TOF. These studies have primarily assessed inter tablet physical properties, however, there remains limited studies on intra tablet assessment with THz-TOF. A study by May et al.<sup>24</sup> generated surface refractive index (SRI) maps from THz-TOF to understand density distribution of tablets. However, only the average SRI of each tablet was used to indicate crushing strength and density. The conversion from a refractive index or an SRI map to a density or a hardness map requires appropriate pixel level reference measurements. In a recent study<sup>188</sup>, for roll-compacted ribbon density assessment, reference bulk density measurements were performed on strips cut from a ribbon. A linear model was then developed between the bulk density of the strips and the respective refractive index from THz-TOF imaging. This model was used to convert a refractive index map of a ribbon to a more pharmaceutically relevant density map. This strategy is difficult to apply to tablets due to the significantly smaller size, therefore, this study investigated indentation hardness measurements as reference for refractive index maps.

The objective of this study was to use THz-TOF imaging to assess intra tablet mechanical strength. Specifically, an indentation hardness model was generated. Indentation hardness is an indicator of tablet quality as it approximately estimates the intra tablet mechanical strength. This study provides the first example of using refractive index from THz-TOF imaging to non-destructively and rapidly quantitate indentation hardness. An example of a potential application of the indentation hardness model was demonstrated by assessing the effect of external

lubrication on hardness distribution. Therefore, the application of THz-TOF was expanded and its role as a potential process analytical tool was further supported.

## **4.2. Materials and Methods**

### **4.2.1. Materials**

For this study, a quantitative model was generated relating refractive indices at relevant terahertz frequencies to indentation hardness. Tablets with variation in mechanical strength and density were required for model development. These tablets comprised of only lactose monohydrate; a common excipient used as a diluent to assist in improving overall mechanical property of the tablet. Lactose monohydrate (Foremost Farms, Rothschild, WI, USA) was specifically chosen due to its strong absorption causing dispersion effect in the terahertz region. Dispersion effect in the refractive index spectrum from THz-TOF acts as an interferent for density and hardness modeling. Most pharmaceutical tablet formulation include lactose monohydrate and other crystalline components exhibiting strong absorbance in terahertz regions. Therefore, it is important to consider this interferent during model development.

### **4.2.2. Experimental Design**

The experimental procedure for generating the terahertz based indentation hardness model involved producing a set of five lactose monohydrate tablets. The target weight of these tablets was 500 mg and they were manufactured using a Carver press tooled with a 13 mm punch and die set. Five different compression forces of 2000, 3000, 4000, 5000, and 6000 lbs were used to produce the five tablets. Compression force was varied to create density and mechanical strength variation. The density variation was ensured with solid fraction measurements of all the tablets.

Solid fraction is the ratio of the bulk density to the true density. Bulk density was determined with tablet weight and dimensions; while the true density of lactose monohydrate was measured using a helium pycnometer (Quantachrome Instruments stereopycnometer SPY-6DC, Boynton Beach, Florida).

These five tablets were split into a calibration and a test set. The calibration set included tablets with compression force of 2000, 4000, and 6000 lb; while the test set included the remained two tablets at 3000 and 5000 lbs compression force. After a week of storage in ambient conditions to allow for viscoelastic recovery, the tablets were scanned with THz-TOF imaging, followed by indentation hardness measurements. Further description on the procedure of the THz-TOF imaging and indentation hardness are provided in subsequent sections (4.2.3 and 4.2.4). The calibration tablets were used to generate a refractive index based hardness model. The accuracy of this model was evaluated with the test set tablets. Three additional tablets were produced to demonstrate the potential application of this model. The first tablet was again produced using 4000lbs compression force to show that refractive index map of this tablet is able to be converted into a hardness map. The next two tablets were both produced at 3000 lbs compression, however, during production of one tablet external lubrication (mixture of magnesium stearate and methanol) was applied to the punch and dies to reduce the effect of die wall friction. Thus, the indentation hardness model was used to preliminarily assess the effect off lubrication on hardness distribution.

### 4.2.3. Indentation Hardness Measurements

Indentation hardness measurements were performed on tablets and used as reference measurements for a terahertz based hardness model. These measurements were performed using the Instron testing system (Instron universal testing system model 5869; Instron Corporation, Norwood, MA, USA), which allows precise control of the force and speed of the indenter. Specifically, a Vickers diamond tip indenter was utilized and attached to a 50 N load cell. The indentation hardness is calculated by determined the ratio between indentation force ( $F$ ) and indent area ( $A$ ) as seen in Equation 60.

The procedure for performing the indents involved appropriate instrument settings, estimation of indent area, and appropriate location of indents. The Instron was set with the following two settings; a maximum load of 10 N (held for 60 s) and compression/decompression speed of 10 N/min. These settings were sufficient to cause local material deformation. The indentation force and indent area are required to perform the indentation hardness calculations. The force used was the maximum load of 10 N and indent area was estimated by considering the pyramidal geometry of the Vickers indenter. The projected indent area is seen in Equation 61 and is dependent on the distance the indenter tip penetrates into the sample ( $H$ ). This distance was determined by extrapolation of the decompression profile near the maximum load to account for elastic recovery. It is important to do multiple indentation hardness measurements on one tablet sample to assess intra tablet hardness. Therefore, five total indentation hardness measurements were performed along two perpendicular lines. One indent was performed in the middle while the remaining 4 indents were performed 5 mm away from the center and at the ends of the two perpendicular lines. Each indent had dimensions of approximately 45  $\mu\text{m}$ . Appropriate THz-TOF

measurements at the approximate locations of the indentation hardness measurements were used during model development.

$$H = \frac{F}{A} \quad (60)$$

$$A = 4H^2 \tan^2 \theta \quad (61)$$

#### **4.2.4. Terahertz Time of Flight Spectroscopy**

Terahertz time of flight spectroscopy imaging in transmittance mode was used to measure the intra tablet refractive index of tablets. This instrument operates by initially producing 1560 nm laser pulse of 50 fs frequency from Laser 1. The laser pulses are directed to a photoconductor, which generates an incident 500 fs pulse. This pulse is directed at the sample where it can be reflected, transmitted, absorbed, or scattered. Another photoconductor collects the transmitted signal along with 1560 nm pulses from Laser 2. Laser 1 and Laser 2 are synchronized with Laser 2 undergoing variable time delay. Time domain signal is collected when the second photoconductor is simultaneously contacted by the transmitted terahertz pulse and the 1560 nm pulse from Laser 2.

The time domain signal needs further processing to generate refractive indices at terahertz frequencies. Both the time domain signal and the reference (measurement with no sample) are required to perform the necessary calculations for refractive index. Once these time domain signals are obtained, they are converted into frequency domain by Fourier transform. The frequency domain signal provides the amplitude and phase information for each of the present

terahertz frequencies. The effective refractive index (frequency domain refractive indices,  $n_{eff,FD}(\omega)$ ) at each of these frequencies ( $\omega$ ) is then calculated using the phase differences between the sample frequency domain signal ( $\vartheta_{s0}$ ) and the reference frequency domain signal ( $\vartheta_{r0}$ ) according to Equation 62. The frequency domain refractive index is also a function of the speed of light ( $c$ ) and sample thickness ( $X$ ). A hyperspectral dataset was generated with refractive index spectrum determined for each pixel of a tablet. The collections parameters included a frequency resolution of 7.6 GHz, a cumulated number of 128, and a spatial resolution of 0.4 mm. A 3 by 3 square of pixels and their respective refractive index spectra at the site of each indent were used to represent the indentation hardness measurements for model development.

$$n_{eff,FD}(\omega) = 1 + \frac{c}{X\omega} (\vartheta_{s0} - \vartheta_{r0}) \quad (62)$$

### 4.3. Results and Discussion

The application of THz-TOF as an indicator of intra-tablet hardness was evaluated. To achieve this objective, lactose monohydrate tablets were manufactured at five different compression forces. These tablets were first assessed with THz-TOF followed by destructive indentation hardness measurements. Figure 4.37 shows the frequency domain spectra obtained by applying Fourier transform to the initially generated time domain signal by THz-TOF. Figure 4.37a shows the mean absorbance spectrum of all the tablets in the frequency range of 0.1 to 1 THz. This is a truncated frequency region that was associated with an appropriate signal to noise ratio for this instrument. There is a significant peak present at approximately 0.5 THz. This peak is associated with a strong terahertz absorption of the lactose monohydrate component in the tablet. This strong absorption is also present in the refractive spectra as a dispersion effect (Figure 4.37b).

However, there is a strong baseline correlation with compression force even with the presence of dispersion. Increasing compression force, increased the tablet density which was positively correlated with refractive index.

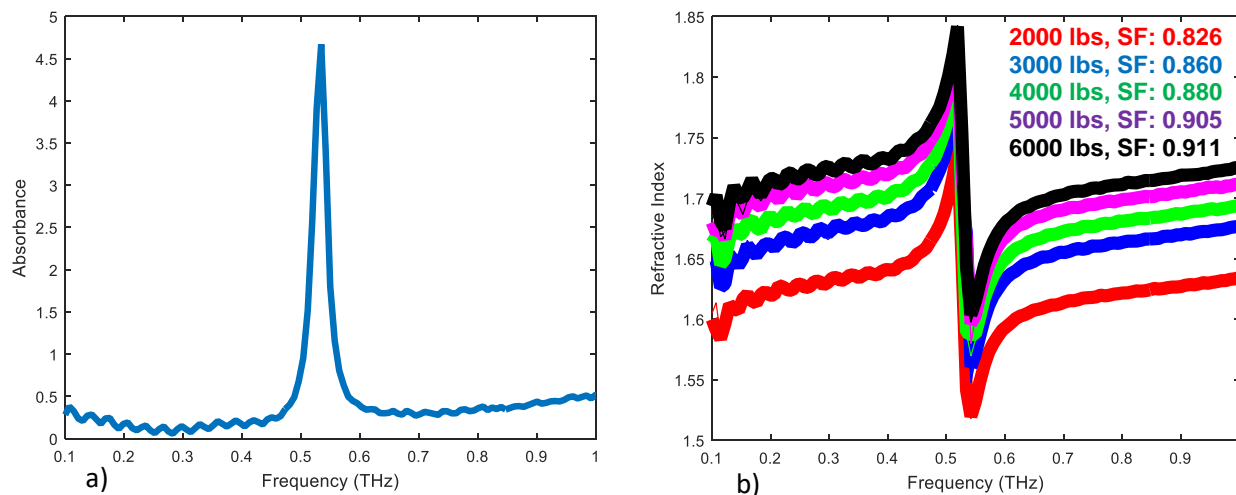
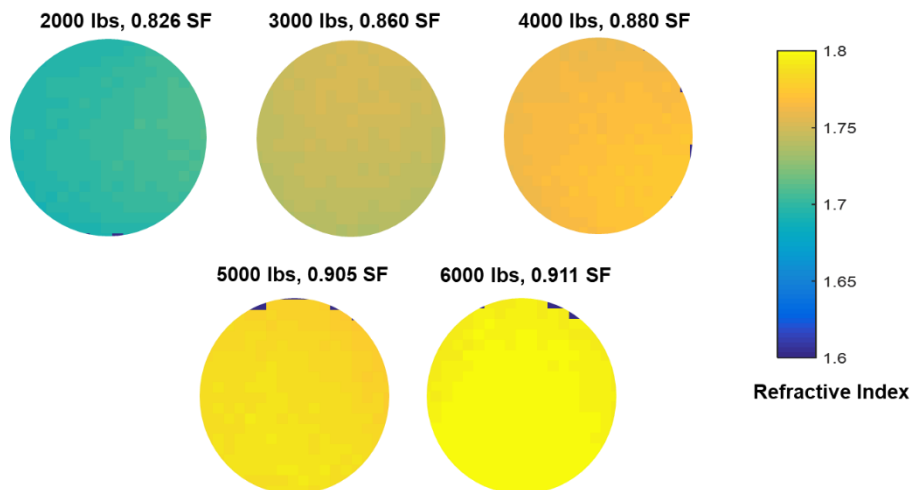


Figure 4.37: Mean absorbance spectrum of all tablets (a) and the mean refractive index spectra of each tablet appropriately color coded according the applied compression force (b)

The positive correlation with compression force and density was further verified by measuring the solid fraction of the tablets. The solid fraction is the ratio of the bulk density to the true density. The bulk density was calculated by using the tablet weight and dimensions of the tablet while the true density was determined using a helium pycnometer. Figure 4.38 shows that the tablet solid fraction ranged from approximately 0.82 to 0.91 and increased with compression force. This Figure also displays the refractive index images associated with 0.5 THz. This frequency is just before the distortion in refractive index spectrum due to dispersion and highly correlates with compression force and density. The refractive index profiles indicate the density

distribution. A model was generated to convert the intra tablet refractive index spectrum into a more pharmaceutical relevant quality attribute, hardness.



*Figure 4.38: Refractive index images at 0.5 THz of the five tablets produced with varying compression force*

The hardness of the tablet was defined by using indentation hardness test. For this test, a Vickers indenter was used and the compression profile was recorded as shown in Figure 4.39. According to this figure, the compression load increases at a precise rate of 10 N/min until the maximum defined load of 10 N is reached. An increase in compression load corresponds to an increase of depth of penetration of the indenter (compression extension). Calculations of indentation hardness was performed using the maximum compression load and depth of the indent. This depth was determined by appropriate extrapolation of the decompression profile to account for elastic recovery (Figure 4.39). These indentation hardness measurements were used as reference for a refractive index based hardness model.

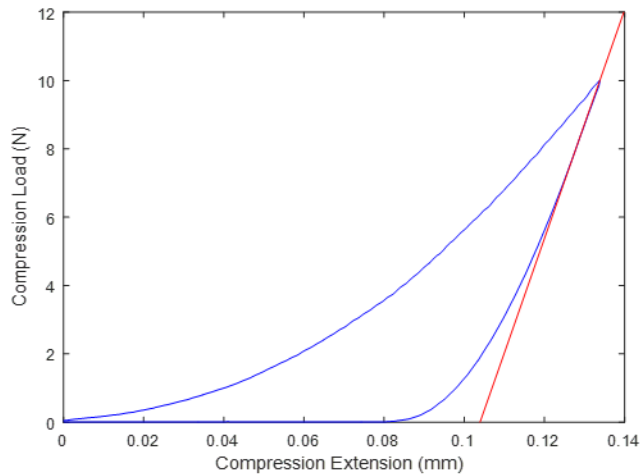


*Figure 4.39: Compression profile during indentation of lactose monohydrate tablet produced at 4000 lbs compression force. The blue trend represents the compression trend while the red trend represents the extrapolation performed to determine indentation depth.*

Indentation hardness measurements were performed at specific locations of the tablet to appropriately characterize the intra tablet hardness. Five total locations were chosen and seen in Figure 4.40, which covers the different regions of the tablets. Therefore, one tablet provided five reference values which were related to corresponding pixels of the refractive index images from THz-TOF. One pixel appropriately describes the entire indentation region as the pixel size is larger than the indentation size. However, 9 total pixels were selected at site of the indentation (one at the theoretical center and 8 surrounding pixels) to ensure the pixel area includes the indentation. The average refractive index spectrum of these nine pixels were related to the indentation hardness values. The tablet produced at 5000 lbs (SF: 0.905) compression showed the highest variation of intra tablet hardness and intra tablet refractive index at frequency of 0.5 THz of approximately 15 MPa and 0.02, respectively.

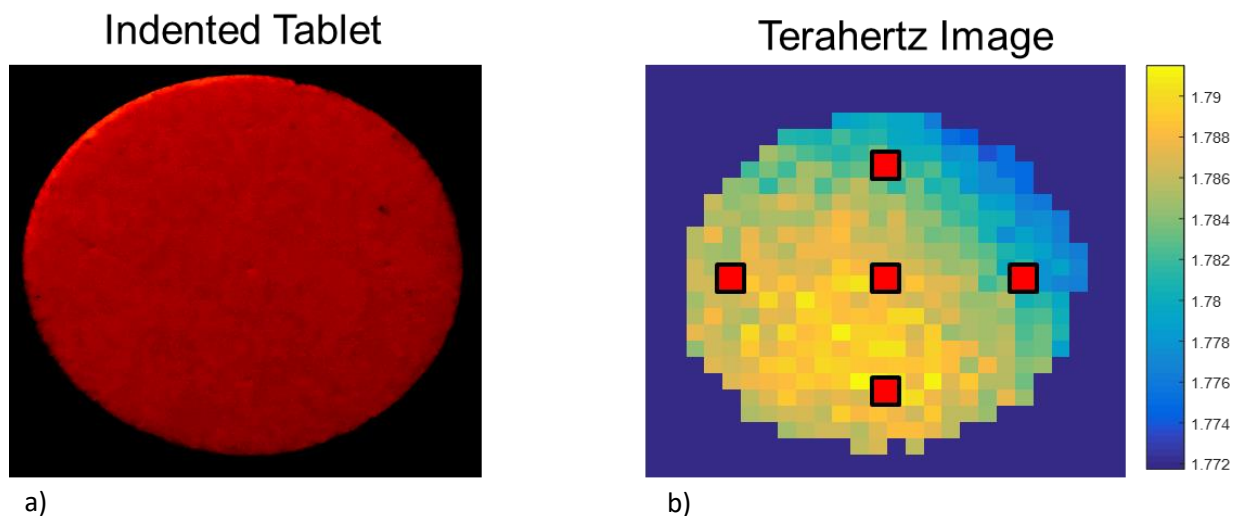


*Figure 4.40: Indented lactose monohydrate tablet produced at 4000 lbs compression force (a) and the corresponding pixels selected (b) for development of refractive index based model.*

A multivariate model was generated relating refractive index spectra to indentation hardness. Specifically, a PLS model was used in which the only preprocessing used was truncation of the refractive index spectra to include frequency range of 0.1 to 0.5 THz and the required mean centering for performing the algorithm. This truncation shown in Figure 4.41a was performed to enhance the accuracy of the model by removing the dispersion effect. A calibration model was built using tablets produced at compression forces of 2000 (SF: 0.826), 4000 (SF: 0.880), and 6000 (SF: 0.911) lbs, while the 3000 (SF: 0.860) and 5000 (0.905) lbs tablets were used to test the model. Two latent variables were chosen for the final model due to minimization of prediction error. The first two loadings capture approximately 99.89 % of the covariance (Figure 4.41b). The shape of these loadings further verifies increase in refractive index at all the included frequencies due to the change in compression force. The latent variable scores space in Figure 4.41c also shows that there is clear trend with compression force and that the test sample scores are including in calibration score space. A PLS model was generated between refractive index spectra and hardness resulting in a prediction error of approximately 4.94 MPa and correlation

coefficient of 0.98 (Figure 4.41d). The relatively high accuracy of this model suggests the PAT applicability of this THz-TOF based method.

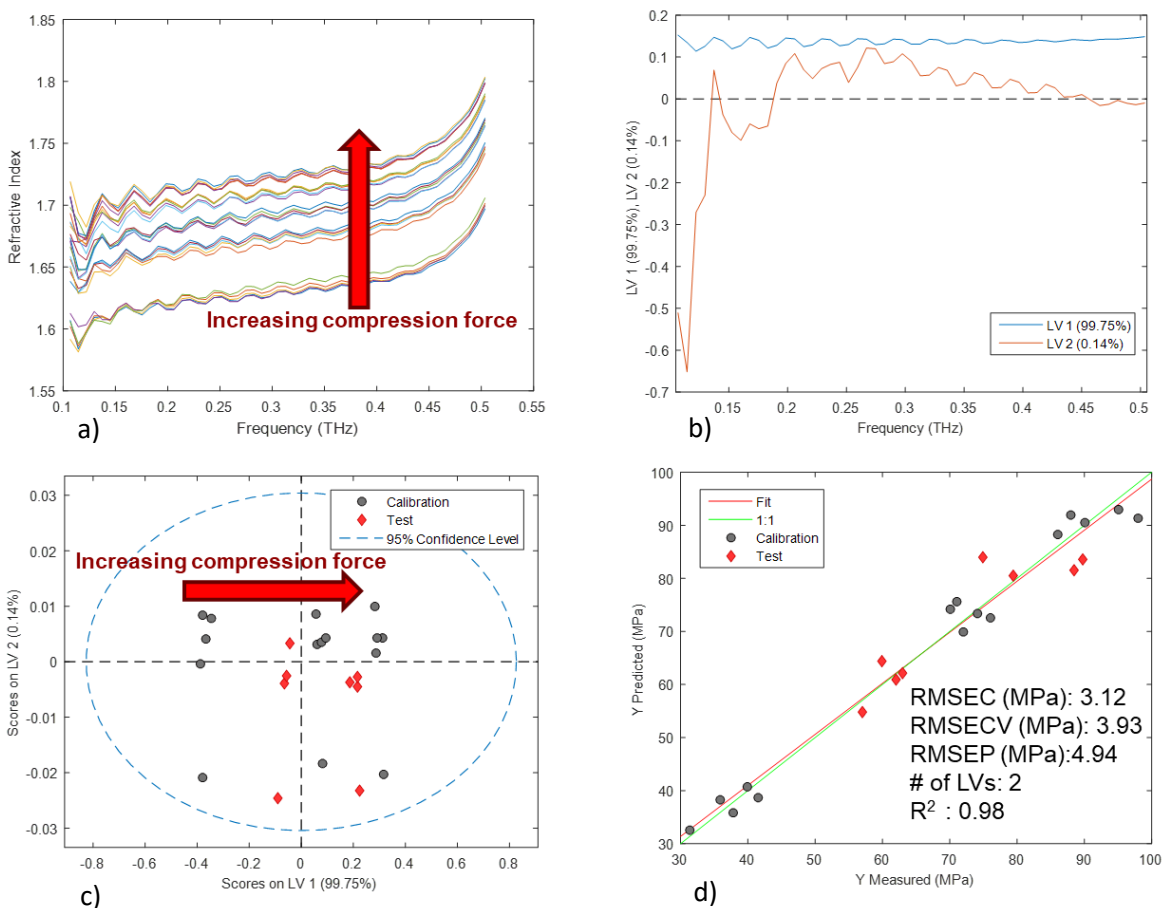
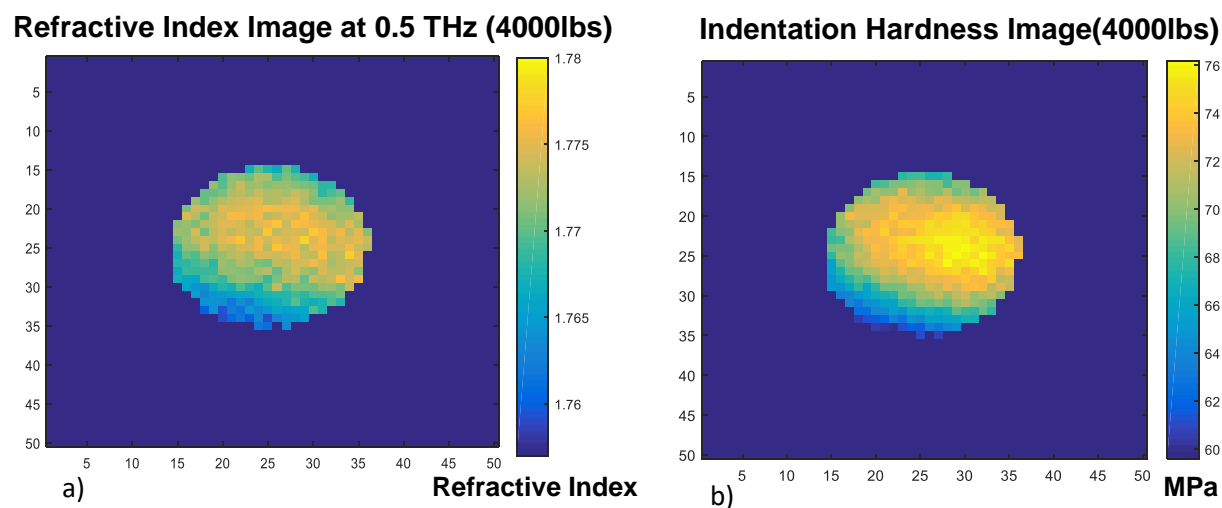


Figure 4.41: Truncated refractive index spectra (a) used for model development. The resulting latent variable (b), scores (c), and model results (c) plots for the developed PLS model between refractive index spectra and indentation hardness

The refractive index based hardness model was demonstrated on a new lactose monohydrate tablet produced at 4000 lbs (SF: 0.880) compression force. Figure 4.42a shows the refractive index map at 0.5 THz for this tablet. Qualitative assessment is possible with the refractive index map where lower regions of refractive index indicates lower hardness. However, the developed refractive index based hardness model was used to convert refractive index spectra into hardness values at each tablet pixel (Figure 4.42b). This model allows quantitative assessment of intra tablet mechanical strength. According to the hardness map in Figure 4.42b, the tablet has a

higher hardness at the center then at the edges. This hardness gradient is potentially a function of the die wall friction, filling, and load distribution. Lactose monohydrate tends to stick to the die wall due to cohesivity further affecting the hardness distribution. Inclusion of a lubricant or application of external lubrication of the die wall can help to mitigate the hardness gradient.



*Figure 4.42: Refractive index image at 0.5 THz (a) for a new tablet produced at 4000 lbs compression force converted into a hardness image (b) using the refractive index based hardness model.*

The impact of external lubrication on the hardness profile was assessed by producing two additional tablets. The tableting parameters such as the compression force (3000 lbs) were the same for both the tablets. The difference between the tablets was the application of external lubrication as one tablet was produced with application of an external lubricant (MgSt and methanol mixture) on the punch and die set. The tablet produced with lubrication resulted in a harder tablet with a higher solid fraction compared to tablet produced without lubrication according to Figure 4.43. This is potential due to the reduced die wall friction effect on the tablet with external lubrication and compression force variations. In addition, the hardness profile characteristics are different between the non lubricated and lubricate tablet as seen by the individually scaled hardness images in Figures 4.43a and 4.43c. This is more clearly seen in

Figure 4.44. The standard deviation for both the non lubricated and lubricated tablet is similar (approximately 2.70 MPa), however, the relative standard deviation for the lubricated tablet (3.72%) is lower than the non lubricated tablet (4.48%). In addition, the distribution for the non lubricated tablet is more skewed (skewness: -0.4016) and thus, deviates more from the normal distribution compared to the lubricated tablet (skewness: 0.0802) according to the QQ plot (Figures 4.44c and 4.44d). Inclusion of an internal lubricant in the formulation may further improve the hardness uniformity. Thus, the refractive index based hardness model can efficiently facilitate in critical material and processing decisions to enhance product quality.

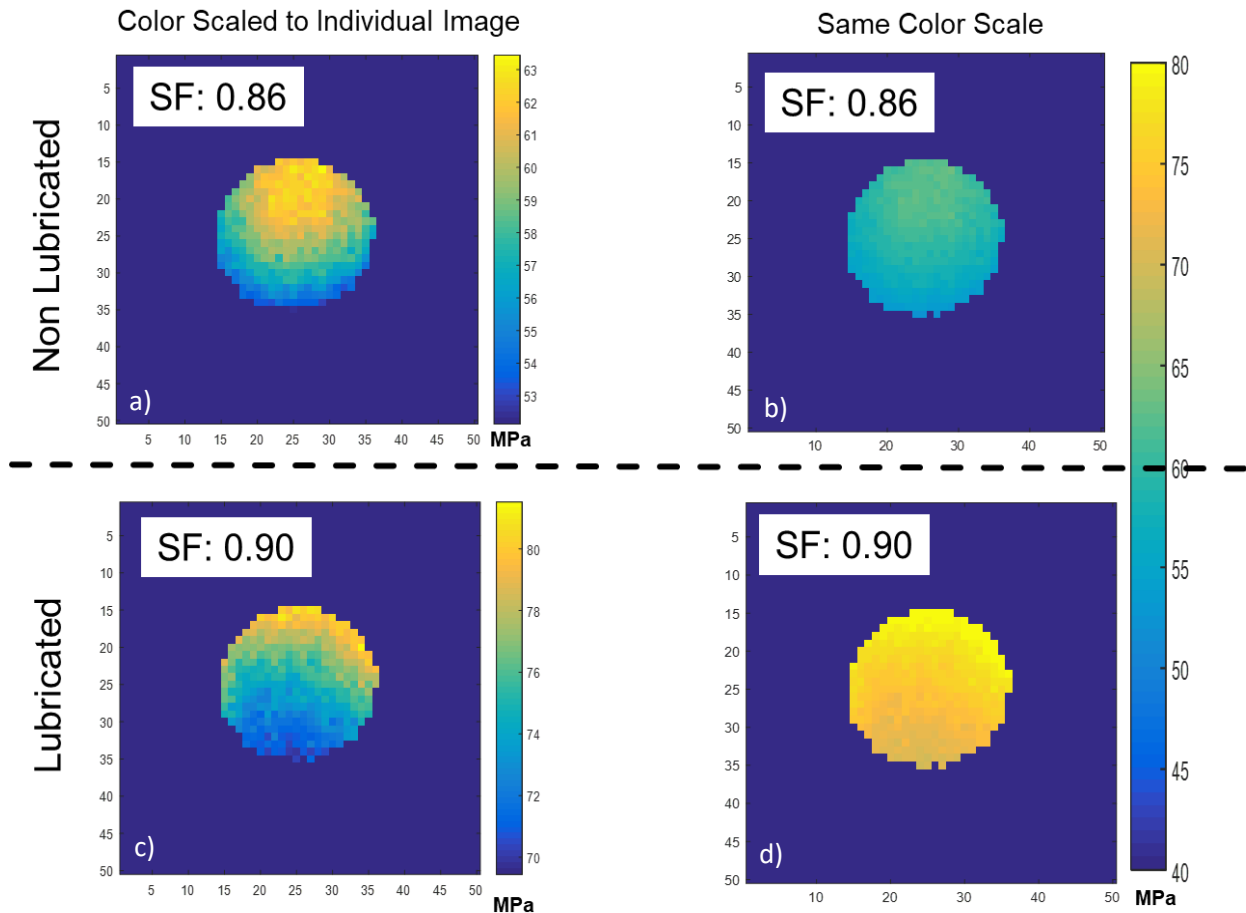


Figure 4.43: Lactose monohydrate produced at 3000 lbs with no external lubrication (a and b) and with external lubrication (c and d).

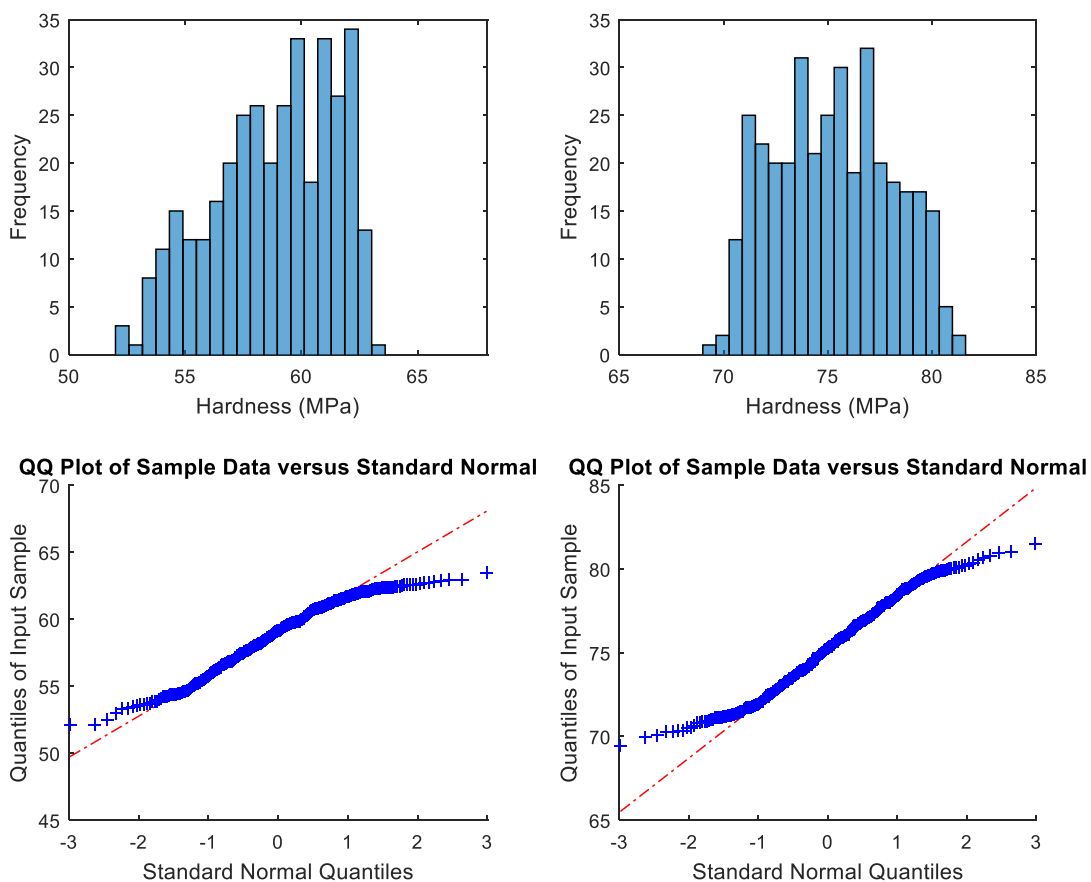


Figure 4.44: Hardness distribution and QQ plot for non-lubricated (a and c) and lubricated lactose (b and d) monohydrate tablets

#### 4.4. Summary and Conclusion

Indentation hardness measurements provide hardness profiles of the tablet, which are often correlated to intra-tablet mechanical strength. A non-uniform distribution in the hardness profile potentially increases the propensity for tablet defects. A hardness profile is typically generated by performing tablet indentations at different spatial locations. This is a destructive and time consuming method. Terahertz time of flight spectroscopy has the potential to non-destructively assess indentation hardness due to its ability to extract refractive index information. The relatively rapid identification of high risk (low hardness) regions within the tablet by THz-TOF

imaging allows pharmaceutical scientist to develop efficient strategies to mitigate these risks.

One such strategy is application of appropriate lubrication to reduce die wall friction. This study generated a quantitative hardness model from THz-TOF imaging and applied it to show the potential application in assessing different hardness distribution with varying factors such as external lubrication and compression force for lactose monohydrate tablets.

The model generated required the extraction of refractive index and indentation hardness of the tablets. Refractive index is a function of the tablet density, therefore, potentially indicates the mechanical strength. The time domain hyperspectral dataset collected with THz-TOF imaging in transmission mode was converted to frequency domain using Fourier transform to extract frequency dependent refractive index at all pixels associated with the tablet. Appropriately truncated refractive index spectra were related to indentation hardness measurements with a PLS model. This resulting model had a prediction error of 4.94 MPa and was shown to successfully convert refractive index spectral profiles of a tablet into a hardness profile.

The quantitative hardness model that was developed further demonstrated as a diagnostic tool for mitigating tableting defects. The hardness profile of a lactose monohydrate tablet was shown to have a non-uniform distribution. This non uniformity in hardness has a tendency to reduce the overall mechanical strength and increase the propensity of defects such as picking and sticking during tablet ejection. External and internal lubrication can be applied to mitigate these risks. Therefore, this study further demonstrates the potential of THz-TOF imaging as a non-destructive PAT tool for assessing the intra tablet mechanical strength.

## **Chapter 5: Investigation of the relationship between terahertz pulse reflections at the layer to layer interface to axial tensile strength for bilayer tablets**

### **5.1. Introduction**

Solid oral dosage forms are the most widely used and preferred forms of drug delivery. Advancements in solid oral dosage manufacturing allow development of complex tablet systems such as multilayered tablets. The production of a bilayer tablet involves sequential compaction of two layers. These tablets offer several advantages<sup>189</sup> including the incorporation of two chemically incompatible drugs<sup>190-193</sup>, the control of the release of the drug in each layer<sup>194-196</sup>, the reduction of dosing burden on patients<sup>197-199</sup>, the extension of the patent life of the product<sup>200</sup>, and the increase of drug efficacy<sup>191, 201</sup>. However, producing bilayer tablet with sufficient mechanical strength is often a challenge. Mechanical failure inherently occurs along the layer interface due to poor adhesion between the layer. Bilayer tablets with a weak adhesion strength results in tablet defects (i.e. lamination) during tableting, packaging, and shipping. Therefore, it is important to carefully characterize the mechanical integrity at the layer interface to reduce tablet failures and ensure that the product quality meets required standards set by the Food and Drug Administration.

There are multiple methods available to characterize the mechanical strength of bilayer tablets. Tensile strength methods have been previously employed for this purpose. Direct tensile strength measurements is performed by determining the fracture force in the axial direction.<sup>202</sup> Three-point bending tests have also been used to determine tensile strength.<sup>203</sup> Similarly, adhesion strength methods are also available as an indicator of mechanical strength. These methods also operates on causing mechanical failure at the layer interface by application of a shear force.<sup>204</sup>

Another mechanical strength test is friability. The tumbling motion of the friabilator simulates mechanical shock experienced by the bilayer tablets during downstream processing, shipping, and handling. A previous study<sup>25</sup> used a friabilator to characterize the delamination risk of bilayer tablets. All these mechanical strength methods are destructive, therefore, limiting opportunities for further testing.

Rapid and non-destructive techniques are preferred for real-time process assessment and process analytical technology (PAT) applications. A non-destructive option is relative density 3D mapping using X-ray micro-computed tomography.<sup>205</sup> These 3D maps identifies locations of fractures/cracks within a tablet. An increased presence of fractures significantly reduces the mechanical strength of tablets. However, this technique still does not fully comply as a PAT tool according to the FDA's quality by design guidance due to the extensive time required for each measurement.<sup>206</sup> Potential PAT tools for mechanical strength assessment of bilayer tablets include acoustics and spectroscopic measurements. Acoustic measurements of bilayer tablets were previously demonstrated to obtain mechanical properties such as Young's modulus and Poisson's ratio with a nondestructive/noncontact setup.<sup>207</sup> Spectroscopic techniques such as terahertz time of flight spectroscopy (THz-TOF) have also been used to assess interface adhesion strength.<sup>25</sup> This study further explored THz-TOF as a PAT tool for mechanical strength assessment of bilayer tablets.

Terahertz spectroscopy uses radiation in the far-infrared region of the electromagnetic spectrum (60 GHz–4 THz or 2-130  $\text{cm}^{-1}$ ). The low frequency radiation induces crystalline phonon vibrations, intermolecular bond vibrations (hydrogen-bonding), and torsion vibrations in

samples. Terahertz time of flight spectroscopy utilizes coherent ultrashort laser pulses allowing for rapid spectral acquisition (< 1 sec). The coherent laser pulse combined with time-gated signal detection enables extraction of both the electric field strength and phase information. The additional field's phase information allows direct determination of refractive index of the sample. Refractive index measurements are generally performed with a transmission setup of THz-TOF, however, a reflectance setup has also been used to assess the refractive index of the surface. The potential of THz-TOF as an indicator of physical tablet quality has been previously demonstrated due to the strong correlation between refractive index and tablet density.<sup>21, 23, 88, 148</sup>

The objective of this study was to assess the mechanical strength of bilayer tablets with THz-TOF in reflectance mode. The time domain signal generated in reflectance mode incorporates information regarding refractive index changes within the sample. Specifically, the intensity and time of a peak present in a time domain signal indicates the magnitude and sample depth of the refractive index change respectively. The study by Niwa et al.<sup>25</sup> defined surface refractive index (SRI) as the maximum peak intensity of the detected terahertz pulse reflected from the tablet surface. An interface index, acquired from an SRI map of the bilayer tablet, was shown to correlate with delamination risk of bilayer tablets. However, this study primarily focused on the tablet surface reflections and utilized only one formulation. In addition, friability assessment was used as reference to determine delamination risk. Multiple tablets are required to perform friability assessment; therefore, obtaining individual tablet mechanical strength reference measurements is not possible with this assessment. This study further advances the interpretation of the time domain signal by uniquely investigating the relation of terahertz pulse reflections at the layer interface to the axial tensile strength of individual tablets. Thus, a

quantitative model was developed to convert time domain signal from THz-TOF to axial tensile strength. This THz-TOF method was challenged by studying two different bilayer tablet formulations. Therefore, this study further demonstrated the PAT capabilities of THz-TOF on bilayer tablet systems.

## **5.2. Materials and Methods**

### **5.2.1. Materials**

Two sets of bilayer tablets were assessed in this study. These sets differed in the chemical component in each layer. Microcrystalline cellulose (MCC, Avicel PH-200, FMC BioPolymer, Mechanicsburgh, PA, USA) and lactose monohydrate (Foremost Farms, Rothschild, WI, USA) were in layer 1 and layer 2 respectively for the first set of tablets. The second set of tablets consisted of MCC in both the layers. These materials were chosen due to their contrasting spectral and mechanical properties. Terahertz radiation induces phonon vibration in lactose monohydrate due to the crystalline structure and the presence of a hydrate. Therefore, a strong peak is observed in the Terahertz absorption spectrum for lactose monohydrate. In contrast, MCC is mostly transparent in the terahertz region. Both MCC and lactose monohydrate also have differing refractive indices according to transmission THz-TOF measurements. Therefore, the contrasting spectral properties facilitated in highlighting the layer interface with THz-TOF allowing for improved characterization of adhesion integrity.

The second tablet set was manufacturing to challenge the THz-TOF method. The THz-TOF method for characterizing the mechanical integrity at the interface relies on refractive index changes within the sample. In the case of tablet set 2, there is minimal to no refractive index

change amongst the layers since the material is identical. However, fractures within the tablet creates areas of refractive index variations. Therefore, these fractures are potentially identifiable with THz-TOF, thus, allowing for characterizing of mechanical strength.

In addition to differences in spectral properties, the two materials also varied in mechanical properties. Specifically, the deformation behavior was different. The predominant deformation mechanism for MCC is plastic deformation. Therefore, the surface roughness of an MCC compact decreases during consolidation. Surface roughness of the first layer often dictates the interfacial strength of a bilayer tablet. In contrast, lactose monohydrate predominantly deforms through brittle fracture. Hence, consolidation of lactose monohydrate results in particle fragmentation. These fragmented particles reveal new surfaces which permit more particle-particle interactions between layers. The number of particle-particle interaction at the interface also dictates the interfacial strength. Therefore, bilayer tablets with a wide range of interfacial strength was created by appropriate material selection and process parameter variation to test the THz-TOF mechanical strength method.

### **5.2.2. Experimental Design**

Bilayer tablets were manufactured with two different chemical formulations. One formulation comprised of MCC in layer 1 and lactose monohydrate in layer 2 (MCC-Lac); while the second formulation had MCC in both the layers (MCC-MCC). A total of five tablets were produced for each of the two formulations. The factor that was varied amongst the two tablet sets was tamping force (0, 1, 3, 5, and 7 kN). This range of tamping force created an appropriate variation in interfacial strength between the tablets. Factors that were kept constant were the main

compression force (15 kN), the compression speed (10 mm/min), the layer sequence (MCC was in layer 1 for all tablets), and the material weight of each layer (200 mg).

The selection of these constant factors was based on consideration of the interfacial strength and subsequent mechanical strength characterization methods. A high main compression force and a relatively slow compression speed was chosen to initiate deformation and create more intimate contact between the layers. Similarly, MCC was placed in layer 1 to vary the mechanical interlocking of the layers. The material weight of 200 mg for each layer was chosen to facilitate in the axial tensile strength and THz-TOF measurements. Axial tensile strength measurements require both the top and bottom surface of the bilayer tablet to adhere on to the two opposing platens. The smaller the tablet, the more sensitive the measurement is to the application and strength of the adhesive. A 400 mg bilayer tablet was deemed appropriate for these measurements according to previous trials. The THz-TOF measurements also depend on the layer weight. The depth of the interface determines the time the reflection signal returns. If the tablet is too small then the surface reflection and interface reflection interact and become indistinguishable. The 400 mg bilayer tablets resulted in appropriate separation of these two reflections. However, the reflection of the opposite end of the tablet was not visible in the time domain signal due to the large tablet thickness. The edge reflection is not critical for characterizing the interfacial strength, however, two additional tablets at 5 kN tamping force and 150 mg weight of each layer (and all other factors the same) was also produced to visually show all the significant reflections. All the produced tablets were stored in ambient conditions for a week to allow for viscoelastic recovery before performing THz-TOF measurements followed by axial tensile strength measurements.

### 5.2.3. Terahertz Time of Flight Spectroscopy

Bilayer tablets were measured with THz-TOF using TAS7500IM (Advantest, Tokyo, Japan).

Spatially resolved time domain signal were collected with reflectance geometry. The acquisition parameters of spatial resolution, cumulative spectral number, and sampling frequency was set to 0.2 mm, 128, and 7.6 GHz, respectively. For the MCC-Lac tablets, both sides were measured to assess the effect of positioning on time domain signal. Only one position (layer 1 facing the detector and terahertz source) was measured for the MCC-MCC tablets since both the layers had the same material. The time domain signal was processed by high frequency filter to improve the signal to noise ratio and mitigate the effect of multiple reflections on the time domain signal. The intensity of the reflected signal from the layer interface was used as indicator of interfacial integrity.

### 5.2.4. Axial Tensile Strength

The axial tensile strength was measured using a texture analyzer (TA.XT Plus, Texture Technologies, Scarsdale, NY). The measurement procedure will involve fixing the side of the tablet corresponding to the second layer to a steel bar. The first layer side was adhered onto a SEM stub attached to a load cell (approximately 100 lbs). Tensile force was applied until complete failure of the bilayer tablet. The load cell displacement rate was set at the minimum allowable value of 0.005 mm/s. The tensile strength ( $\sigma_t$ ) was calculated according to Equation 63 where 'F' and ' $\phi^2$ ' are the force required to debond the tablet and diameter of the tablet respectively.

$$\sigma_t = \frac{4F}{\pi\phi^2} \quad (63)$$

### 5.3. Results and Discussion

In this study, THz-TOF was used to assess adhesion integrity of bilayer tablets. Reflectance measurements were performed on two different sets of bilayer tablets. However, some monolithic tablets were also scanned for comparison. Figure 5.45a and 5.45c shows the average time domain signal of pure lactose monohydrate and MCC tablets produced at a weight of 300 mg. There are two primary reflected pulses visible in the time domain signal at approximately the same time for both the pure component tablets. The first reflected pulse at approximately 5 ps corresponds to the air to tablet surface interface. The next major reflected pulse occurs at approximately 25 ps due again to the tablet surface and air interface, however, at the opposite end of the tablet. Therefore, any signal present in between these two reflections is associated with refractive index changes or absorption within the tablet. Pure component tablets are generally chemically and physically homogenous, therefore, are not expected to produce pulse reflection from within the tablets. This is seen in Figure 5.45c as no significant reflections occur inside the tablets. However, there seems to be pulse reflections in the lactose monohydrate tablet. These apparent reflections potentially occurred due to the strong absorption of lactose monohydrate and multiple reflections. Therefore, these apparent reflections act as an interference for determining the mechanical integrity. High frequency noise removal was utilized to minimize these interferences. Figure 5.45b and 5.45d show the time domain signal after appropriate frequency filter (>60 THz). This frequency filter was chosen as removing any lower frequencies resulted in removal of the reflection signals of interest. The absorption effect in the lactose monohydrate tablet is still present but reduced after the frequency filter (Figure 5.45b). All subsequent time domain signals were preprocessed with this frequency filter to only highlight the reflected pulse at the layer interface for bilayer tablets.

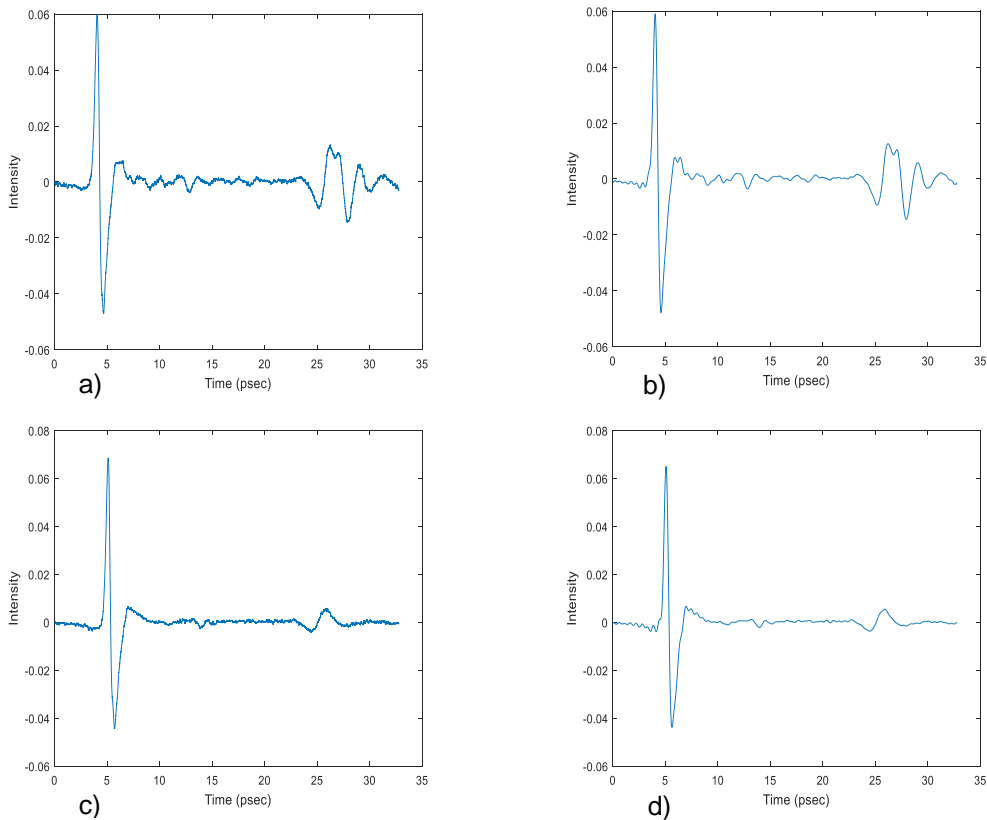


*Figure 5.45: Pure lactose monohydrate and MCC raw average time domain signal (a and b) and preprocessed with frequency filter (b and d)*

The mean time domain signals for multicomponent monolithic and bilayer tablets are also shown in Figure 5.46. These tablets were also produced with a total weight of 300 g (150 g in each layer for the bilayer tablets). Figures 5.46a and 5.46b show monolithic tablets that are pure MCC or mixture of MCC and lactose monohydrate. The reflected pulses present in these time domain signals are similar to the pure component tablets with two primary reflections at the beginning and end of the tablet. However, a new significant reflected pulse appears for the bilayer tablets due to the layer interface. Both the MCC-MCC and MCC-Lac bilayer tablets show the interface reflections in Figures 5.46c and 5.46d. It is important to note that the MCC side of the bilayer is

facing the terahertz source and detector for the MCC-Lac bilayer tablets. Therefore, the reflections at the layer interface is potentially associated with the refractive index changes from MCC to air void, MCC to lactose, and/or air void to lactose for the MCC-Lac bilayer tablets. Presence of voids at the layer interface is potentially due to the presence of fractures/failures. This can be further confirmed with the MCC-MCC bilayer tablet. There is still an interface reflection present in the time domain signal for this tablet. This interface reflection is most likely due to the presence of voids since both the layers are the same, thus, having similar refractive indices. Therefore, the interface reflections may indicate the interfacial strength.

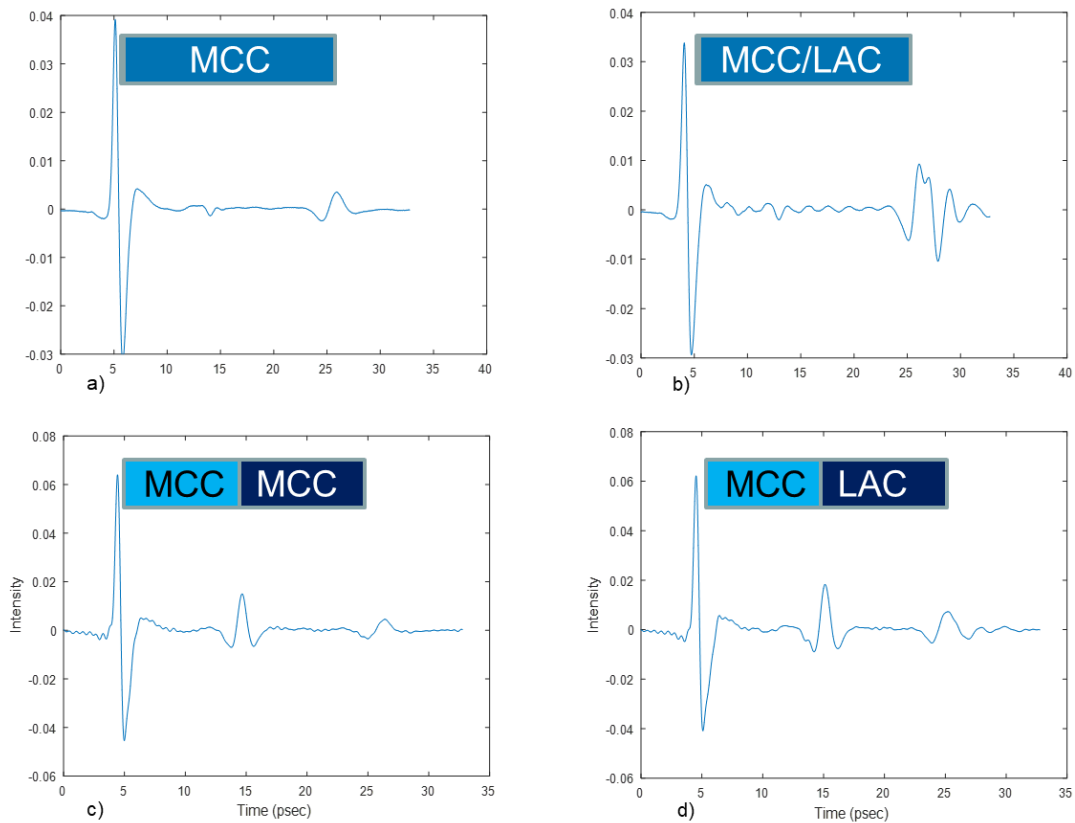


*Figure 5.46: Mean time domain signal of monolithic MCC (a) and MCC/lactose mixture (b) tablets and bilayer MCC-MCC (c) and MCC-Lactose (d) tablets.*

Two sets of tablets were manufactured to investigate the effect of layer interface reflections on interfacial strength. The tablet weight for all these tablets was increased to 400 mg (200mg for each layer) to separate the tablet surface reflection and interface reflection, thus, reducing their interaction. Also, a larger tablet was required to perform accurate axial tensile strength measurements. The two tablet sets differed in the chemical composition (MCC-Lac and MCC-MCC bilayer tablets). Five tablets, varying in tamping force, were produced in both the sets. The tamping force affects the interfacial strength by varying the mechanical interlocking at the layer interface. Therefore, bilayer tablets with different levels of mechanical strength were achieved.

Figure 5.47 shows the mean time domain signal of the five MCC-Lac bilayer tablets. Two primary reflections are observed in these signals. The tablet surface reflection is the first main signal received by the detector at approximately 5 psec. The intensity of this first peak generally increases as the surface gets smoother and denser (*i.e.* higher refractive index). However, at tamping forces of 5 and 7 kN the intensity of the first seems to decrease. This is primarily due to a decrease in tablet thickness. The terahertz instrument positions all the tablets in the same location. Therefore, a significant decrease in the thickness results in a longer distance between the tablet surface and terahertz source. This increases the path length causing a reduction in reflection intensity. Standardizing the distance between the tablet surface and terahertz sensor may results in a better interpretability of the first reflection. The second major reflections are seen at approximately 25 psec (Figure 5.47). These reflections are indicative of the layer interface. The intensity of these reflections is increasing with tamping force. The mechanical interlocking at the layer interface is reduced at higher tamping force. This results in a more

prominent interface at higher tamping forces with the potential presence of fractures. Thus, the intensity of the interface reflection was used to indicate the intra and inter interfacial integrity.

Intra tablet interfacial integrity was assessed by using spatially resolved measurements of THz-TOF. These measurements provide time domain signal at multiple locations of the tablet. A map of the layer interface intensity was generated for each bilayer tablet (Figure 5.48). These maps locate regions of strong refractive index changes at the layer interface. These high intensity regions are potentially associated with weak interfacial strength. This strength weakens in more locations with increasing tamping force. The mean intensity was used to represent the interfacial strength for inter tablet mechanical strength assessment.

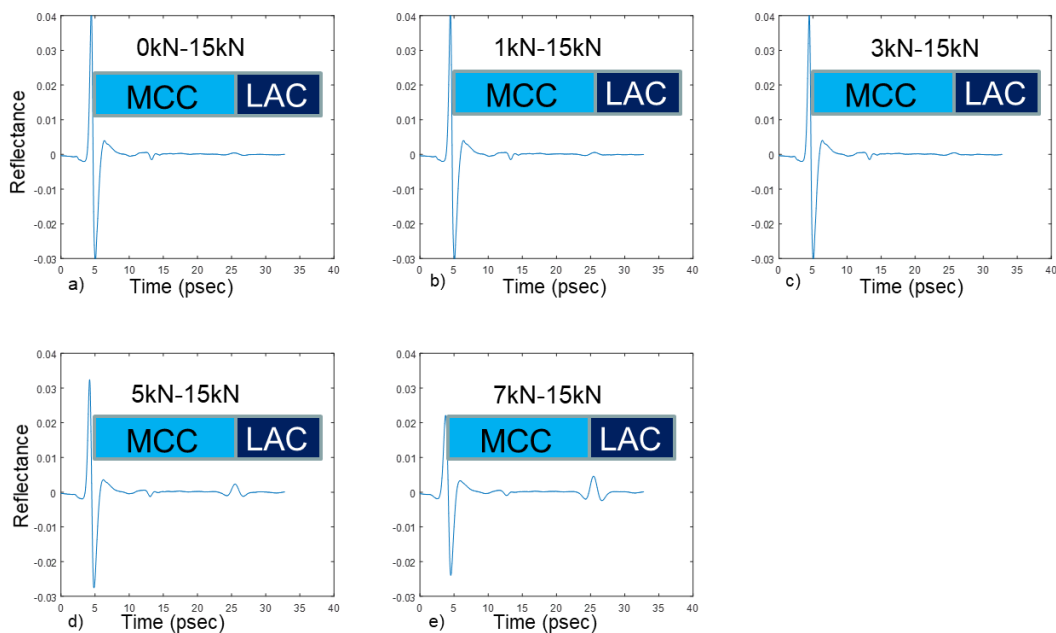
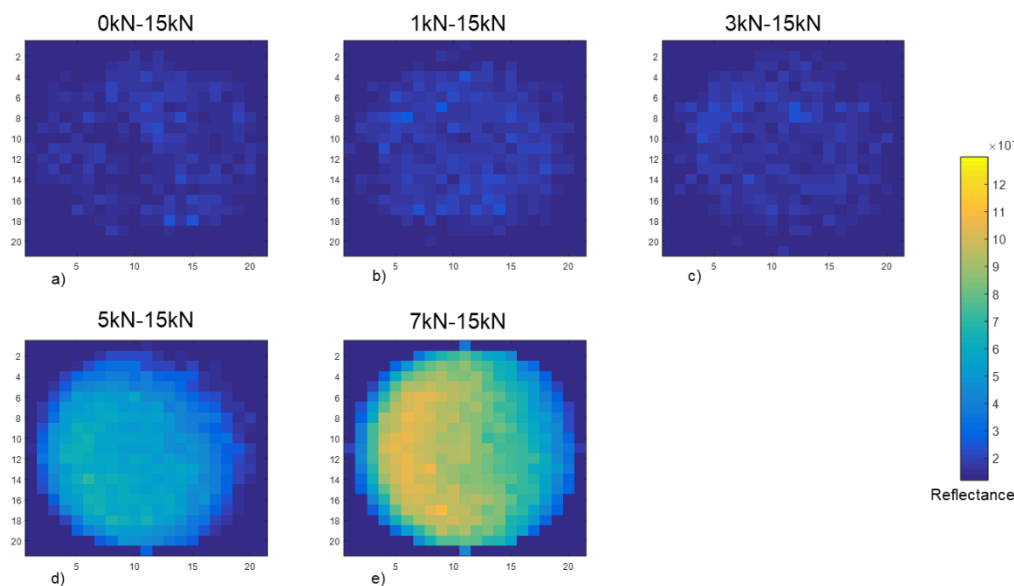


Figure 5.47: Mean time domain signal of MCC-Lac bilayer tablets with tamping force of 0 (a), 1 (b), 3 (c), 5 (d), and 7 (e) kN and MCC side of the tablet facing the terahertz source and detector.



*Figure 5.48: Layer interface reflection intensity maps of MCC-Lac bilayer tablets with tamping force of 0 (a), 1 (b), 3 (c), 5 (d), and 7 (e) kN and MCC side of the tablet facing the terahertz source and detector.*

The effect of the tablet position on layer interface intensity was also assessed. The MCC-Lac tablets were originally measured with the MCC side facing the detector and source. Scans of the same tablet were, also, made with the lactose side facing the detector and source. The mean time domain signals of these reversed tablets are seen in Figure 5.49. The locations of the reflections are similar to the originally measured MCC-Lac tablets. However, the time domain signal seems to include more noise. This is because the terahertz pulse is interacting more with the lactose layer. Lactose monohydrate is a strong absorber of the terahertz pulse, thus, causing dispersion effect in the signal. The shape of the reflected pulse at the layer interface is also different. This may be attributed to the magnitude and direction of the refractive index changes between the layers. However, the increasing intensity trend and intensity map distribution (Figure 5.50) is still similar to the originally scanned tablets.

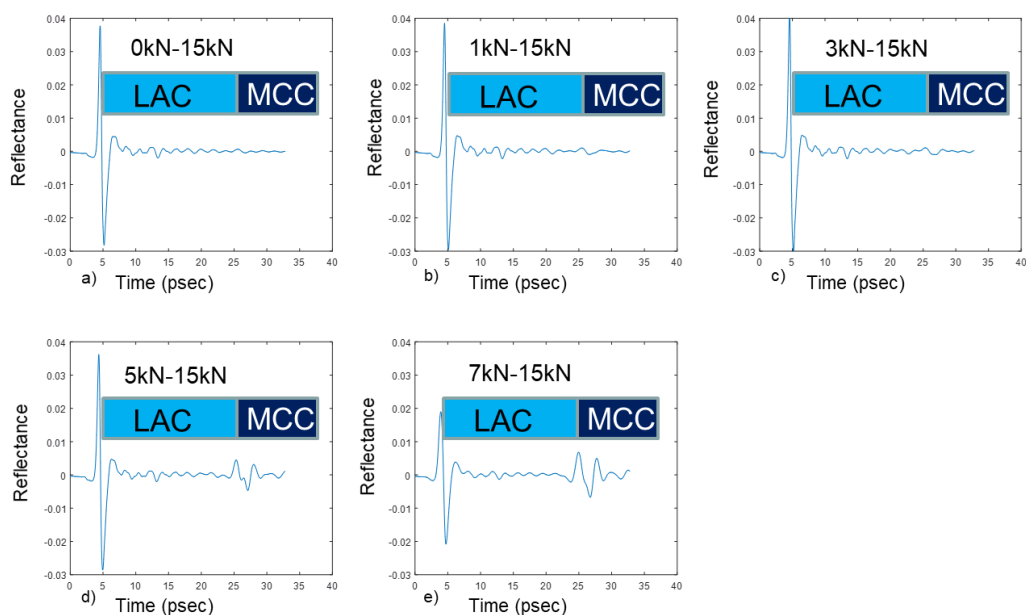


Figure 5.49: Mean time domain signal of MCC-Lac bilayer tablets with tamping force of 0 (a), 1 (b), 3 (c), 5 (d), and 7 (e) kN and lactose monohydrate side of the tablet facing the terahertz source and detector.

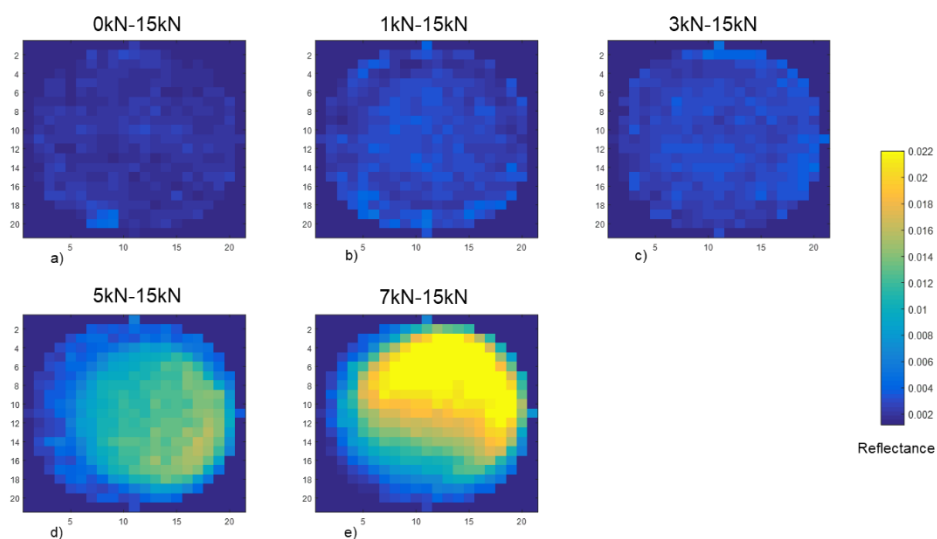


Figure 5.50: Layer interface reflection intensity maps of MCC-Lac bilayer tablets with tamping force of 0 (a), 1 (b), 3 (c), 5 (d), and 7 (e) kN and MCC side of the tablet facing the terahertz source and detector.

Time domain signals were also generated for a second set of bilayer tablets. These tablets had MCC in both the layers, therefore, only one side was scanned. Again 5 levels of tamping force were used to create interfacial strength variation. There is a weak reflection signal from the layer interface at approximately 25 psec (Figure 5.51), which slightly increases over tamping force. This is indicative of a refractive index change between voids and layer differences. The material in both the layers is the same, however, their densities maybe different, causing a small refractive index change. The interface intensity maps (Figure 5.52) shows that these small refractive changes due to voids and layer difference mainly occur at the 5 and 7 kN tamping forces. Specifically, the interface intensity is higher at the edges for these two tablets suggesting a weaker interfacial strength at these locations. The die wall friction during tableting and ejection is more prominent at the tablet edges, thus, potentially lowering the interfacial strength at the edge. The overall interface intensity for all the MCC-MCC tablets is significantly lower than the MCC-Lac tablets. This suggests the cohesion strength of MCC is much stronger than the adhesion strength between MCC and lactose layer. Therefore, the intermolecular interactions between the layers also contribute to the interfacial strength.

The source of the interface reflections was further investigated through simulation. It was observed that the shape of the reflected pulses was different. For example, in Figure 5.46c all the three primary reflections from the tablet surfaces and the layer interface have a unique shape. In addition, the shape of the interface reflections amongst the two sets of bilayer tablet are also different. The MCC-Lac bilayers with the lactose facing the source and detector, especially, has a unique reflection shape (Figure 5.49). Preliminary shape assessment was done to further improve signal interpretability.

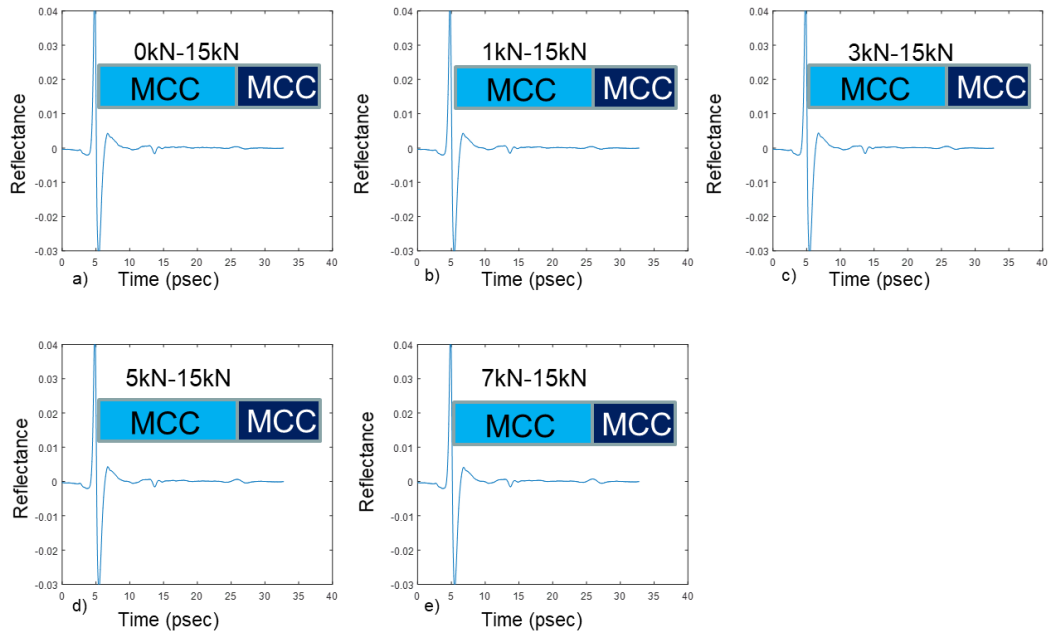


Figure 5.51: Mean time domain signal of MCC-MCC bilayer tablets with tamping force of 0 (a), 1 (b), 3 (c), 5 (d), and 7 (e) kN.

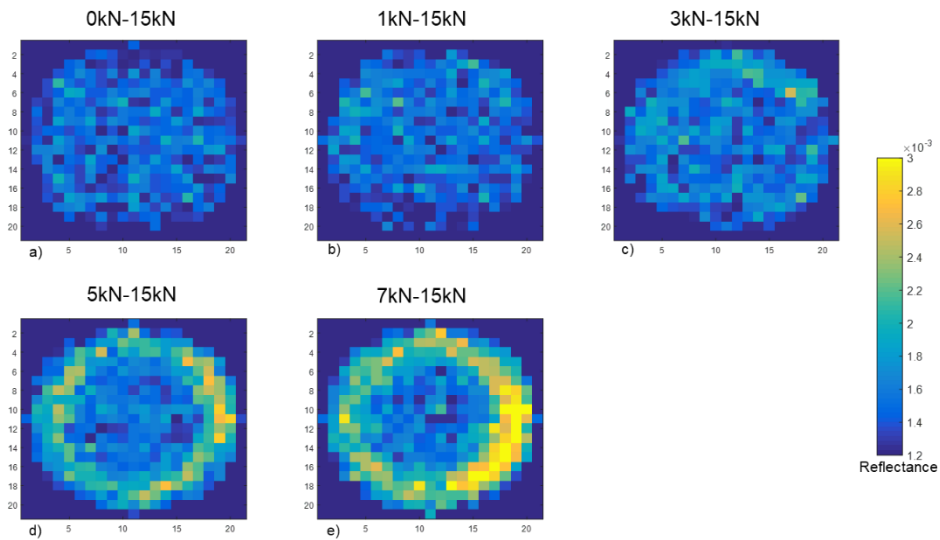
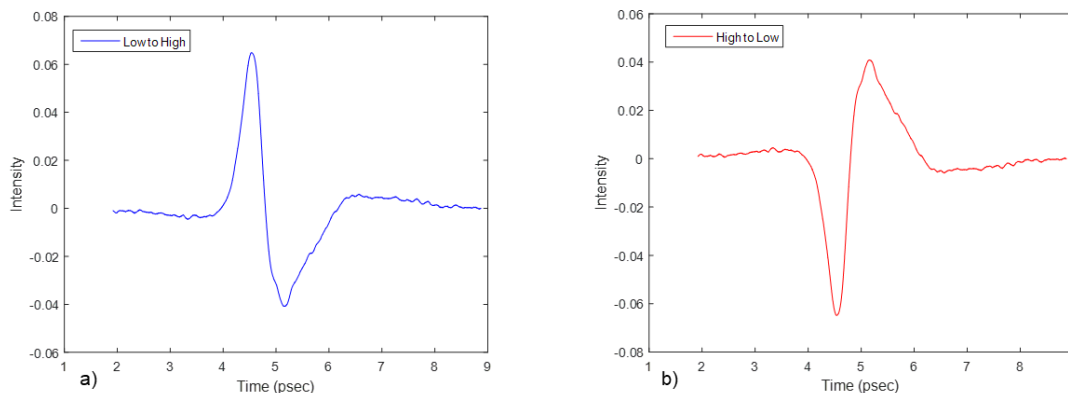


Figure 5.52: Layer interface reflection intensity maps of MCC-MCC bilayer tablets with tamping force of 0 (a), 1 (b), 3 (c), 5 (d), and 7 (e) kN.

The shape of the reflected pulses is dependent on the direction of change in the refractive index. Two primary types of pulse reflections are possible. The first type of pulse reflection occurs when the initial medium has a lower refractive index than the newly encountered medium. Alternatively, the change of refractive index from high to low corresponds to the second type of reflection. Figure 5.53a and 5.53b shows the corresponding shapes of the first and second type of pulse reflections, respectively. These two shapes are also observed in the monolithic and bilayer tablet time domain signals in Figures 5.45 and 5.46. The reflection due to the initial tablet surface corresponds to the first type of pulse reflection because the terahertz pulse travels through a low refractive index medium (air) before interacting with a high refractive index medium (tablet surface). The opposite effect occurs at the opposite side of the tablet results in the second type of pulse reflection. The interface reflection shapes, however, do not completely align with the shapes from these two types of pulse reflections. Instead, the shape is a combination of these two shapes due to the complex nature of the interface. Combinations of the two primary pulse reflections shapes were simulated to improve the interpretation of the interface reflection. The order of these combination provides potential understanding of the various medium present at the layer interface.



*Figure 5.53: Terahertz pulse reflection shape of refractive change in media from low to high (a) and high to low (b).*

The terahertz pulse transitions through air voids and/or a new solid layer (layer 2) at the layer interface, resulting in unique reflection shapes. For MCC-MCC bilayer tablets, layer 1 and layer 2 are the same component, therefore, the pulse transition through air voids potentially contributes more toward the reflection shape. Thus, primary reflections occur when the terahertz pulse encounters a refractive index change from high (layer 1 MCC) to low (voids), followed by a change from low (voids) to high (layer 2 MCC). Figure 5.54a shows these two reflections superimposed onto each other with an intentional time delay to account for pulse transition time between the media. The addition of these two shapes is shown in Figure 5.54b. This shape closely resembles the actual MCC-MCC bilayer tablets interface reflection shape, thus, suggesting the presence of minor voids at the interface, especially at higher tamping force. This is also potentially true for MCC-Lac bilayer tablets.

The MCC-Lactose tablets, however, have differing interface reflection shapes compared to the MCC-MCC bilayer tablets. This observation may occur due to the different components in each layer. The refractive index for lactose monohydrate is higher at most terahertz frequencies than MCC according to the transmission terahertz measurements of pure component tablets (Figure 5.55). Therefore, refractive index changes from layer to layer and layer to void both inherently contribute to the interface reflection shape. The tablet position, however, also effects the reflection shape. According to Figures 5.47 and 5.49, the same set of tablets produced different reflection shapes at the interface based on the specific layer facing the terahertz source and detector. The magnitude of the refractive index change is the same regardless of the two positions; however, the direction of the refractive index change is different. In the case where the MCC layer is facing the terahertz source and detector, the terahertz pulse encounters an increase

in refractive index traveling from the MCC layer to the lactose layer with negligible void space in between. The refractive index changes in the opposite direction when the lactose layer faces the terahertz source and detector. The direct layer to layer reflection event is simulated for the MCC facing side in Figure 5.54c and for the lactose facing side in Figure 5.54e. The same reflection event from the MCC-MCC bilayer tablet is also possible in the presence of voids at the interface. Thus, the simulated combination of these two reflection events (Figure 5.54c and 5.54e) results in an overall reflection shape seen in Figure 54d and 54f for the MCC facing and lactose facing tablet sides, respectively. These simulated overall reflection shapes resemble the observed interface reflection shapes. Therefore, these simulations potentially identified all the major reflection events at the interface.

The relationship between the interface reflection intensity and interfacial strength was further investigated by performing axial tensile strength measurements on the bilayer tablets. The procedure for these measurements involved applying a load in the axial direction until total mechanical failure was achieved. Two key information provided from this procedure was the interface surface profile after failure and the breaking force. Microscope images were made on the bottom half of the broken tablets to investigate the interface surface profile. The images of the MCC-Lac and MCC-MCC bilayer tablets are shown in Figures 5.56 and 5.57. Only 4 images are shown for MCC-MCC bilayer tablets because the 0 kN tamping force did not fail at the interface due to its high mechanical strength. In general, the surface roughness was seen to decrease with increasing tamping force. The increase in tamping force reduces mechanical interlocking, thus, creating smoother interfaces. The smoother surface also creates stronger interface reflections.

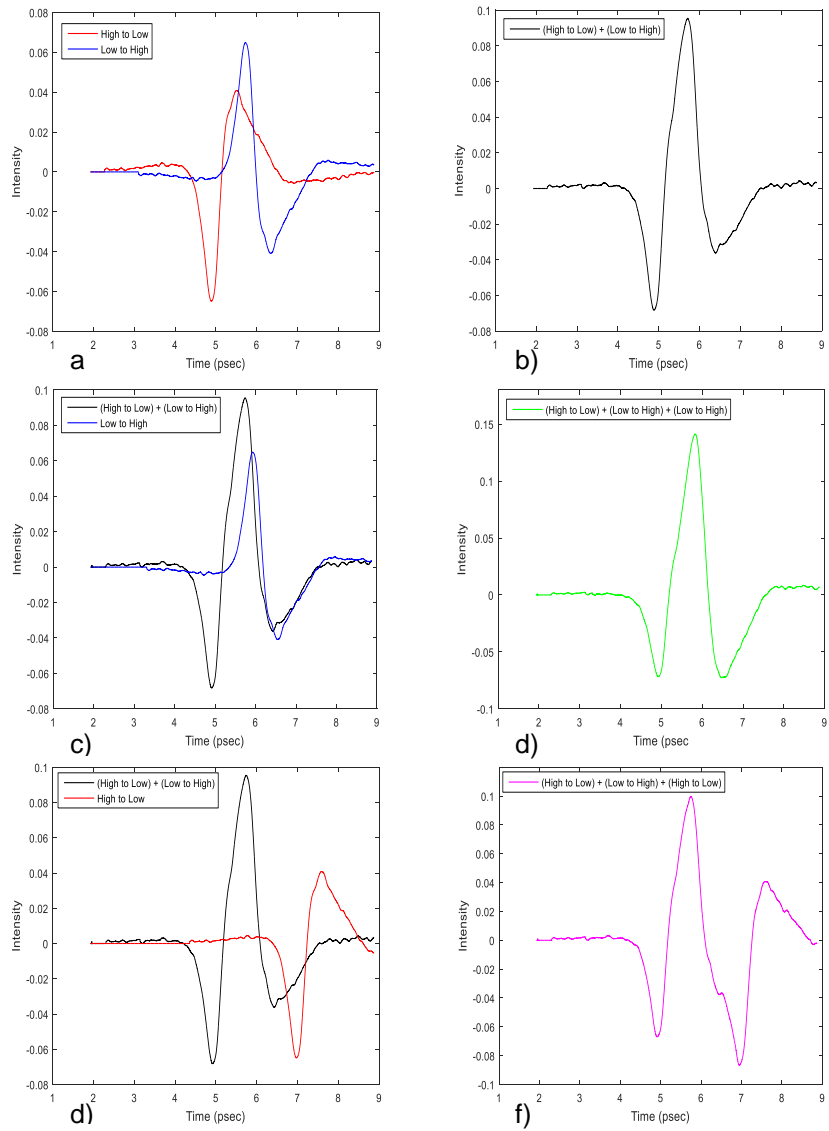


Figure 5.54: Simulated individual reflection shapes (a, c, d) and the overall combined reflection shapes (b, d, f) at the interface for MCC-MCC, MCC facing MCC-Lac, and lactose facing MCC-Lac bilayer tablets, respectively.

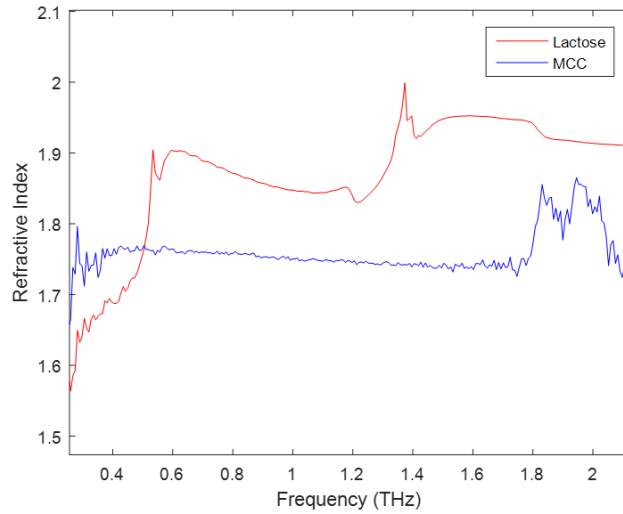


Figure 5.55: Refractive index spectra of pure lactose monohydrate and MCC tablets.

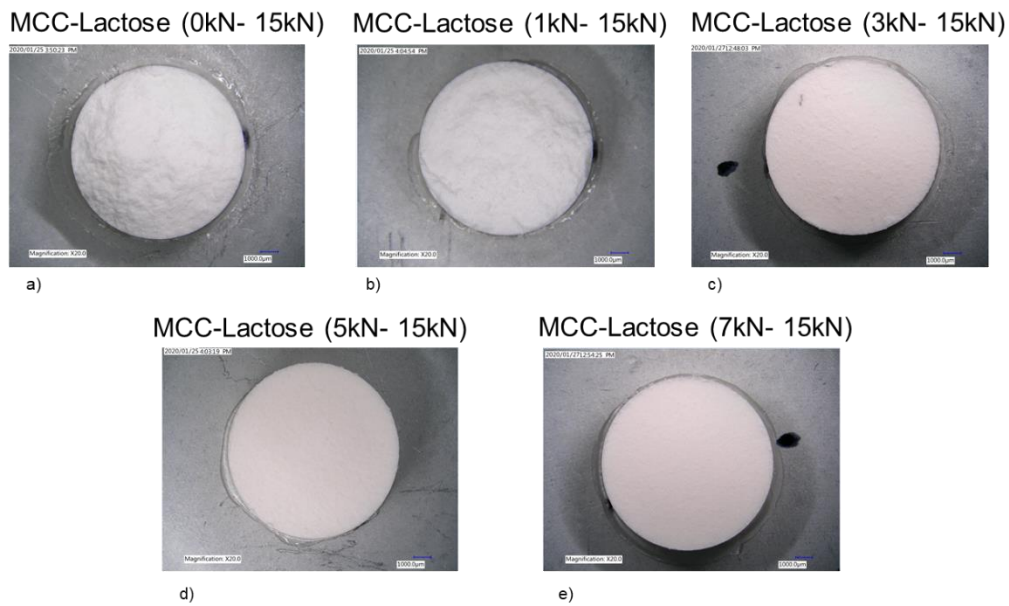
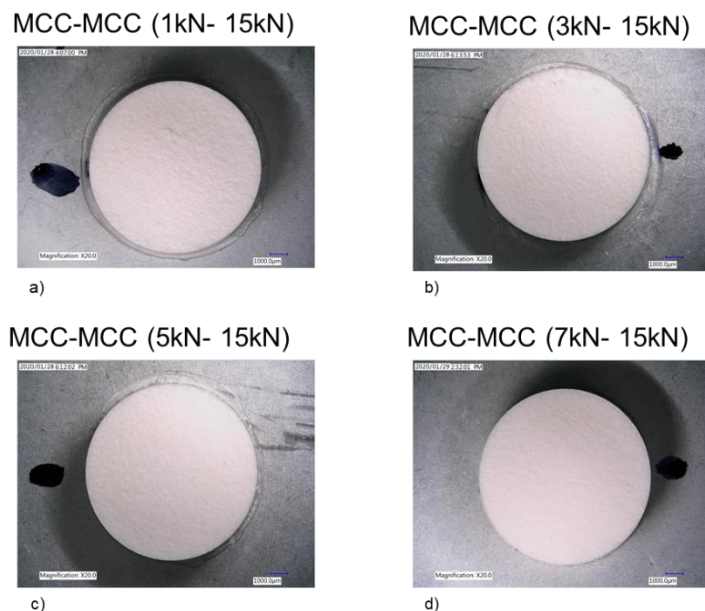


Figure 5.56: Surface images of the bottom half of the MCC-Lac bilayer tablets with tamping force of 0 (a), 1 (b), 3 (c), 5 (d), and 7 (e) kN tamping force after the tensile strength test



*Figure 5.57: Surface images of the bottom half of the MCC-Lac bilayer tablets with tamping force of 1 (a), 3 (b), 5 (c), and 7 (d) kN tamping force after the tensile strength test*

In addition to interface surface profile, the breaking force was also assessed. Figure 5.14 shows the breaking force at each tamping force. In general, the breaking force decreases with tamping force. The breaking force decreases significantly after the 1 kN tamping force for the MCC-Lac bilayer tablets. These results are supported by the microscope images as the surface roughness also significantly smoothens after 1 kN tamping force. A slightly different trend is observed for MCC-MCC bilayer tablets in which the breaking force reduces 3 kN tamping forces. It is important to note that overall the breaking force for all the MCC-MCC bilayer tablets is significantly higher than the MCC-Lac bilayer tablets. Thus, MCC-MCC bilayer tablets has relatively stronger interface interactions. The breaking force was converted to tensile strength and compared with the mean interface reflection intensity (reflectance). According to Figure 5.54, indirect nonlinear trend between these parameters. Additional tablets are required to establish the trend. However, these preliminary results show that a bilayer tablet with a weak

interfacial strength corresponds to a high intensity of the terahertz interface reflection. Thus, thresholds can be set on these reflection intensities to ensure the interfacial strength is within the desired criteria.

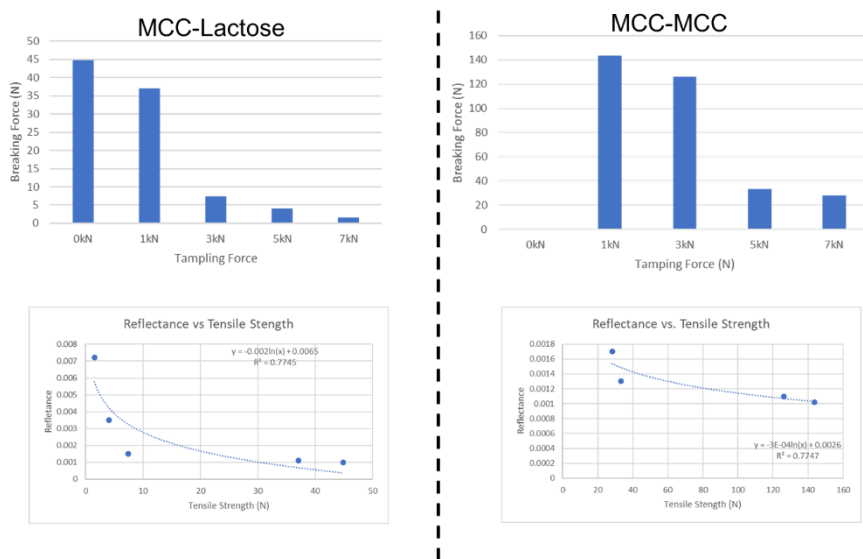


Figure 5.58: Breaking force versus tamping force and reflectance versus tensile strength for both MCC-Lac and MCC-MCC bilayer tablets.

#### 5.4. Summary and Conclusion

A bilayer tablet is an important form drug delivery offering several advantages such as improved drug efficacy and patient compliance. However, a critical challenge exists during manufacturing of these dosage forms. The mechanical strength tends to be low due to poor interfacial strength. Therefore, rapid and non-destructive tools to assess the interfacial strength and integrity are desired to improve process understanding and ensure that the product quality meets the required specifications. This study further investigated THz-TOF in reflectance model as a potential PAT tool for interfacial strength assessment of bilayer tablets.

Two sets of bilayer tablets were primarily analyzed with THz-TOF. The tablet composition was MCC in layer 1 and lactose monohydrate in layer 2 for the first set and MCC in both layers for the second set. Five tablets were produced in each set varying in tamping force to create

interfacial strength variation. Terahertz and axial tensile strength measurements were performed on these tablets to characterize the interfacial integrity.

The time domain signal from THz-TOF was able to provide information regarding the layer interface. Reflections from the interface due to refractive index changes was present in time domain signal and indicated the interfacial integrity. A stronger interface reflection potentially results from voids and/or smoother interfaces. Thus, interface reflection intensity maps were generated to provide locations of weak interfacial strength. Axial tensile strength measurements were also performed and further indicated that interface reflection intensity is related to tensile strength. Therefore, this work further demonstrated the strong potential of THz-TOF for bilayer tablet manufacturing across different formulations.

## Chapter 6: Conclusion

Mechanical strength is a critical quality attribute for compaction based unit operations. Therefore, PAT tools for mechanical strength assessment facilitate in improving process understanding and final product quality. This study investigated the relationship between refractive index measurement from THz-TOF and mechanical strength assessment. Mechanical strength is a function of porosity, mechanical interlocking, interparticle bonds, and solid bridges.<sup>158</sup> Refractive index was hypothesized to be highly correlated with mechanical strength. This hypothesis was based on the strong correlation between refractive index and porosity. As a result, 4 studies were performed. The first study confirmed the refractive index and porosity relation, while the remaining studies developed the relationship between refractive index and 3 different mechanical strength measurements.

The first study focused on development of porosity models. Porosity of pharmaceutical compacts is also often considered a critical quality attribute of both a roller compaction and a tablet compression processes due to its impact on tablet disintegration and dissolution. Terahertz spectroscopy provides an opportunity to monitor porosity rapidly and non-destructively, therefore, acting as a process analytical technology (PAT) tool for both roller compaction and tablet compression processes. This study provided further support for terahertz spectroscopy as a PAT tool by performing steps towards method validation. Specifically, the terahertz based porosity models were evaluated for accuracy and robustness by using unique test sets. These test sets included process parameter and chemical composition variations expected in a roller compaction or a tablet compression process. In total, four terahertz based porosity models were generated; three univariate models based on time domain refractive index and one multivariate

partial least squares (PLS) model based on frequency domain refractive index. All the models were shown to be robust against the process parameter and chemical composition variations used in this study. These models are able to be applied in real-time to improve process understanding and product quality.

After confirmation of the porosity relationship, the refractive index was then related to radial tensile strength (RTS). Tensile strength is a measure of the mechanical strength. This method operates by applying a load in the tensile direction until complete mechanical failure. Therefore, further testing is precluded due to its destructive nature. Terahertz time of flight spectroscopy was used as a nondestructive indicator of RTS for the tablets generated in chapter 2. Specifically, effective refractive index was modeled with RTS. However, the initial trend was observed to be nonlinear. In addition, the correlation between effective refractive index and RTS was low. This was attributed to chemical composition. In particular, the variation in MCC was acting as strong interferent, when trying to model effective refractive index for RTS. The interparticle bonds between MCC particles is very strong due to hydrogen bonding and predominant plastic deformation characteristics, thus causing a higher RTS. Therefore, it was concluded that separate models need to be generated for each chemical composition for accurate predictions.

Indentation hardness was the next mechanical assessment studies. Indentation hardness tests are employed for pharmaceutical tablets to determine intra tablet variation in density and mechanical strength. These tests involve penetrating the same with an indenter at different locations within a tablet thus assessing the resistance to deformation locally. The destructive nature of this technique and the extensive time required to perform these measurements eliminates its

applicability as a routine method or a process analytical technology (PAT) tool. This study investigated terahertz time of flight (THz-TOF) imaging as a PAT tool for intra tablet mechanical strength assessment. Specifically, THz-TOF was used due to its ability to extract refractive index from solid samples. Therefore, a model was generated between refractive index images and indentation hardness measurements. This successful model was shown to be able to convert refractive index images of a tablet into a hardness image. Further, the model was preliminarily tested on lubricated and non lubricated tableting systems. The lubricated tablet system showed a more uniform hardness distribution, thus reducing the propensity of tablet defects

The final mechanical strength assessment used was axial tensile strength for bilayer tablets. The multilayer tablet is an advanced solid oral dosage form that has gained considerable interest as an option for delivering fixed dose combination (FDC). In multilayer FDC tablets, two or more drugs are incorporated into a single dosage form thus reducing the dosing burden for patients. However, producing multilayer tablets with sufficient mechanical strength is often challenging. Inadequate manufacturing and material selection may result in the occurrence of a fracture at the layer interface causing tablet defects (*i.e.*, delamination). Delamination and other tablet defects that cause tablet breakage is a very critical concern as patients may not receive one of the intended drugs. Therefore, it is important to characterize the mechanical strength of multilayer tablets to mitigate these risks. Tensile strength and adhesion strength measurement methods are available and have been used to determine mechanical strength in bilayer tablets. These measurement methods are, however, destructive and do not fully comply with the Food and Drug Administration's (FDA) promoted process analytical technology (PAT) initiative. This study

demonstrated the strong potential of terahertz time of flight spectroscopy as a nondestructive PAT tool for characterizing the interfacial strength of bilayer tablets.

The work in this thesis was able to improve the understanding between refractive index, porosity, and mechanical strength. Refractive index was shown to be correlated with porosity, indentation hardness, radial tensile strength, and axial tensile strength. Therefore, THz-TOF provides the advantage of offering a rapid and non-destructive option for measuring porosity and mechanical strength of pharmaceutical compacts. Particularly for tableting and roller compaction processes, THz-TOF can be developed as PAT tool for inter and intra tablet/ribbon assessment of mechanical strength.

## **Appendix: Terahertz Time of Flight Spectroscopy as a Coating Thickness Reference Method for Partial Least Squares Near Infrared Spectroscopy Models**

### **Abstract**

Near infrared spectroscopy (NIRS) is often used during tablet coating process to assess coating thickness. As the coating process proceeds the increase and decrease in NIRS signal from both the coating formulation and tablet core has been related to coating thickness. Partial least square models are often generated relating NIRS spectra to reference coating thickness measurements for in-line and/or at-line monitoring of the coating process. This study investigates the effect of the reference coating thickness measurements on the accuracy of the model. The two primary reference techniques used were weight gain based coating thickness and terahertz based coating thickness. Most NIRS coating thickness models currently use weight gain based reference values, however, terahertz time of flight spectroscopy (THz-TOF) offers a more direct reference coating thickness measurement. Results showed that the accuracy of the NIRS coating thickness model significantly improved when terahertz based coating thickness measurements were used as reference when compared to weight gain based coating thickness measurements. Therefore, the application of THz-TOF as a reference method is further demonstrated.

## A.1. Introduction

Tablet coating is an important unit operation in the manufacturing of solid oral dosage forms. Reasons for coating include product identification, improving the chemical stability, taste masking, and the control of the dissolution behavior.<sup>208</sup> Coating thickness and uniformity are often considered critical quality attributes for the coating process. For enteric and sustained-release coating, the polymer thickness determines the location of the drug release and drug release kinetics respectively.<sup>208</sup> Also for drugs sensitive to light, humidity, and oxygen, the coating thickness dictates the chemical stability of the final product.<sup>208</sup> With FDA's initiative towards quality by design (QbD), it is important to monitor and control critical quality attributes (CQA) of the coating process with process analytical technology (PAT) to improve the final product quality.<sup>125</sup>

Near-Infrared spectroscopy (NIRS) is commonly used as a PAT tool for multiple unit operations in solid oral dosage manufacturing including tablet coating.<sup>209-219</sup> Most solid pharmaceutical components absorb light in the NIRS region (approximately 700 to 2500 nm), allowing for quantitative NIRS model development. For tablet coating, NIRS reflectance measurements are generally sensitive to the active pharmaceutical ingredient (API) in the tablet core along with the polymer from the film coating layer. Therefore, the disappearance of the tablet core information along with the appearance of coating film information in the NIRS absorbance spectra with increasing coating amount has been related to coating thickness and tablet weight gain.<sup>213, 215-2227-</sup>

However, challenges exist when utilizing NIRS for tablet coating. This spectroscopic technique is indirect, therefore, requiring a chemometric calibration model which relates reference coating thickness measurements with NIRS spectra. A common reference measurement used is tablet weight gain which acts as a surrogate for coating thickness. Tablet weight gain measurements are obtained by sampling tablets from the coating pan at different time points. The average weight of the sampled coated tablets is then subtracted from the average core tablet weight to obtain weight gain. However, measurement errors occur due to variations in core tablet weight, attrition during the process, and moisture variation.<sup>223</sup> In addition, tablets with the same weight gain may have different coating thickness distribution, thus, acting as a source of error during calibration model development.

The limitations of weight gain measurements are resolved by considering direct thickness measurements of individual coated tablets. Direct thickness measurements include obtaining microscope images of sliced tablets. In these images the tablet core and film layer are generally distinguishable allowing for coating thickness measurements.<sup>224</sup> X-ray microtomography has also been used to measure coating thickness of individual tablets.<sup>225</sup> However, these techniques are time consuming and/or destructive, therefore limiting any further tablet testing.

A potential rapid, non-destructive, and non-invasive option for direct coating thickness measurement is terahertz time of flight spectroscopy (THz-TOF).<sup>214, 226-235</sup> The low frequency vibration (approximately 300 GHz–3 THz or 10-100  $\text{cm}^{-1}$ ) of terahertz spectroscopy induces crystalline phonon vibrations, intermolecular bond vibrations (hydrogen bonding), and torsion vibrations in pharmaceutical samples. In addition to absorption, the long wavelength of terahertz radiation undergoes specular reflections at interfaces corresponding to refractive index changes.

For coated tablets, there is a clear interface between the film coating and tablet core. The reflected terahertz pulse associated with this interface is identified in the time domain waveform and the time delay of this reflected pulse is used to calculate the coating thickness. The lower limit of coating thickness from this technique has been reported to be approximately 30-40  $\mu\text{m}$ .<sup>228, 229</sup>

An accurate and direct coating thickness measurement such as THz-TOF is especially important for functional coating assessment. Applications for measuring coating thickness with THz-TOF for control of dissolution rate<sup>236-241</sup> and photostability<sup>242</sup> are demonstrated in literature. An example of dissolution rate control is a study by Muller et al<sup>240</sup>. Results from this study showed that the coating thickness of a sustained released coating layer had a high correlation with the mean dissolution time (MDT). According to their linearly fitted model, an increase in coating thickness of 1  $\mu\text{m}$  resulted in an approximate MDT increase of 3 minutes.<sup>240</sup> Similarly, for photostability control, a recent study done by this lab showed that coating thickness measurements from THz-TOF was significant for predicting the photodegradation of coated nifedipine tablets especially at higher illumination conditions.<sup>242</sup> Under an illumination condition of 300,000 lux hours, an approximate coating thickness change from 30 to 35  $\mu\text{m}$ s resulted in an approximate increase of four percent label claim of nifedipine. Therefore, a coating thickness measurement method with a high accuracy is desired to achieve a precise dissolution rate and photodegradation control to ensure that final the product is within the required quality specifications.

The THz-TOF technique provides direct and accurate coating thickness measurement, however, this technique is still limited for real-time applications. In-line THz-TOF measurements have been recently demonstrated<sup>228, 229, 231, 243</sup> but are still not widely available compared to NIRS. Therefore, THz-TOF can complement NIRS by being applied as a reference method during calibration model development. Previous studies have demonstrated using THz-TOF to calibrate a NIRS quantitative model for coating thickness.<sup>214, 244</sup> However, the assessment of the prediction performance with THz-TOF as the reference has currently not been reported.

This study compares the method performance of NIRS models developed using traditional weight gain or THz-TOF as a reference method. Specifically, three at-line NIRS coating thickness models were developed in which each model utilized a different reference method: two weight gain based coating thickness measurements and one terahertz based coating thickness measurement. The prediction performance between the three models was evaluated. Further discussion of the relative advantages of thickness measurements of individual tablets compared to population comparison (weight gain) is presented for NIRS quantitative model development. Thus, this work further establishes the application of THz-TOF as a core reference technique for tablet coating thickness.

## **A.2. Materials and Methods**

### **A.2.1. Core Tablet**

Film coating was applied on placebo tablets. The formulation of these tablets was 69.5 wt% lactose monohydrate (Foremost Farms, WI, USA), 30 wt% microcrystalline cellulose (FMC BioPolymer, DE, USA ), and 0.5 wt% magnesium stearate (Fisher Scientific, PA, USA).

Manufacturing procedure involved first blending the components in a V-Blender with batch size of 4 kg for 15 minutes. Then, the blend was tableted using a 38-station rotary tablet press (HT-AP-38, Elizabeth-Hata International, Inc. PA, USA) tooled with two sets of flat faced beveled edged 9.5 mm punches (3/16 inches) with a score on the upper punch. Flat faced punches were used to reduce spectroscopic measurement errors due to tablet curvature. The fill depth and punch distance on the press were adjusted to maintain tablet weight and crushing force of approximately 450 mg and 9000 ponds.

### **A.2.2. Coating Solution**

The coating composition consisted of 4 wt% hypromellose (HPMC; Pharmacoat 606, Shin-Etsu Chemical Co., Ltd.), 2.4 wt% titanium dioxide (TiO<sub>2</sub>; USP, Spectrum chemical), 0.8 wt% Talc (powder USP, Spectrum chemical) and 0.8 wt% polyethylene glycol 6000 (PEG 6000; Alfa Aesar). Talc and TiO<sub>2</sub> were dispersed while HPMC and PEG 6000 were dissolved in 92 wt% water.

### **A.2.3. Tablet Coating Process**

Coating was performed in a HCT-48 pan coater (Freund Co., Ltd.). The pre-heating and spraying phase of coating were performed in the pan coater. Drying and cooling of samples, removed during the process, was performed outside the pan coater by placing them in a humidity chamber with conditions of 35% RH and room temperature. The parameters set for the pre-heating phase were 80°C target inlet air temperature and 10 RPM pan speed. For the spraying phase, the spray rate was maintained at 17 g/min and the rotation speed was adjusted to 15 RPM.

#### A.2.4. Terahertz Based Coating Thickness

The first coating thickness reference method used was terahertz based coating thickness. Terahertz images of coated tablets were acquired by using TAS7500IM (Advantest, California, USA). The spatial resolution of the images was set to 0.5 mm. At each pixel, 128 time domain waveforms were collected in reflection mode and averaged to produce final pixel waveform. A flat metal mirror was used to acquire a reference waveform. A reflected pulse present in the waveform indicates the incident pulse encountering a change in refractive index. The first reflected pulse is due to the refractive index change between air and solid surface of coated tablet or metal mirror. The second reflected pulse in a coated tablet sample is expected to be from the incident pulse encountering the interface between tablet core and film coating layer. Assuming the incident angle is perpendicular to the tablet surface, the time delay ( $\Delta t$ ) between the second pulse (core surface) and first pulse (coated tablet surface) is directly related to the coating thickness ( $d$ ) by Equation 64. In this Equation, 'c' is the speed of light and 'n' is the refractive index of the film coating layer. The refractive index of the film was measured separately by casting a thin film with an appropriately characterized thickness to be approximately 2.06 by the terahertz instrument in transmission setup. Time delay was calculated by first shifting the waveforms allowing the first pulse maximum of sample and reference to correspond to 0 picosecond time point. Then, all waveforms were normalized to the first peak maximum value of the reference waveform. Subtraction of the normalized sample and reference waveforms was performed, and the time point at the minima of the resulting vector was determined to be the time delay.

$$d = \frac{c\Delta t}{2n} \quad (64)$$

At the edge of the tablet, the reflection of the terahertz pulse is expected to be influenced by the curvature, so the thickness data was extracted from a 5.5 mm square at the center of the tablet. The average coating thickness from the approximate 121 pixels of this area were used as the final coating thickness value.

#### **A.2.5. Weight Gain Based Coating Thickness**

The second and third coating thickness reference method used was a weight gain based coating thickness measurement. Weight gain was calculated by first obtaining average weight of 100 sampled uncoated tablets. A total of 50 tablets were sampled at each designated coating time point. The average weight of these sampled tablets ( $m_s$ ) was subtracted by the average uncoated tablet weight ( $m_c$ ) to obtain weight gain/film amount ( $m$ ) for each coating time point. Film amounts with 5, 10, 50, and 100 sampled tablets were also determined resulting in a relative error of an NIR coating thickness model to be 15.5, 12.1, 9.2, 9.2 % respectively. Since there was not a significant change in the film amount and model performance between 50 and 100 sampled tablets, only results from 50 tablets are reported in this study.

The film amount was converted into coating thickness ( $d$ ) by Equation 65, resulting in the second coating thickness reference method. This conversion requires both film density ( $\rho$ ) and core tablet surface area ( $A$ ). For film density assessment, a thin film was created by spraying the coating solution into a petri dish and then drying the film. The dried film was removed and then cut into a 25 mm x 25 mm square. The weight and average thickness value from 16 micrometer measurements of the film was 142.5 mg and 0.1765 mm respectively. The film density, calculated from the weight and average thickness of the film, was approximately 1.25 mg/mm<sup>3</sup>.

The core tablet surface area was estimated to be 288.51 mm<sup>2</sup>; this was based on the average diameter (9.59 mm) and thickness (4.78 mm) of 50 uncoated tablets.

$$d = \frac{\frac{m}{A}}{\rho} \quad (65)$$

These tablet weight measurements were made on undried sampled tablets from the coating process. Therefore, loss-on-drying (LOD) measurements (Computrac Max 2000, Arizona Instruments) were obtained to account for additional weight gain and/or core tablet moisture variation during processing due to environmental moisture conditions. Five tablets at specified coating times were sampled for LOD measurements. These tablets were crushed with a mortar and pestle and then heated to 140°C in the LOD apparatus. The resulting moisture percent (LOD) from this procedure was then used in Equation 66 and Equation 67 to obtain moisture corrected sample tablet weight ( $m_{s'}$ ) and core tablet weight ( $m_{c'}$ ). The coated tablet solid weight (Solid Weight<sub>Sample</sub>) was then subtracted from the averaged core tablet solid weight (Solid Weight<sub>Core</sub>) to yield moisture corrected weight gain or film amount ( $m_{mc}$ ) shown in Equation 68. The third reference method used was the coating thickness measurements obtained from applying the moisture corrected film amount into Equation 63.

$$m_{s'} = m_s - \left(m_s * \frac{LOD}{100}\right) \quad (66)$$

$$m_{c'} = m_c - \left(m_c * \frac{LOD}{100}\right) \quad (67)$$

$$m_{mc} = m_{s'} - m_{c'} \quad (68)$$

### **A.2.6. Near Infrared Spectral Collection**

Near infrared reflectance spectra of coated tablets were collected on a Foss NIRSystem 5000 bench top instrument (Silver Spring, Maryland). The wavelength range was approximately 400 to 2500 nm with spectral resolution of 2 nm. The number of co-adds was set to 32. The tablets were centered using an iris prior to spectral collection. One spectrum, corresponding to the same face of the tablet scanned by THz-TOF, was collected. Near infrared spectra were truncated and preprocessed with standard normal variate (SNV) and mean-centering to reduce physical sample effects and enhance chemical features attributed to the film coating layer and core tablet. Three partial least squares (PLS) models for predicting coating thickness were generated relating the NIRS absorbance information to either a weight gain based coating thickness measurement or a terahertz based coating thickness measurement. All NIRS data processing and modeling was performed using MATLAB software (Version R2016b, Mathworks Inc., MA, USA) and PLS\_Toolbox (Version 821, Eigen-vector Research Inc., WA, USA).

### **A.2.7. Experimental Design**

A design of experiment with spraying time as factor was used to achieve variation in inter-tablet coating thickness. Approximately 60 coated tablets were sampled at 80, 100, 120, 140, and 160 minutes coating times. Fifty tablets were used to obtain weight gain measurements at each sampling time point while terahertz measurements and NIRS spectral collections were performed on the same remaining 10 sampled tablets. An additional sample of five tablets were removed at coating times of 100, 120, and 140 minutes and used as test set to assess NIRS coating thickness model performance. All measurements were performed immediately after sampling without any additional drying.

### **A.3. Results and Discussion**

This study involved comparing three NIRS coating thickness models differing in reference method. One model used coating thickness measurements from THz-TOF as the reference method. Figure A.59 shows images outputted by the terahertz instrument of one tablet sampled at specific coating times according to the experimental design. Only one face of the tablet was scanned by THz-TOF. This face also coincided with the face scanned by NIRS. Each pixel in the images shown in Figure 1 are color coded based on the coating thickness. As the coating time increases the coating thickness of the tablet increases. The intra-tablet coating thickness relative standard deviation ranged from 4.95 to 8.35 % from all 50 tablets collected from the five sampling points and scanned with THz-TOF . The terahertz based coating thickness for a single tablet was determined to be the average coating thickness from 121 pixels corresponding to the respective tablet. The inter-tablet terahertz based coating thickness standard deviation from 10 tablets across each sampling point ranged from 8.35 to 11.23 % . Potential reasons for inter-tablet coating thickness variation at specified time points include variation in core tablet dimensions and low drying capacity. The observed range of terahertz based coating thickness from the sampling points varied between approximately 30 to 50  $\mu\text{m}$ .

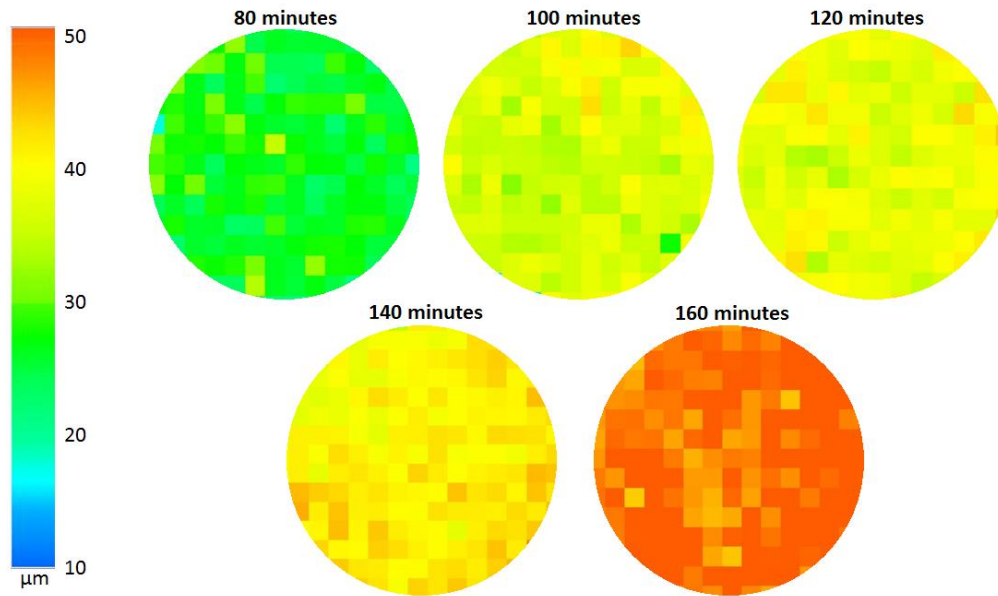


*Figure A.59: Coating thickness images of one tablet at each sampled coating time point measured by terahertz*

Two additional models used weight gain based coating thickness values as reference method for NIRS coating thickness models. The weight of 50 tablets were obtained at each sampling point for these calculations to account for core tablet weight variation and to achieve enough amount of material to operate the LOD apparatus. In contrast to terahertz based coating thickness measurements, weight gain based coating thickness measurements considered the entire tablet instead of one face. For the generation of one weight gain based thickness value, an average of 50 tablets were required at each sampling point to account for core tablet weight variation. Weight gain coating thickness measurements, both with and without moisture correction, were generated. The moisture content of the core tablet before and during the spraying phase of the coating process is expected to be different due to the variation in the environmental condition inside the coating pan. Therefore, moisture correction was performed to normalize this environmental effect. Figure A.60 shows comparison between weight gain based coating

thickness with and without moisture correction at each sampling point. There is an approximate decrease of 10 microns in coating thickness at each sampling point after the application of moisture correction.

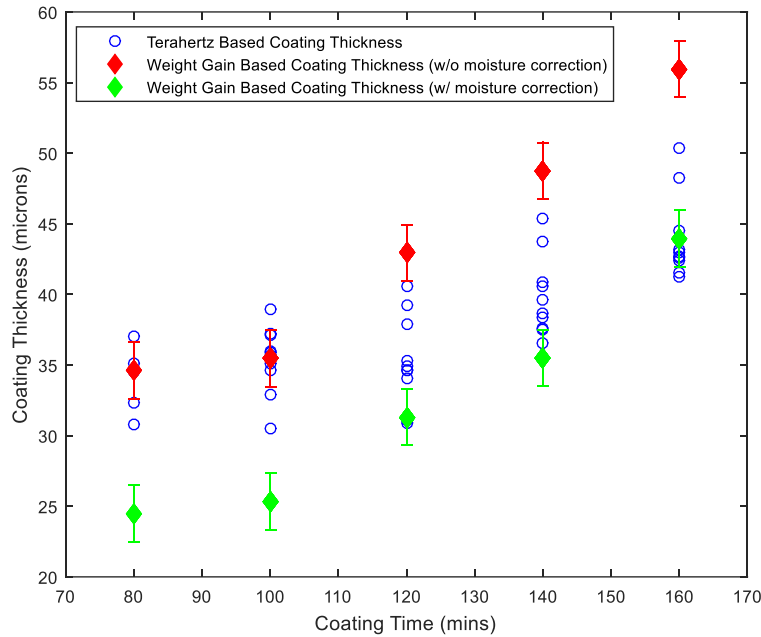


Figure A.60: Weight gain based coating thickness and terahertz based coating thickness trend with coating time. Error bars represent lab uncertainty.

In addition to the two (with and without moisture correction) weight gain based coating thickness measurements, terahertz based coating thickness measurements of 10 tablets are plotted as a function of coating time in Figure A.60. Differences exist between weight gain based coating thicknesses and terahertz based coating thicknesses. A potential reason for the specific difference between terahertz based coating thickness and weight gain based coating thickness is due to sampling. For weight gain based coating thickness measurements the entire tablet was considered, and more tablets were sampled (50 vs.10). Therefore, weight-gain based coating thickness measurement was potentially more representative of the batch. However, the reliance on averaging large numbers of samples to mitigate core tablet weight variation decreases the

accuracy of the coating thickness measurement for a single tablet. Direct coating thickness measurements such as shown in this study with THz-TOF, is not dependent on core tablet weight variations.

Another potential reason for the differences between the coating thickness measurements is due to the effect of moisture. The weight gain based coating thickness measurements with moisture correction fall approximately within the range of the terahertz based coating thickness measurements at the later coating time points (120, 140, and 160 minutes). However, at the earlier coating time points (80 and 100 minutes), the weight gain based coating thickness measurements without moisture correction are more closely associated with the terahertz based coating thickness measurements than weight gain based coating thickness measurements with moisture correction. This is potentially owing to the higher moisture gain of the core tablet at earlier time points during processing and transportation compared to the later coating time points. A higher coating thickness potentially provides better protection of the core tablet from moisture. Figure A.60 also shows that generally the weight gain based coating thickness with moisture correction fall below or are in the lower half of the terahertz based coating thickness distribution at each coating time point. A potential reason is that the terahertz based coating thickness measurements potentially overestimates the actual coating thickness of the final coating tablet due to swelling of the film coating layer from moisture. Thus, allowing the coated tablets to complete the drying stage may resolve this issue. However, for real-time applications it is more practical to define the immediate state (undried) of the coating tablet to better understand the process.

The effect of the weight gain based (with and without moisture correction) and terahertz based coating thickness reference methods on NIRS coating thickness models for this pan coating system was evaluated. The three reference coating thickness measurements was related to NIRS spectrum of each sampled coated tablet. The raw NIR spectra is seen in Figure A.61a. All the NIRS spectra were preprocessed with standard normal variate (SNV) to minimize scatter and enhance chemical signature. The SNV processed spectra is illustrated in Figure A.61b. These spectra are color coded in terms of coating time. There are both increasing and decreasing  $\log(1/R)$  trends in the spectra with respect to coating time. At the approximate wavelength range of 1400 to 1600 nm there is a decrease in NIRS signal. This is attributed to the decrease in core tablet NIRS signal as the coating thickness increases. This was confirmed by comparing NIRS preprocessed spectra with the pure NIRS spectrum of the components in the core tablet. One of the primary component in the core tablet is lactose monohydrate which has NIR peaks in the wavelength range of 1400 to 1600 nm (Figure A.61b) due to water and OH band. In contrast, there are NIRS regions exhibiting increasing  $\log(1/R)$  trends in the NIRS spectra such as at the signal near 2250 nm. This is potentially due to the NIRS signal from the coating formulation. The primary component in the coating formulation is HPMC which also has an NIRS peak at approximately 2250 nm due to CH combinations. All NIRS models were developed with truncated NIRS spectra included wavelength range of 1375 to 2325 nm to enhance model specificity towards both the tablet core and coating formulation.

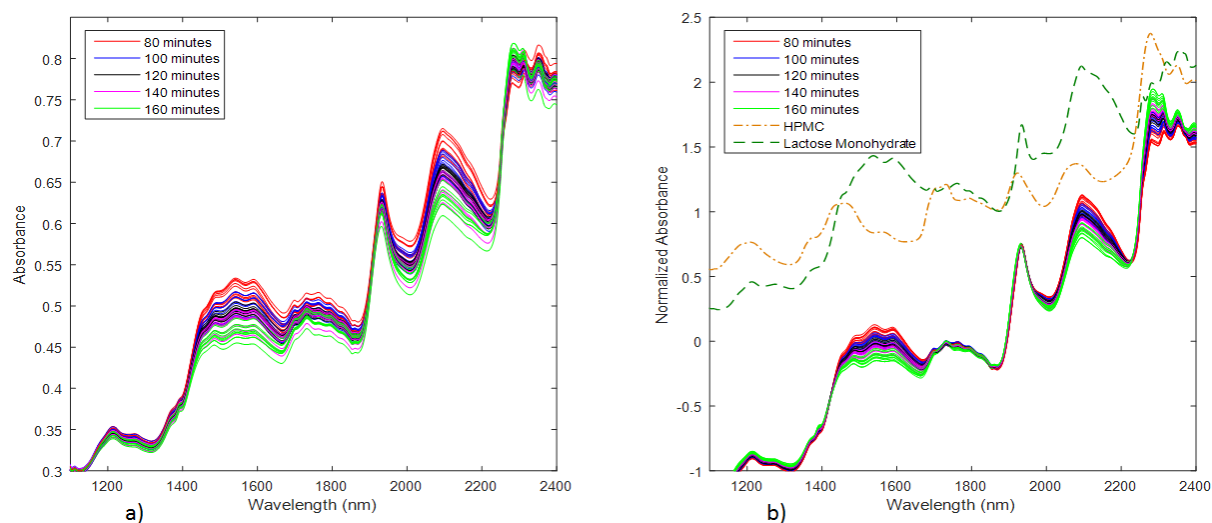


*Figure A.61: Raw NIR spectra (a) and SNV processed NIR spectra (b) compared with offset pure HPMC and lactose monohydrate NIR spectrum*

Three PLS models were built relating truncated and SNV processed NIRS spectra with either weight gain based coating thickness without moisture correction, weight gain based coating thickness with moisture correction, or terahertz based coating thickness. For the three models, ten NIRS spectra were collected at each sampling point. The NIRS coating thickness model using weight gain based coating thickness measurements as reference related one averaged coating thickness measurement to each of the ten NIRS spectra for a sampling time point. In contrast, the NIRS coating thickness model using THz-TOF related one coating thickness measurement to one NIRS spectrum. All final models used three latent variables according to the minimization of the prediction error minimization for an independent test set. The resulting percent spectral variance captured by all the models was approximately 99.50%. Figure 4 shows only the first two latent variables for the terahertz based coating thickness model as both the weight gain based model latent variable shapes and the percent variance captured were similar.

The NIRS regions with high spectral covariance corresponds to NIR peaks present in lactose monohydrate and HPMC (Figure A.62) further verifying the selection of the wavelengths. The model results are seen in Figure A.63. The terahertz based model has a significantly lower prediction error than both the weight gain based models (1.49 versus 4.74 and 4.97  $\mu\text{m}$ ).

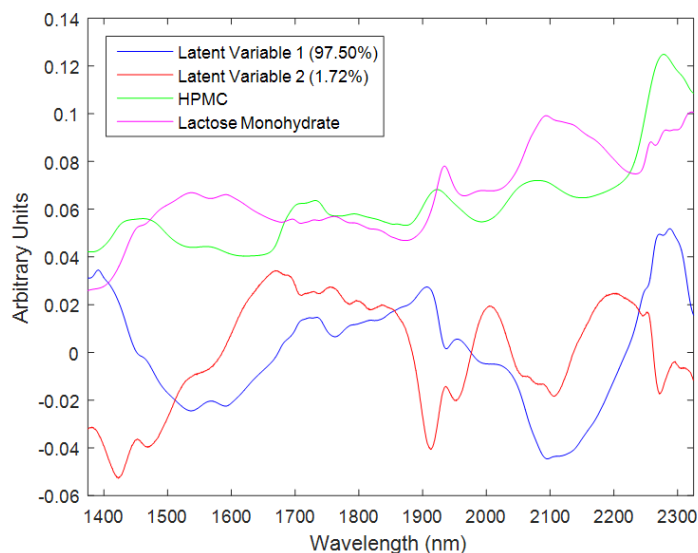


*Figure A.62: First two latent variables for the terahertz based coating thickness model compared with offset pure HPMC and lactose monohydrate NIR spectrum*

The difference in model performance is primarily due to the reference method. The weight gain based coating models used reference method which is based on averaging multiple tablets, therefore, individual tablet coating thickness variation information is not included. This is seen in Figure A.63a. At each measured coating thickness value, there is a wide distribution of predictions as the model is forcing one value to represent multiple tablets which is not appropriate in this case. In Figure A.63b, the improvement in model performance is seen when individual coating thickness measurements on each tablet was made for reference purpose. In addition, the accuracy of the measurement also effects the model performance. Weight gain

based coating thickness measurements include error from moisture and core tablet weight variation in contrast with terahertz based coating thickness measurements. The different tablet coating thickness range in Figure A.63 was potentially attributed to the measurement accuracy.

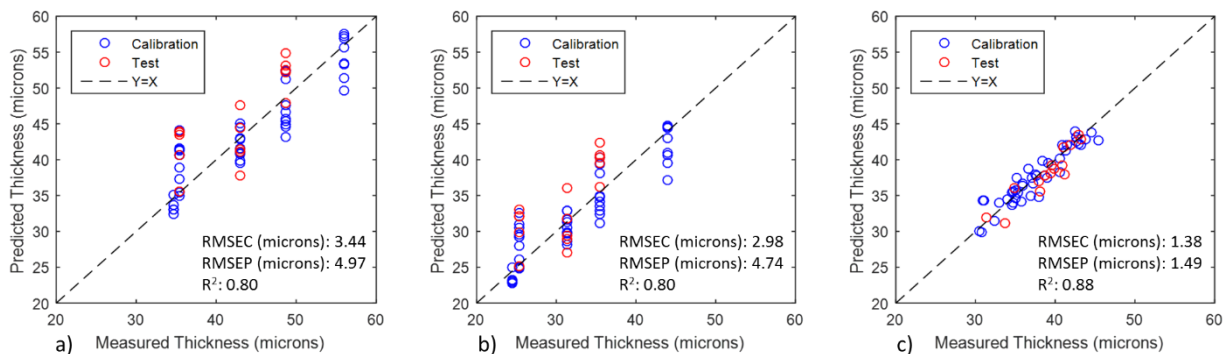


*Figure A.63: Weight gain based coating thickness model without moisture correction (a), weight gain based coating thickness with moisture correction (b), and terahertz based coating thickness (c) models*

The accuracy of the model was improved by averaging spectral and reference measurements. Averaging is also potentially important for in-line models where the NIRS spectrometer is placed inside the pan coater. One NIRS measurement may include NIRS signature from multiple tablets. In addition, it is difficult to know exactly what tablets were scanned. Therefore, averaging spectral and reference measurements from representative samples facilitates in estimating the information obtaining for the NIRS spectrometer at the sampled time. With the dataset in this study, NIRS spectra and reference values were averaged to create three additional models: averaged weight gain based model with and without moisture correction and averaged terahertz based model. Figure A.64 shows the three averaged models. Only one latent variable was used to develop both these models which accounted for approximately 99.78% spectral variance. Averaging improved the model performance of all the models. However, terahertz based coating model still had lower prediction error compared to the two weight gain based

coating thickness models (0.75 versus 3.89 and 3.65  $\mu\text{m}$ ). All these NIR coating thickness models has potential to be used at-line and/or in-line to improve product quality and efficiency.

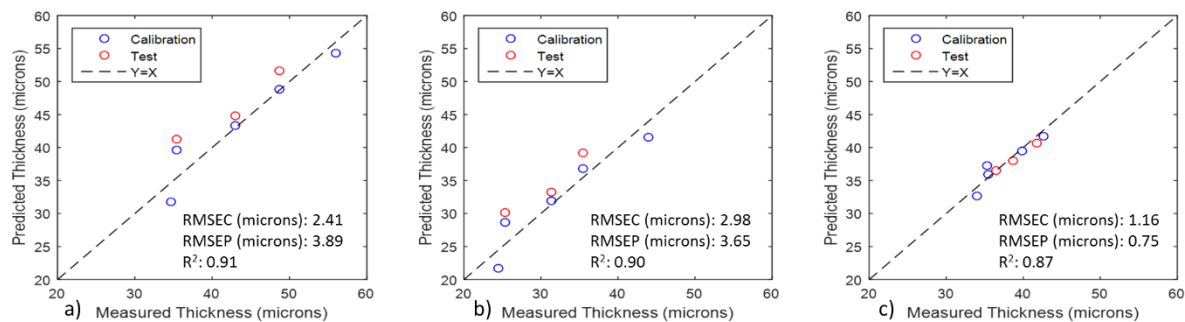


Figure A.64: Averaged weight gain based coating thickness model without moisture correction (a), weight gain based coating thickness with moisture correction (b), and terahertz based coating thickness (b) models

#### A.4. Summary and Conclusion

Coating thickness is a critical quality attribute for most pan coating processes. In order to improve coating process understanding and product quality, PAT tools such as NIRS are used to obtain real time measurements. This study investigated the effect of the reference methods on NIRS coating thickness models.

The two types of reference methods compared were coating thickness based on weight gain and direct terahertz based coating thickness. Three PLS models were generated relating NIRS spectra to with and without moisture corrected weight gain based coating thickness and terahertz based coating thickness. Results showed that when using terahertz based coating thickness measurements as a reference, the model accuracy was significantly higher compared to model based on weight gain based coating measurements as a reference. Averaging spectra and THz-TOF reference measurements (tablet weight gain inherently averages the weight of 50 tablets)

improved model performance. Even though all the models improved in accuracy after averaging, the terahertz based coating thickness model still showed better prediction performance compared to weight gain based coating thickness model.

The model accuracy for an NIR coating thickness model is important for coating applications associated with dissolution and stability control. The type of reference method used was shown to influence the model accuracy. While weight gain is a popular technique used for reference measurement for coating thickness, it is not as direct as THz-TOF. Further, weight gain does not afford the opportunity to associate the specific weight of an individual tablet with the spectrum of that tablet. THz-TOF allows the 1:1 association of an NIRS spectrum with a coating thickness measurement for a single tablet. However, errors associated with weight gain decreases the accuracy of the measurement. Thus, the use of a direct reference techniques, in this case THz-TOF, improves accuracy of an NIRS coating thickness model.

## Reference

1. Bi, Y.; Sunada, H.; Yonezawa, Y.; Danjo, K., Evaluation of rapidly disintegrating tablets prepared by a direct compression method. *Drug development and industrial pharmacy* **1999**, *25* (5), 571-581.
2. Markl, D.; Sauerwein, J.; Goodwin, D. J.; van den Ban, S.; Zeitler, J. A., Non-destructive determination of disintegration time and dissolution in immediate release tablets by terahertz transmission measurements. *Pharmaceutical research* **2017**, *34* (5), 1012-1022.
3. Ferrero, C.; Bravo, I.; Jiménez-Castellanos, M., Drug release kinetics and fronts movement studies from methyl methacrylate (MMA) copolymer matrix tablets: effect of copolymer type and matrix porosity. *Journal of controlled release* **2003**, *92* (1-2), 69-82.
4. Otsuka, M.; Tanabe, H.; Osaki, K.; Otsuka, K.; Ozaki, Y., Chemoinformetrical evaluation of dissolution property of indomethacin tablets by near-infrared spectroscopy. *Journal of pharmaceutical sciences* **2007**, *96* (4), 788-801.
5. Pilpel, N.; Otuyemi, S.; Kurup, T., Factors affecting the disintegration and dissolution of chloroquine phosphate/starch tablets. *Journal of Pharmacy and Pharmacology* **1978**, *30* (1), 214-219.
6. Batsanov, S. S.; Ruchkin, E. D.; Poroshina, I. A., *Refractive Indices of Solids*. Springer: 2016.
7. Baxter, J. B.; Guglietta, G. W., Terahertz spectroscopy. *Analytical chemistry* **2011**, *83* (12), 4342-4368.
8. Mantsch, H. H.; Naumann, D., Terahertz spectroscopy: The renaissance of far infrared spectroscopy. *Journal of Molecular Structure* **2010**, *964* (1-3), 1-4.
9. Taday, P. F.; Newnham, D. A., Technological advances in terahertz pulsed systems bring far infrared spectroscopy into the spotlight. *Spectroscopy Europe* **2004**, *16* (5), 20-25.
10. Allen Jr, L. V., Quality-control analytical methods: Refractometry. *International journal of pharmaceutical compounding* **2003**, *7* (5), 383.
11. Green, M. D.; Nettey, H.; Rojas, O. V.; Pamanivong, C.; Khounsaknalath, L.; Ortiz, M. G.; Newton, P. N.; Fernández, F. M.; Vongsack, L.; Manolin, O., Use of refractometry and colorimetry as field methods to rapidly assess antimalarial drug quality. *Journal of pharmaceutical and biomedical analysis* **2007**, *43* (1), 105-110.
12. Kendrick, B. S.; Kerwin, B. A.; Chang, B. S.; Philo, J. S., Online size-exclusion high-performance liquid chromatography light scattering and differential refractometry methods to determine degree of polymer conjugation to proteins and protein–protein or protein–ligand association states. *Analytical biochemistry* **2001**, *299* (2), 136-146.
13. Kumar, R.; Agarwal, A.; Shubhankar, B., Counterfeit Drug Detection: Recent Strategies and Analytical Perspectives. *Int J Pharma Res Health Sci* **2018**, *6* (2), 2351-58.
14. Silvennoinen, R.; Peiponen, K.-E.; RÄTY, J., Detection of Refractive Index Change of Liquids by Diffractive Element talrd Sensor. *Optical review* **1999**, *6* (1), 68-70.
15. Singh, H. K.; Chamuah, N.; Sarkar, D.; Bezboruah, T., Non-intrusive technique for measuring refractive index of clear and transparent liquids. *IEEE Sensors Journal* **2014**, *14* (2), 313-314.
16. Zillies, J. C.; Zwioerek, K.; Winter, G.; Coester, C., Method for quantifying the PEGylation of gelatin nanoparticle drug carrier systems using asymmetrical flow field-flow fractionation and refractive index detection. *Analytical chemistry* **2007**, *79* (12), 4574-4580.

17. Zölls, S.; Gregoritz, M.; Tantipolphan, R.; Wiggenhorn, M.; Winter, G.; Friess, W.; Hawe, A., How subvisible particles become invisible—Relevance of the refractive index for protein particle analysis. *Journal of pharmaceutical sciences* **2013**, *102* (5), 1434-1446.
18. WATANABE, A.; YAMAOKA, Y.; KURODA, K., Study of crystalline drugs by means of polarizing microscope. III. Key refractive indices of some crystalline drugs and their measurement using an improved immersion method. *Chemical and Pharmaceutical Bulletin* **1980**, *28* (2), 372-378.
19. Strachan, C. J.; Taday, P. F.; Newnham, D. A.; Gordon, K. C.; Zeitler, J. A.; Pepper, M.; Rades, T., Using terahertz pulsed spectroscopy to quantify pharmaceutical polymorphism and crystallinity. *Journal of Pharmaceutical Sciences* **2005**, *94* (4), 837-846.
20. Palermo, R.; Cogdill, R. P.; Short, S. M.; Drennen III, J. K.; Taday, P. F., Density mapping and chemical component calibration development of four-component compacts via terahertz pulsed imaging. *Journal of pharmaceutical and biomedical analysis* **2008**, *46* (1), 36-44.
21. Bawuah, P.; Mendia, A. P.; Silfsten, P.; Pääkkönen, P.; Ervasti, T.; Ketolainen, J.; Zeitler, J. A.; Peiponen, K.-E., Detection of porosity of pharmaceutical compacts by terahertz radiation transmission and light reflection measurement techniques. *International journal of pharmaceutics* **2014**, *465* (1-2), 70-76.
22. King, M. D.; Buchanan, W. D.; Korter, T. M., Identification and quantification of polymorphism in the pharmaceutical compound diclofenac acid by terahertz spectroscopy and solid-state density functional theory. *Analytical chemistry* **2011**, *83* (10), 3786-3792.
23. Peiponen, K.-E.; Silfsten, P.; Pajander, J.; Ketolainen, J., Broadening of a THz pulse as a measure of the porosity of pharmaceutical tablets. *International journal of pharmaceutics* **2013**, *447* (1-2), 7-11.
24. May, R. K.; Su, K.; Han, L.; Zhong, S.; Elliott, J. A.; Gladden, L. F.; Evans, M.; Shen, Y.; Zeitler, J. A., Hardness and density distributions of pharmaceutical tablets measured by terahertz pulsed imaging. *Journal of pharmaceutical sciences* **2013**, *102* (7), 2179-2186.
25. Niwa, M.; Hiraiishi, Y.; Iwasaki, N.; Terada, K., Quantitative analysis of the layer separation risk in bilayer tablets using terahertz pulsed imaging. *International journal of pharmaceutics* **2013**, *452* (1-2), 249-256.
26. Lens, A., *Optics, retinoscopy, and refractometry*. Slack Incorporated: 2005.
27. Antošová, M.; Polakovič, M.; Bálaš, V., Separation of fructooligosaccharides on a cation-exchange HPLC column in silver form with refractometric detection. *Biotechnology techniques* **1999**, *13* (12), 889-892.
28. Clement, A.; Yong, D.; Brechet, C., Simultaneous identification of sugars by HPLC using evaporative light scattering detection (ELSD) and refractive index detection (RI). Application to plant tissues. *Journal of Liquid Chromatography & Related Technologies* **1992**, *15* (5), 805-817.
29. Desbene, P.; Portet, F.; Goussot, G., Quantitative trace analysis of surfactant mixtures by reversed-phase high-performance liquid chromatography with refractometric detection. *Journal of Chromatography A* **1996**, *730* (1-2), 209-218.
30. Główska, F. K.; Łada, M. K.; Grund, G.; Wachowiak, J., Determination of treosulfan in plasma and urine by HPLC with refractometric detection; pharmacokinetic studies in children undergoing myeloablative treatment prior to haematopoietic stem cell transplantation. *Journal of Chromatography B* **2007**, *850* (1-2), 569-574.

31. Maas, F. M.; Hoffmann, I.; Van Harmelen, M. J.; De Kok, L. J., Refractometric determination of sulphate and other anions in plants separated by High-Performance Liquid Chromatography. *Plant and Soil* **1986**, *91* (1), 129-132.
32. Stoiber, R. E.; Morse, S. A., *Crystal identification with the polarizing microscope*. Springer Science & Business Media: 2012.
33. Wheatcroft, J. C., Terahertz Time Domain Spectroscopy and Fresnel Coefficient Based Predictive Model. **2012**.
34. Syms, R. R. A.; Cozens, J. R., *Optical Guided Waves and Devices*. McGraw-Hill: 1992.
35. Cauchy, L., Sur la dispersion de la lumiere. *bull. des. sc. maht.* **1830**, *14*, 9.
36. Ghosh, G., *Handbook of optical constants of solids: Handbook of thermo-optic coefficients of optical materials with applications*. Academic Press: 1998.
37. Briot, C., *Essais sur la théorie mathématique de la lumière*. Mallet-Bachelier, imp.-lib: 1864.
38. Hartmann, J., A simple interpolation formula for the prismatic spectrum. *The Astrophysical Journal* **1898**, *8*, 218.
39. Conrady, A. E., *Applied Optics and Optical Design, Part One*. Courier Corporation: 2013.
40. Tatian, B., Fitting refractive-index data with the Sellmeier dispersion formula. *Applied optics* **1984**, *23* (24), 4477-4485.
41. Tilton, L. W., *Prism refractometry and certain goniometrical requirements for precision*. 1929.
42. Bass, J. D.; Weidner, D. J., Method for measuring the refractive index of transparent solids. *Review of Scientific Instruments* **1984**, *55* (10), 1569-1573.
43. Bond, W., Measurement of the refractive indices of several crystals. *Journal of Applied Physics* **1965**, *36* (5), 1674-1677.
44. Chandra, B.; Bhaiya, S., A simple, accurate alternative to the minimum deviation method of determining the refractive index of liquids. *American Journal of Physics* **1983**, *51*, 160-161.
45. Synowicki, R.; Pribil, G. K.; Cooney, G.; Herzinger, C. M.; Green, S. E.; French, R. H.; Yang, M. K.; Burnett, J. H.; Kaplan, S., Fluid refractive index measurements using rough surface and prism minimum deviation techniques. *Journal of Vacuum Science & Technology B: Microelectronics and Nanometer Structures Processing, Measurement, and Phenomena* **2004**, *22* (6), 3450-3453.
46. Cheng, C.-C., Refractive index measurement by prism autocollimation. *American Journal of Physics* **2014**, *82*, 214-216.
47. Van Keuren, E. R., Refractive index measurement using total internal reflection. *American journal of physics* **2005**, *73* (7), 611-614.
48. Chiu, M.-H.; Lee, J.-Y.; Su, D.-C., Refractive-index measurement based on the effects of total internal reflection and the uses of heterodyne interferometry. *Applied optics* **1997**, *36* (13), 2936-2939.
49. Meeten, G., Refractive index errors in the critical-angle and the Brewster-angle methods applied to absorbing and heterogeneous materials. *Measurement Science and Technology* **1997**, *8* (7), 728.
50. Onodera, H.; Awai, I.; Ikenoue, J.-i., Refractive-index measurement of bulk materials: prism coupling method. *Applied optics* **1983**, *22* (8), 1194-1197.
51. Faust, R., An interferometric method of studying local variations in the refractive indices of a solid. *Proceedings of the Physical Society. Section B* **1952**, *65* (1), 48.

52. Fendley, J., Measurement of refractive index using a Michelson interferometer. *Physics Education* **1982**, 17 (5), 209.
53. Gillen, G. D.; Guha, S., Refractive-index measurements of zinc germanium diphosphide at 300 and 77 K by use of a modified Michelson interferometer. *Applied optics* **2004**, 43 (10), 2054-2058.
54. Bommareddi, R. R., Applications of optical interferometer techniques for precision measurements of changes in temperature, growth and refractive index of materials. *Technologies* **2014**, 2 (2), 54-75.
55. Tadmor, R.; Chen, N.; Israelachvili, J. N., Thickness and refractive index measurements using multiple beam interference fringes (FECO). *Journal of colloid and interface science* **2003**, 264 (2), 548-553.
56. Gillen, G. D.; Guha, S., Use of Michelson and Fabry–Perot interferometry for independent determination of the refractive index and physical thickness of wafers. *Applied optics* **2005**, 44 (3), 344-347.
57. Lunazzi, J.; Garavaglia, M., Fabry-Perot laser interferometry to measure refractive index or thickness of transparent materials. *Journal of Physics E: Scientific Instruments* **1973**, 6 (3), 237.
58. Brasunas, J. C.; Cushman, G. M., Interferometric but nonspectroscopic technique for measuring the thickness of a transparent plate. *Optical Engineering* **1995**, 34 (7), 2126-2131.
59. Coppola, G.; Ferraro, P.; Iodice, M.; De Nicola, S., Method for measuring the refractive index and the thickness of transparent plates with a lateral-shear, wavelength-scanning interferometer. *Applied optics* **2003**, 42 (19), 3882-3887.
60. Choi, H. J.; Lim, H. H.; Moon, H. S.; Eom, T. B.; Ju, J. J.; Cha, M., Measurement of refractive index and thickness of transparent plate by dual-wavelength interference. *Optics express* **2010**, 18 (9), 9429-9434.
61. Pristinski, D.; Kozlovskaya, V.; Sukhishvili, S. A., Determination of film thickness and refractive index in one measurement of phase-modulated ellipsometry. *JOSA A* **2006**, 23 (10), 2639-2644.
62. McCrackin, F. L.; Passaglia, E.; Stromberg, R. R.; Steinberg, H. L., Measurement of the thickness and refractive index of very thin films and the optical properties of surfaces by ellipsometry. *J. Res. Nat. Bur. Sec. A* **1963**, 67.
63. Fujiwara, H., *Spectroscopic ellipsometry: principles and applications*. John Wiley & Sons: 2007.
64. Tompkins, H.; Irene, E. A., *Handbook of ellipsometry*. William Andrew: 2005.
65. Synowicki, R., Spectroscopic ellipsometry characterization of indium tin oxide film microstructure and optical constants. *Thin Solid Films* **1998**, 313, 394-397.
66. Al-Ani, K. S., Methods of Determining the refractive Index of thin solid films. *International J. Appl. Phys.* **2008**, 4 (1), 17-23.
67. Al-Ani, S.; Hogarth, C., The optical properties of amorphous V2O5 and SiO thin films and of the mixed dielectric system SiO/V2O5. *Journal of materials science* **1985**, 20 (4), 1185-1192.
68. Löper, P.; Stuckelberger, M.; Niesen, B.; Werner, J.; Filipic, M.; Moon, S.-J.; Yum, J.-H.; Topič, M.; De Wolf, S.; Ballif, C., Complex refractive index spectra of CH3NH3PbI3 perovskite thin films determined by spectroscopic ellipsometry and spectrophotometry. *The journal of physical chemistry letters* **2014**, 6 (1), 66-71.

69. de Larivière, G. P.; Frigerio, J.; Rivory, J.; Abeles, F., Estimate of the degree of inhomogeneity of the refractive index of dielectric films from spectroscopic ellipsometry. *Applied optics* **1992**, *31* (28), 6056-6061.
70. Fenstermaker, C. A.; McCrackin, F. L., Errors arising from surface roughness in ellipsometric measurement of the refractive index of a surface. *Surface Science* **1969**, *16*, 85-96.
71. Han, P.; Tani, M.; Usami, M.; Kono, S.; Kersting, R.; Zhang, X.-C., A direct comparison between terahertz time-domain spectroscopy and far-infrared Fourier transform spectroscopy. *Journal of Applied Physics* **2001**, *89* (4), 2357-2359.
72. Yasuda, H.; Hosako, I., Measurement of terahertz refractive index of metal with terahertz time-domain spectroscopy. *Japanese Journal of Applied Physics* **2008**, *47* (3R), 1632.
73. Hangyo, M.; Nagashima, T.; Nashima, S., Spectroscopy by pulsed terahertz radiation. *Measurement Science and Technology* **2002**, *13* (11), 1727.
74. Shen, Y.-C., Terahertz pulsed spectroscopy and imaging for pharmaceutical applications: a review. *International journal of pharmaceutics* **2011**, *417* (1-2), 48-60.
75. Naftaly, M.; Miles, R., Terahertz time-domain spectroscopy: A new tool for the study of glasses in the far infrared. *Journal of non-crystalline solids* **2005**, *351* (40-42), 3341-3346.
76. Jepsen, P. U.; Fischer, B. M., Dynamic range in terahertz time-domain transmission and reflection spectroscopy. *Optics letters* **2005**, *30* (1), 29-31.
77. Němec, H.; Kadlec, F.; Kužel, P.; Duvillaret, L.; Coutaz, J.-L., Independent determination of the complex refractive index and wave impedance by time-domain terahertz spectroscopy. *Optics communications* **2006**, *260* (1), 175-183.
78. Lucarini, V.; Saarinen, J. J.; Peiponen, K.-E.; Vartiainen, E. M., *Kramers-Kronig relations in optical materials research*. Springer Science & Business Media: 2005; Vol. 110.
79. Schmuttenmaer, C. A., Exploring dynamics in the far-infrared with terahertz spectroscopy. *Chemical reviews* **2004**, *104* (4), 1759-1780.
80. Upadhyaya, P.; Nguyen, K.; Shen, Y.; Obradovic, J.; Fukushige, K.; Griffiths, R.; Gladden, L.; Davies, A.; Linfield, E., Characterization of Crystalline Phase-Transformations in Theophylline by Time-Domain Terahertz Spectroscopy. *Spectroscopy letters* **2006**, *39* (3), 215-224.
81. Taday, P. F.; Bradley, I.; Arnone, D.; Pepper, M., Using terahertz pulse spectroscopy to study the crystalline structure of a drug: A case study of the polymorphs of ranitidine hydrochloride. *Journal of pharmaceutical sciences* **2003**, *92* (4), 831-838.
82. Strachan, C. J.; Rades, T.; Newnham, D. A.; Gordon, K. C.; Pepper, M.; Taday, P. F., Using terahertz pulsed spectroscopy to study crystallinity of pharmaceutical materials. *Chemical Physics Letters* **2004**, *390* (1-3), 20-24.
83. Mori, T.; Igawa, H.; Okada, D.; Yamamoto, Y.; Iwamoto, K.; Toyota, N.; Kojima, S., Broadband terahertz time-domain spectroscopic study on form II polyvinylidene fluoride. *Journal of Molecular Structure* **2015**, *1090*, 93-97.
84. Kim, Y.; Yee, D.-S., High-speed terahertz time-domain spectroscopy based on electronically controlled optical sampling. *Optics letters* **2010**, *35* (22), 3715-3717.
85. Baxter, J. B.; Schmuttenmaer, C. A., Conductivity of ZnO nanowires, nanoparticles, and thin films using time-resolved terahertz spectroscopy. *The Journal of Physical Chemistry B* **2006**, *110* (50), 25229-25239.
86. Jiang, Z.; Li, M.; Zhang, X.-C., Dielectric constant measurement of thin films by differential time-domain spectroscopy. *Applied Physics Letters* **2000**, *76* (22), 3221-3223.

87. Ho, L.; Müller, R.; Römer, M.; Gordon, K.; Heinämäki, J.; Kleinebudde, P.; Pepper, M.; Rades, T.; Shen, Y.; Strachan, C., Analysis of sustained-release tablet film coats using terahertz pulsed imaging. *Journal of Controlled release* **2007**, *119* (3), 253-261.
88. Ervasti, T.; Silfsten, P.; Ketolainen, J.; Peiponen, K.-E., A study on the resolution of a terahertz spectrometer for the assessment of the porosity of pharmaceutical tablets. *Applied spectroscopy* **2012**, *66* (3), 319-323.
89. May, R. K.; Han, L.; Alton, J.; Zhong, S.; Elliott, J. A.; Byers, C.; Gladden, L. F.; Evans, M.; Shen, Y.; Zeitler, J. A. In *Pharmaceutical tablet hardness measurements with THz pulsed imaging*, Infrared, Millimeter, and Terahertz Waves, 2009. IRMMW-THz 2009. 34th International Conference on, IEEE: 2009; pp 1-2.
90. Withayachumnankul, W.; Fischer, B. M.; Lin, H.; Abbott, D., Uncertainty in terahertz time-domain spectroscopy measurement. *JOSA B* **2008**, *25* (6), 1059-1072.
91. Igne, B.; Hossain, M. N.; Drennen III, J. K.; Anderson, C. A., Robustness considerations and effects of moisture variations on near infrared method performance for solid dosage form assay. *Journal of Near Infrared Spectroscopy* **2014**, *22* (3), 179-188.
92. Hossain, M. N.; Igne, B.; Anderson, C. A.; Drennen III, J. K., Influence of moisture variation on the performance of Raman spectroscopy in quantitative pharmaceutical analyses. *Journal of pharmaceutical and biomedical analysis* **2019**, *164*, 528-535.
93. Chakkittakandy, R.; Corver, J. A.; Planken, P. C., Quasi-near field terahertz generation and detection. *Optics Express* **2008**, *16* (17), 12794-12805.
94. Nashima, S.; Morikawa, O.; Takata, K.; Hangyo, M., Measurement of optical properties of highly doped silicon by terahertz time domain reflection spectroscopy. *Applied physics letters* **2001**, *79* (24), 3923-3925.
95. Azimi-Sadjadi, M. R.; Charleston, S.; Wilbur, J.; Dobeck, G. J., A new time delay estimation in subbands for resolving multiple specular reflections. *IEEE transactions on signal processing* **1998**, *46* (12), 3398-3403.
96. Withayachumnankul, W.; Ferguson, B.; Rainsford, T.; Mickan, S.; Abbott, D., Direct fabry-pérot effect removal. *Fluctuation and Noise Letters* **2006**, *6* (02), L227-L239.
97. Hirsch, O.; Alexander, P.; Gladden, L. F., Techniques for cancellation of interfering multiple reflections in terahertz time-domain measurements. *Microelectronics Journal* **2008**, *39* (5), 841-848.
98. Duvillaret, L.; Garet, F.; Coutaz, J.-L., A reliable method for extraction of material parameters in terahertz time-domain spectroscopy. *IEEE Journal of selected topics in quantum electronics* **1996**, *2* (3), 739-746.
99. Cao, X.; Hancock, B. C.; Leyva, N.; Becker, J.; Yu, W.; Masterson, V. M., Estimating the refractive index of pharmaceutical solids using predictive methods. *International journal of pharmaceutics* **2009**, *368* (1-2), 16-23.
100. Korotkov, A.; Atuchin, V., Prediction of refractive index of inorganic compound by chemical formula. *Optics communications* **2008**, *281* (8), 2132-2138.
101. Eisenlohr, F., A new calculation of atomic refractions. *Z. physik. Chem* **1911**, *75*, 585-607.
102. Vogel, A. I., 369. Physical properties and chemical constitution. Part XXIII. Miscellaneous compounds. Investigation of the so-called co-ordinate or dative link in esters of oxy-acids and in nitro-paraffins by molecular refractivity determinations. atomic, structural, and group parachors and refractivities. *Journal of the Chemical Society (Resumed)* **1948**, 1833-1855.

103. Cao, X.; Leyva, N.; Anderson, S. R.; Hancock, B. C., Use of prediction methods to estimate true density of active pharmaceutical ingredients. *International journal of pharmaceutics* **2008**, *355* (1-2), 231-237.
104. Viana, M.; Jouannin, P.; Pontier, C.; Chulia, D., About pycnometric density measurements. *Talanta* **2002**, *57* (3), 583-593.
105. Sun, C. C., A novel method for deriving true density of pharmaceutical solids including hydrates and water-containing powders. *Journal of pharmaceutical sciences* **2004**, *93* (3), 646-653.
106. Vogel, A. I.; Cresswell, W. T.; Jeffery, G. H.; Leicester, J., 98. Physical properties and chemical constitution. Part XXIV. Aliphatic aldoximes, ketoximes, and ketoxime O-alkyl ethers, NN-dialkylhydrazines, aliphatic ketazines, mono- and di-alkylaminopropionitriles, alkoxypropionitriles, dialkyl azodiformates, and dialkyl carbonates. Bond parachors, bond refractions, and bondrefraction coefficients. *Journal of the Chemical Society (Resumed)* **1952**, 514-549.
107. Beaucage, G.; Composto, R.; Stein, R., Ellipsometric study of the glass transition and thermal expansion coefficients of thin polymer films. *Journal of Polymer Science Part B: Polymer Physics* **1993**, *31* (3), 319-326.
108. Wietzke, S.; Jansen, C.; Jung, T.; Reuter, M.; Baudrit, B.; Bastian, M.; Chatterjee, S.; Koch, M., Terahertz time-domain spectroscopy as a tool to monitor the glass transition in polymers. *Optics express* **2009**, *17* (21), 19006-19014.
109. Zeitler, J. A.; Taday, P. F.; Pepper, M.; Rades, T., Relaxation and crystallization of amorphous carbamazepine studied by terahertz pulsed spectroscopy. *Journal of pharmaceutical sciences* **2007**, *96* (10), 2703-2709.
110. Chakraborty, M.; Bawuah, P.; Tan, N.; Ervasti, T.; Pääkkönen, P.; Zeitler, J. A.; Ketolainen, J.; Peiponen, K.-E., On the correlation of effective terahertz refractive index and average surface roughness of pharmaceutical tablets. *Journal of Infrared, Millimeter, and Terahertz Waves* **2016**, *37* (8), 776-785.
111. Cogdill, R. P.; Short, S. M.; Forcht, R.; Shi, Z.; Shen, Y.; Taday, P. F.; Anderson, C. A.; Drennen, J. K., An efficient method-development strategy for quantitative chemical imaging using terahertz pulse spectroscopy. *Journal of Pharmaceutical Innovation* **2006**, *1* (1), 63-75.
112. Naftaly, M.; Miles, R., Terahertz time-domain spectroscopy of silicate glasses and the relationship to material properties. *Journal of Applied Physics* **2007**, *102* (4), 043517.
113. Dengale, S. J.; Grohgan, H.; Rades, T.; Löbmann, K., Recent advances in co-amorphous drug formulations. *Advanced drug delivery reviews* **2016**, *100*, 116-125.
114. Ellis, B.; Smith, R., *Polymers: a property database*. CRC Press: 2008.
115. Brittain, H. G., *Polymorphism in pharmaceutical solids*. CRC Press: 2016.
116. Taday, P. F., Applications of terahertz spectroscopy to pharmaceutical sciences. *Philosophical Transactions of the Royal Society of London. Series A: Mathematical, Physical and Engineering Sciences* **2003**, *362* (1815), 351-364.
117. Zeitler, J. A.; Taday, P. F.; Newnham, D. A.; Pepper, M.; Gordon, K. C.; Rades, T., Terahertz pulsed spectroscopy and imaging in the pharmaceutical setting-a review. *Journal of Pharmacy and Pharmacology* **2007**, *59* (2), 209-223.
118. Ikeda, Y.; Ishihara, Y.; Moriwaki, T.; Kato, E.; Terada, K., A novel analytical method for pharmaceutical polymorphs by terahertz spectroscopy and the optimization of crystal form at the discovery stage. *Chemical and Pharmaceutical Bulletin* **2010**, *58* (1), 76-81.

119. May, R. K.; Evans, M. J.; Zhong, S.; Warr, I.; Gladden, L. F.; Shen, Y.; Zeitler, J. A., Terahertz in-line sensor for direct coating thickness measurement of individual tablets during film coating in real-time. *Journal of Pharmaceutical Sciences* **2011**, *100* (4), 1535-1544.
120. Eriksson, M.; Alderborn, G., The effect of original particle size and tablet porosity on the increase in tensile strength during storage of sodium chloride tablets in a dry atmosphere. *International journal of pharmaceutics* **1995**, *113* (2), 199-207.
121. Loreti, S.; Wu, C.-Y., Three-dimensional discrete element modelling of three point bending tests: The effect of surface energy on the tensile strength. *Powder Technology* **2018**, *337*, 119-126.
122. Osei-Yeboah, F.; Sun, C. C., Validation and applications of an expedited tablet friability method. *International journal of pharmaceutics* **2015**, *484* (1-2), 146-155.
123. Tye, C. K.; Sun, C. C.; Amidon, G. E., Evaluation of the effects of tableting speed on the relationships between compaction pressure, tablet tensile strength, and tablet solid fraction. *Journal of pharmaceutical sciences* **2005**, *94* (3), 465-472.
124. Markl, D.; Strobel, A.; Schlossnikl, R.; Bötter, J.; Bawuah, P.; Ridgway, C.; Rantanen, J.; Rades, T.; Gane, P.; Peiponen, K.-E., Characterisation of pore structures of pharmaceutical tablets: A review. *International journal of pharmaceutics* **2018**, *538* (1-2), 188-214.
125. Food; Administration, D., Guidance for industry, PAT-A Framework for Innovative Pharmaceutical Development, Manufacturing and Quality Assurance. <http://www.fda.gov/cder/guidance/published.html> **2004**.
126. Short, S. M.; Cogdill, R. P.; Wildfong, P. L.; Drennen III, J. K.; Anderson, C. A., A near-infrared spectroscopic investigation of relative density and crushing strength in four-component compacts. *Journal of pharmaceutical sciences* **2009**, *98* (3), 1095-1109.
127. Tatavarti, A. S.; Fahmy, R.; Wu, H.; Hussain, A. S.; Marnane, W.; Bensley, D.; Hollenbeck, G.; Hoag, S. W., Assessment of NIR spectroscopy for nondestructive analysis of physical and chemical attributes of sulfamethazine bolus dosage forms. *aaps Pharmscitech* **2005**, *6* (1), E91-E99.
128. Ellison, C. D.; Ennis, B. J.; Hamad, M. L.; Lyon, R. C., Measuring the distribution of density and tableting force in pharmaceutical tablets by chemical imaging. *Journal of pharmaceutical and biomedical analysis* **2008**, *48* (1), 1-7.
129. Talwar, S.; Roopwani, R.; Anderson, C. A.; Buckner, I. S.; Drennen, J. K., Determination of spatially resolved tablet density and hardness using near-infrared chemical imaging (NIR-CI). *Applied spectroscopy* **2017**, *71* (8), 1906-1914.
130. Shah, R. B.; Tawakkul, M. A.; Khan, M. A., Process analytical technology: chemometric analysis of Raman and near infra-red spectroscopic data for predicting physical properties of extended release matrix tablets. *Journal of pharmaceutical sciences* **2007**, *96* (5), 1356-1365.
131. Lim, H.; Dave, V. S.; Kidder, L.; Lewis, E. N.; Fahmy, R.; Hoag, S. W., Assessment of the critical factors affecting the porosity of roller compacted ribbons and the feasibility of using NIR chemical imaging to evaluate the porosity distribution. *International journal of pharmaceutics* **2011**, *410* (1-2), 1-8.
132. Khorasani, M.; Amigo, J. M.; Sun, C. C.; Bertelsen, P.; Rantanen, J., Near-infrared chemical imaging (NIR-CI) as a process monitoring solution for a production line of roll compaction and tableting. *European Journal of Pharmaceutics and Biopharmaceutics* **2015**, *93*, 293-302.

133. Souihi, N.; Nilsson, D.; Josefson, M.; Trygg, J., Near-infrared chemical imaging (NIR-CI) on roll compacted ribbons and tablets–multivariate mapping of physical and chemical properties. *International journal of pharmaceutics* **2015**, *483* (1-2), 200-211.
134. Soh, J. L.; Boersen, N.; Carvajal, M. T.; Morris, K. R.; Peck, G. E.; Pinal, R., Importance of raw material attributes for modeling ribbon and granule properties in roller compaction: multivariate analysis on roll gap and NIR spectral slope as process critical control parameters. *Journal of Pharmaceutical Innovation* **2007**, *2* (3-4), 106-124.
135. Khorasani, M.; Amigo, J. M.; Bertelsen, P.; Sun, C. C.; Rantanen, J., Process optimization of dry granulation based tableting line: extracting physical material characteristics from granules, ribbons and tablets using near-IR (NIR) spectroscopic measurement. *Powder Technology* **2016**, *300*, 120-125.
136. Gupta, A.; Peck, G. E.; Miller, R. W.; Morris, K. R., Real-time near-infrared monitoring of content uniformity, moisture content, compact density, tensile strength, and Young's modulus of roller compacted powder blends. *Journal of pharmaceutical sciences* **2005**, *94* (7), 1589-1597.
137. Khorasani, M.; Amigo, J.; Sonnergaard, J.; Olsen, P.; Bertelsen, P.; Rantanen, J., Visualization and prediction of porosity in roller compacted ribbons with near-infrared chemical imaging (NIR-CI). *Journal of pharmaceutical and biomedical analysis* **2015**, *109*, 11-17.
138. Peeters, E.; Da Silva, A. F. T.; Toiviainen, M.; Van Renterghem, J.; Vercruyse, J.; Juuti, M.; Lopes, J. A.; De Beer, T.; Vervaet, C.; Remon, J.-P., Assessment and prediction of tablet properties using transmission and backscattering Raman spectroscopy and transmission NIR spectroscopy. *asian journal of pharmaceutical sciences* **2016**, *11* (4), 547-558.
139. Virtanen, S.; Antikainen, O.; Yliruusi, J., Determination of the crushing strength of intact tablets using Raman spectroscopy. *International journal of pharmaceutics* **2008**, *360* (1-2), 40-46.
140. Johansson, J.; Pettersson, S.; Folestad, S., Characterization of different laser irradiation methods for quantitative Raman tablet assessment. *Journal of pharmaceutical and biomedical analysis* **2005**, *39* (3-4), 510-516.
141. Hakulinen, M.; Pajander, J.; Leskinen, J.; Ketolainen, J.; Van Veen, B.; Niinimäki, K.; Pirskanen, K.; Poso, A.; Lappalainen, R., Ultrasound transmission technique as a potential tool for physical evaluation of monolithic matrix tablets. *AAPS PharmSciTech* **2008**, *9* (1), 267-273.
142. de Oliveira Jr, J. M.; Andreo Filho, N.; Chaud, M. V.; Angiolucci, T.; Aranha, N.; Martins, A. C. G., Porosity measurement of solid pharmaceutical dosage forms by gamma-ray transmission. *Applied Radiation and Isotopes* **2010**, *68* (12), 2223-2228.
143. Markl, D.; Wang, P.; Ridgway, C.; Karttunen, A.-P.; Chakraborty, M.; Bawuah, P.; Pääkkönen, P.; Gane, P.; Ketolainen, J.; Peiponen, K.-E., Characterization of the pore structure of functionalized calcium carbonate tablets by terahertz time-domain spectroscopy and X-ray computed microtomography. *Journal of pharmaceutical sciences* **2017**, *106* (6), 1586-1595.
144. Bawuah, P.; Silfsten, P.; Ervasti, T.; Ketolainen, J.; Zeitler, J. A.; Peiponen, K.-E., Non-contact weight measurement of flat-faced pharmaceutical tablets using terahertz transmission pulse delay measurements. *International journal of pharmaceutics* **2014**, *476* (1-2), 16-22.
145. Bawuah, P.; Ervasti, T.; Tan, N.; Zeitler, J. A.; Ketolainen, J.; Peiponen, K.-E., Noninvasive porosity measurement of biconvex tablets using terahertz pulses. *International journal of pharmaceutics* **2016**, *509* (1-2), 439-443.
146. Ridgway, C.; Bawuah, P.; Markl, D.; Zeitler, J. A.; Ketolainen, J.; Peiponen, K.-E.; Gane, P., On the role of API in determining porosity, pore structure and bulk modulus of the

- skeletal material in pharmaceutical tablets formed with MCC as sole excipient. *International journal of pharmaceutics* **2017**, 526 (1-2), 321-331.
147. Bawuah, P.; Chakraborty, M.; Ervasti, T.; Zeitler, J. A.; Ketolainen, J.; Gane, P. A.; Peiponen, K.-E., A structure parameter for porous pharmaceutical tablets obtained with the aid of Wiener bounds for effective permittivity and terahertz time-delay measurement. *International journal of pharmaceutics* **2016**, 506 (1-2), 87-92.
148. Bawuah, P.; Tan, N.; Tweneboah, S. N. A.; Ervasti, T.; Zeitler, J. A.; Ketolainen, J.; Peiponen, K.-E., Terahertz study on porosity and mass fraction of active pharmaceutical ingredient of pharmaceutical tablets. *European Journal of Pharmaceutics and Biopharmaceutics* **2016**, 105, 122-133.
149. Bawuah, P.; Markl, D.; Farrell, D.; Evans, M.; Portieri, A.; Anderson, A.; Goodwin, D.; Lucas, R.; Zeitler, J. A., Terahertz-based porosity measurement of pharmaceutical tablets: a tutorial. *Journal of Infrared, Millimeter, and Terahertz Waves* **2020**, 1-20.
150. Choy, T. C., *Effective medium theory: principles and applications*. Oxford University Press: 2015; Vol. 165.
151. Bruggeman, V. D., Berechnung verschiedener physikalischer Konstanten von heterogenen Substanzen. I. Dielektrizitätskonstanten und Leitfähigkeiten der Mischkörper aus isotropen Substanzen. *Annalen der physik* **1935**, 416 (7), 636-664.
152. Singh, R.; Muzzio, F. J.; Ierapetritou, M.; Ramachandran, R., A combined feed-forward/feed-back control system for a QbD-based continuous tablet manufacturing process. *Processes* **2015**, 3 (2), 339-356.
153. Food; Administration, D., Guidance for Industry Powder Blends and Finished Dosage Units-Stratified In-Process Dosage Unit Sampling and Assessment. <http://www.fda.gov/cder/guidance/index.htm> **2003**.
154. Davies, P. N.; Worthington, H. E.; Podczec, F.; Newton, J. M., The determination of the mechanical strength of tablets of different shapes. *European journal of pharmaceutics and biopharmaceutics* **2007**, 67 (1), 268-276.
155. Broitman, E., Indentation hardness measurements at macro-, micro-, and nanoscale: a critical overview. *Tribology Letters* **2017**, 65 (1), 23.
156. Doerner, M. F.; Nix, W. D., A method for interpreting the data from depth-sensing indentation instruments. *Journal of Materials research* **1986**, 1 (4), 601-609.
157. Jetzer, W., Measurement of hardness and strength of tablets and their relation to compaction performance of powders. *Journal of pharmacy and pharmacology* **1986**, 38 (4), 254-258.
158. Podczec, F., Methods for the practical determination of the mechanical strength of tablets—From empiricism to science. *International journal of pharmaceutics* **2012**, 436 (1-2), 214-232.
159. Alderborn, G.; Nystrom, C., Radial and axial tensile strength and strength variability of paracetamol tablets. *Acta pharmaceutica suecica* **1984**, 21 (1), 1-8.
160. AC10520925, A., *Standard test method for splitting tensile strength of intact rock core specimens*. ASTM Internat.: 2008.
161. ASTM, D., 3967, Standard Test Method for Splitting Tensile Strength of Intact Rock Core Specimens. *ASTM International, West Conshohocken, PA* **2016**.
162. Formulary, U. S. P. N., USPS35/NF30. *The United States Pharmacopoeial Convention* **2011**.

163. Paul, S.; Sun, C. C., Dependence of friability on tablet mechanical properties and a predictive approach for binary mixtures. *Pharmaceutical research* **2017**, *34* (12), 2901-2909.
164. Blanco, M.; Alcalá, M., Content uniformity and tablet hardness testing of intact pharmaceutical tablets by near infrared spectroscopy: a contribution to process analytical technologies. *Analytica chimica acta* **2006**, *557* (1-2), 353-359.
165. Blanco, M.; Alcalá, M.; González, J. M.; Torras, E., A process analytical technology approach based on near infrared spectroscopy: tablet hardness, content uniformity, and dissolution test measurements of intact tablets. *Journal of pharmaceutical sciences* **2006**, *95* (10), 2137-2144.
166. Kirsch, J. D.; Drennen, J. K., Nondestructive tablet hardness testing by near-infrared spectroscopy: a new and robust spectral best-fit algorithm. *Journal of pharmaceutical and biomedical analysis* **1999**, *19* (3-4), 351-362.
167. Li, J.; Jiang, Y.; Fan, Q.; Chen, Y.; Wu, R., Simultaneous determination of the impurity and radial tensile strength of reduced glutathione tablets by a high selective NIR-PLS method. *Spectrochimica Acta Part A: Molecular and Biomolecular Spectroscopy* **2014**, *125*, 278-284.
168. Morisseau, K. M.; Rhodes, C. T., Near-infrared spectroscopy as a nondestructive alternative to conventional tablet hardness testing. *Pharmaceutical research* **1997**, *14* (1), 108-111.
169. Otsuka, M., Chemoinformetrical evaluation of granule and tablet properties of pharmaceutical preparations by near-infrared spectroscopy. *Chemometrics and intelligent laboratory systems* **2006**, *82* (1-2), 109-114.
170. Pestieau, A.; Krier, F.; Thoorens, G.; Dupont, A.; Chavez, P.-F.; Ziemons, E.; Hubert, P.; Evrard, B., Towards a real time release approach for manufacturing tablets using NIR spectroscopy. *Journal of pharmaceutical and biomedical analysis* **2014**, *98*, 60-67.
171. Tanabe, H.; Otsuka, K.; Otsuka, M., Theoretical analysis of tablet hardness prediction using chemoinformetric near-infrared spectroscopy. *Analytical sciences* **2007**, *23* (7), 857-862.
172. Heigl, N.; Hodzic, A.; Llusa, M.; Tritthart, W.; Reiter, F.; Fraser, S.; Laggner, P.; Khinast, J., Potential of Raman spectroscopy for evaluating crushing strength of tablets. *Journal of pharmaceutical innovation* **2012**, *7* (2), 76-86.
173. Akseli, I.; Iyer, S.; Lee, H. P.; Cuitiño, A. M., A quantitative correlation of the effect of density distributions in roller-compacted ribbons on the mechanical properties of tablets using ultrasonics and X-ray tomography. *Aaps Pharmscitech* **2011**, *12* (3), 834-853.
174. Razavi, S. M.; Callegari, G.; Drazer, G.; Cuitino, A. M., Toward predicting tensile strength of pharmaceutical tablets by ultrasound measurement in continuous manufacturing. *International journal of pharmaceuticals* **2016**, *507* (1-2), 83-89.
175. Simonaho, S.-P.; Takala, T. A.; Kuosmanen, M.; Ketolainen, J., Ultrasound transmission measurements for tensile strength evaluation of tablets. *International journal of pharmaceuticals* **2011**, *409* (1-2), 104-110.
176. Peiponen, K.-E.; Bawuah, P.; Chakraborty, M.; Juuti, M.; Zeitler, J. A.; Ketolainen, J., Estimation of Young's modulus of pharmaceutical tablet obtained by terahertz time-delay measurement. *International journal of pharmaceuticals* **2015**, *489* (1-2), 100-105.
177. May, R. K.; Han, L.; Alton, J.; Zhong, S.; Elliott, J. A.; Byers, C.; Gladden, L. F.; Evans, M.; Shen, Y.; Zeitler, J. A. In *Pharmaceutical tablet hardness measurements with THz pulsed imaging*, 2009 34th International Conference on Infrared, Millimeter, and Terahertz Waves, IEEE: 2009; pp 1-2.
178. Augsburger, L. L.; Hoag, S. W., *Pharmaceutical dosage forms-tablets*. CRC press: 2016.

179. Miguelez-Moran, A.; Wu, C.-Y.; Seville, J., The effect of lubrication on density distributions of roller compacted ribbons. *International journal of pharmaceutics* **2008**, *362* (1-2), 52-59.
180. Sinka, I.; Burch, S.; Tweed, J.; Cunningham, J., Measurement of density variations in tablets using X-ray computed tomography. *International Journal of Pharmaceutics* **2004**, *271* (1-2), 215-224.
181. Michrafy, A.; Kadiri, M. S.; Dodds, J. A., Wall friction and its effects on the density distribution in the compaction of pharmaceutical excipients. *Chemical Engineering Research and Design* **2003**, *81* (8), 946-952.
182. Sinka, I.; Cunningham, J.; Zavaliangos, A., The effect of wall friction in the compaction of pharmaceutical tablets with curved faces: a validation study of the Drucker–Prager Cap model. *Powder Technology* **2003**, *133* (1-3), 33-43.
183. Standard, A., E384, Standard test method for microindentation hardness of materials. *West Conshohocken, PA: ASTM International* **2000**.
184. Busignies, V.; Leclerc, B.; Porion, P.; Evesque, P.; Couarraze, G.; Tchoreloff, P., Quantitative measurements of localized density variations in cylindrical tablets using X-ray microtomography. *European journal of pharmaceutics and biopharmaceutics* **2006**, *64* (1), 38-50.
185. Wahl, P.; Pucher, I.; Scheibelhofer, O.; Kerschhaggl, M.; Sacher, S.; Khinast, J., Continuous monitoring of API content, API distribution and crushing strength after tableting via near-infrared chemical imaging. *International journal of pharmaceutics* **2017**, *518* (1-2), 130-137.
186. Igne, B.; Anderson, C. A.; Drennen III, J. K., Radial tensile strength prediction of relaxing and relaxed compacts by near-infrared chemical imaging. *International journal of pharmaceutics* **2011**, *418* (2), 297-303.
187. May, R. K.; Evans, M. J.; Zhong, S.; Byers, C.; Gladden, L. F.; Shen, Y.; Zeitler, J. A. In *Terahertz pulsed imaging of surface variations on pharmaceutical tablets*, 35th International Conference on Infrared, Millimeter, and Terahertz Waves, IEEE: 2010; pp 1-2.
188. Zhang, J.; Pei, C.; Schiano, S.; Heaps, D.; Wu, C.-Y., The application of terahertz pulsed imaging in characterising density distribution of roll-compacted ribbons. *European Journal of Pharmaceutics and Biopharmaceutics* **2016**, *106*, 20-25.
189. Abebe, A.; Akseli, I.; Sprockel, O.; Kottala, N.; Cuitiño, A. M., Review of bilayer tablet technology. *International journal of pharmaceutics* **2014**, *461* (1-2), 549-558.
190. Li, S. P.; Karth, M. G.; Feld, K. M.; Di Paolo, L. C.; Pendharkar, C. M.; Williams, R. O., Evaluation of bilayer tablet machines—a case study. *Drug development and industrial pharmacy* **1995**, *21* (5), 571-590.
191. Benkerrou, L.; Galley, O.; Quinet, F.; Abebe, A.; Timmins, P., Multilayered tablet containing pravastatin and aspirin and method. Google Patents: 2004.
192. Efentakis, M.; Peponaki, C., Formulation study and evaluation of matrix and three-layer tablet sustained drug delivery systems based on carbopols with isosorbite mononitrate. *AAPS PharmSciTech* **2008**, *9* (3), 917-923.
193. Vaithiyalingam, S. R.; Sayeed, V. A., Critical factors in manufacturing multi-layer tablets—Assessing material attributes, in-process controls, manufacturing process and product performance. *International journal of pharmaceutics* **2010**, *398* (1-2), 9-13.

194. Krumme, M.; Zerbe, H. G., Smatrix System: Design Characteristics and Release Properties of a Novel Erosion-Controlled Oral Delivery System. In *Modified-Release Drug Delivery Technology*, CRC Press: 2002; pp 83-100.
195. Nirmal, J.; Saisivam, S.; Peddanna, C.; Muralidharan, S.; Godwinkumar, S.; Nagarajan, M., Bilayer tablets of atorvastatin calcium and nicotinic acid: formulation and evaluation. *Chemical and Pharmaceutical Bulletin* **2008**, *56* (10), 1455-1458.
196. Shiyani, B.; Gattani, S.; Surana, S., Formulation and evaluation of bi-layer tablet of metoclopramide hydrochloride and ibuprofen. *AAPS PharmSciTech* **2008**, *9* (3), 818-827.
197. LaForce, C.; Gentile, D. A.; Skoner, D. P., A randomized, double-blind, parallel-group, multicenter, placebo-controlled study of the safety and efficacy of extended-release guaifenesin/pseudoephedrine hydrochloride for symptom relief as an adjunctive therapy to antibiotic treatment of acute respiratory infections. *Postgraduate medicine* **2008**, *120* (2), 53-59.
198. Charman, W. N.; Charman, S. A., Oral Modified-Release Delivery Systems. In *Modified-release drug delivery technology*, CRC Press: 2002; pp 25-34.
199. Bangalore, S.; Kamalakkannan, G.; Parkar, S.; Messerli, F. H., Fixed-dose combinations improve medication compliance: a meta-analysis. *The American journal of medicine* **2007**, *120* (8), 713-719.
200. Verma, R. K.; Garg, S., Drug delivery technologies and future directions. *Pharmaceutical Technology* **2001**, *25* (2), 1-14.
201. Serebruany, V. L.; Malinin, A. I.; Sane, D. C.; Jilma, B.; Takserman, A.; Atar, D.; Hennekens, C. H., Magnitude and time course of platelet inhibition with Aggrenox® and Aspirin in patients after ischemic stroke: the AGgrenox versus Aspirin Therapy Evaluation (AGATE) trial. *European journal of pharmacology* **2004**, *499* (3), 315-324.
202. Akseli, I.; Abebe, A.; Sprockel, O.; Cuitiño, A. M., Mechanistic characterization of bilayer tablet formulations. *Powder technology* **2013**, *236*, 30-36.
203. Podczeck, F.; Drake, K.; Newton, J.; Haririan, I., The strength of bilayered tablets. *European journal of pharmaceutical sciences* **2006**, *29* (5), 361-366.
204. Dietrich, P.; Bauer-Brandl, A.; Schubert, R., Influence of tableting forces and lubricant concentration on the adhesion strength in complex layer tablets. *Drug development and industrial pharmacy* **2000**, *26* (7), 745-754.
205. Wu, C.-Y.; Seville, J. P., A comparative study of compaction properties of binary and bilayer tablets. *Powder Technology* **2009**, *189* (2), 285-294.
206. Hinz, D. C., Process analytical technologies in the pharmaceutical industry: the FDA's PAT initiative. *Analytical and bioanalytical chemistry* **2006**, *384* (5), 1036-1042.
207. Akseli, I.; Dey, D.; Cetinkaya, C., Mechanical property characterization of bilayered tablets using nondestructive air-coupled acoustics. *AAPS PharmSciTech* **2010**, *11* (1), 90-102.
208. Felton, L. A., *Aqueous polymeric coatings for pharmaceutical dosage forms*. CRC Press: 2016.
209. Ciurczak, E. W.; Igne, B., *Pharmaceutical and medical applications of near-infrared spectroscopy*. CRC Press: 2014.
210. Luybaert, J.; Massart, D.; Vander Heyden, Y., Near-infrared spectroscopy applications in pharmaceutical analysis. *Talanta* **2007**, *72* (3), 865-883.
211. Gendrin, C.; Roggo, Y.; Collet, C., Pharmaceutical applications of vibrational chemical imaging and chemometrics: a review. *Journal of pharmaceutical and biomedical analysis* **2008**, *48* (3), 533-553.

212. Roggo, Y.; Chalus, P.; Maurer, L.; Lema-Martinez, C.; Edmond, A.; Jent, N., A review of near infrared spectroscopy and chemometrics in pharmaceutical technologies. *Journal of pharmaceutical and biomedical analysis* **2007**, *44* (3), 683-700.
213. Andersson, M.; Josefson, M.; Langkilde, F. W.; Wahlund, K. G., Monitoring of a film coating process for tablets using near infrared reflectance spectrometry. *Journal of pharmaceutical and biomedical analysis* **1999**, *20* (1), 27-37.
214. Cogdill, R. P.; Forcht, R. N.; Shen, Y.; Taday, P. F.; Creekmore, J. R.; Anderson, C. A.; Drennen, J. K., Comparison of Terahertz Pulse Imaging and Near-Infrared Spectroscopy for Rapid, Non-Destructive Analysis of Tablet Coating Thickness and Uniformity. *Journal of Pharmaceutical Innovation* **2007**, *2* (1-2), 29-36.
215. Kirsch, J. D.; Drennen, J. K., Determination of film-coated tablet parameters by near-infrared spectroscopy. *Journal of Pharmaceutical and Biomedical Analysis* **1995**, *13* (10), 1273-1281.
216. Kirsch, J. D.; Drennen, J. K., Near-infrared spectroscopic monitoring of the film coating process. *Pharmaceutical Research* **1996**, *13* (2), 234-237.
217. Moes, J. J.; Ruijken, M. M.; Gout, E.; Frijlink, H. W.; Ugwoke, M. I., Application of process analytical technology in tablet process development using NIR spectroscopy: blend uniformity, content uniformity and coating thickness measurements. *Int J Pharm* **2008**, *357* (1-2), 108-18.
218. Möltgen, C.-V.; Puchert, T.; Menezes, J.; Lochmann, D.; Reich, G., A novel in-line NIR spectroscopy application for the monitoring of tablet film coating in an industrial scale process. *Talanta* **2012**, *92*, 26-37.
219. Ozawa, T.; Yokoyama, M.; Hosono, T.; Nagato, T.; Tahara, K.; Takeuchi, H., A novel approach to monitor coating amount by short-wavelength near-infrared spectroscopy using a tracer with a long-chain hydrocarbyl group. *International journal of pharmaceuticals* **2013**, *458* (1), 9-14.
220. Igne, B.; Arai, H.; Drennen, J. K.; Anderson, C. A., Effect of sampling frequency for real-time tablet coating monitoring using near infrared spectroscopy. *Applied spectroscopy* **2016**, *70* (9), 1476-1488.
221. Gendre, C.; Boiret, M.; Genty, M.; Chaminade, P.; Pean, J. M., Real-time predictions of drug release and end point detection of a coating operation by in-line near infrared measurements. *International journal of pharmaceuticals* **2011**, *421* (2), 237-243.
222. Pérez-Ramos, J. D.; Findlay, W. P.; Peck, G.; Morris, K. R., Quantitative analysis of film coating in a pan coater based on in-line sensor measurements. *Aaps Pharmscitech* **2005**, *6* (1), E127-E136.
223. Knop, K.; Kleinebudde, P., PAT-tools for process control in pharmaceutical film coating applications. *Int J Pharm* **2013**, *457* (2), 527-36.
224. Fitzgerald, A. J.; Cole, B. E.; Taday, P. F., Nondestructive analysis of tablet coating thicknesses using terahertz pulsed imaging. *Journal of pharmaceutical sciences* **2005**, *94* (1), 177-183.
225. Russe, I. S.; Brock, D.; Knop, K.; Kleinebudde, P.; Zeitler, J. A., Validation of Terahertz coating thickness measurements using X-ray microtomography. *Mol Pharm* **2012**, *9* (12), 3551-9.
226. Lin, H.; May, R. K.; Evans, M. J.; Zhong, S.; Gladden, L. F.; Shen, Y.; Zeitler, J. A., Impact of Processing Conditions on Inter-tablet Coating Thickness Variations Measured by Terahertz In-Line Sensing. *J Pharm Sci* **2015**, *104* (8), 2513-22.

227. Lin, H.; Dong, Y.; Shen, Y.; Axel Zeitler, J., Quantifying Pharmaceutical Film Coating with Optical Coherence Tomography and Terahertz Pulsed Imaging: An Evaluation. *Journal of Pharmaceutical Sciences* **2015**, *104* (10), 3377-3385.
228. May, R. K.; Evans, M. J.; Zhong, S.; Warr, I.; Gladden, L. F.; Shen, Y.; Zeitler, J. A., Terahertz in-line sensor for direct coating thickness measurement of individual tablets during film coating in real-time. *J Pharm Sci* **2011**, *100* (4), 1535-44.
229. Lin, H.; Dong, Y.; Markl, D.; Williams, B. M.; Zheng, Y.; Shen, Y.; Zeitler, J. A., Measurement of the Intertablet Coating Uniformity of a Pharmaceutical Pan Coating Process With Combined Terahertz and Optical Coherence Tomography In-Line Sensing. *J Pharm Sci* **2017**, *106* (4), 1075-1084.
230. Momose, W.; Yoshino, H.; Katakawa, Y.; Yamashita, K.; Imai, K.; Sako, K.; Kato, E.; Irisawa, A.; Yonemochi, E.; Terada, K., Applying terahertz technology for nondestructive detection of crack initiation in a film-coated layer on a swelling tablet. *Results Pharma Sci* **2012**, *2*, 29-37.
231. Lin, H.; Dong, Y.; Pei, C.; Williams, B. M.; Markl, D.; Zheng, Y.; Elliot, J. A.; Shen, Y.; Zeitler, J. A., Studying the Pharmaceutical Film Coating Process with Terahertz Sensing, Optical Coherence Tomography and Numerical Modelling. In *2016 41st International Conference on. IEEE, Infrared, Millimeter, and Terahertz waves (IRMMW-THz)*: 2016.
232. Maurer, L.; Leuenberger, H., Terahertz pulsed imaging and near infrared imaging to monitor the coating process of pharmaceutical tablets. *Int J Pharm* **2009**, *370* (1-2), 8-16.
233. Zhong, S.; Shen, Y.-C.; Ho, L.; May, R. K.; Zeitler, J. A.; Evans, M.; Taday, P. F.; Pepper, M.; Rades, T.; Gordon, K. C.; Müller, R.; Kleinebudde, P., Non-destructive quantification of pharmaceutical tablet coatings using terahertz pulsed imaging and optical coherence tomography. *Optics and Lasers in Engineering* **2011**, *49* (3), 361-365.
234. Dohi, M.; Momose, W.; Yoshino, H.; Hara, Y.; Yamashita, K.; Hakomori, T.; Sato, S.; Terada, K., Application of terahertz pulse imaging as PAT tool for non-destructive evaluation of film-coated tablets under different manufacturing conditions. *J Pharm Biomed Anal* **2016**, *119*, 104-13.
235. Zeitler, J. A.; Shen, Y.; Baker, C.; Taday, P. F.; Pepper, M.; Rades, T., Analysis of coating structures and interfaces in solid oral dosage forms by three dimensional terahertz pulsed imaging. *J Pharm Sci* **2007**, *96* (2), 330-40.
236. Ho, L.; Muller, R.; Gordon, K. C.; Kleinebudde, P.; Pepper, M.; Rades, T.; Shen, Y.; Taday, P. F.; Zeitler, J. A., Applications of terahertz pulsed imaging to sustained-release tablet film coating quality assessment and dissolution performance. *J Control Release* **2008**, *127* (1), 79-87.
237. Ho, L.; Muller, R.; Gordon, K. C.; Kleinebudde, P.; Pepper, M.; Rades, T.; Shen, Y.; Taday, P. F.; Zeitler, J. A., Terahertz pulsed imaging as an analytical tool for sustained-release tablet film coating. *Eur J Pharm Biopharm* **2009**, *71* (1), 117-23.
238. Ho, L.; Muller, R.; Gordon, K. C.; Kleinebudde, P.; Pepper, M.; Rades, T.; Shen, Y.; Taday, P. F.; Zeitler, J. A., Monitoring the film coating unit operation and predicting drug dissolution using terahertz pulsed imaging. *J Pharm Sci* **2009**, *98* (12), 4866-76.
239. Ho, L.; Muller, R.; Romer, M.; Gordon, K. C.; Heinamaki, J.; Kleinebudde, P.; Pepper, M.; Rades, T.; Shen, Y. C.; Strachan, C. J.; Taday, P. F.; Zeitler, J. A., Analysis of sustained-release tablet film coats using terahertz pulsed imaging. *J Control Release* **2007**, *119* (3), 253-61.

240. Müller, J.; Brock, D.; Knop, K.; Zeitler, J. A.; Kleinebudde, P., Prediction of dissolution time and coating thickness of sustained release formulations using Raman spectroscopy and terahertz pulsed imaging. *European Journal of Pharmaceutics and Biopharmaceutics* **2012**, *80* (3), 690-697.
241. Spencer, J. A.; Gao, Z.; Moore, T.; Buhse, L. F.; Taday, P. F.; Newnham, D. A.; Shen, Y.; Portieri, A.; Husain, A., Delayed release tablet dissolution related to coating thickness by terahertz pulsed image mapping. *J Pharm Sci* **2008**, *97* (4), 1543-50.
242. Odani, N.; Mohan, S.; Kato, E.; Feng, H.; Li, Y.; Hossain, M. N.; Drennen III, J. K.; Anderson, C. A., Determining the effect of photodegradation on film coated nifedipine tablets with terahertz based coating thickness measurements. *European Journal of Pharmaceutics and Biopharmaceutics* **2019**, *145*, 35-41.
243. Markl, D.; Hanneschläger, G.; Sacher, S.; Leitner, M.; Buchsbaum, A.; Pescod, R.; Baele, T.; Khinast, J. G., In-line monitoring of a pharmaceutical pan coating process by optical coherence tomography. *Journal of pharmaceutical sciences* **2015**, *104* (8), 2531-2540.
244. Zhong, S.; Shen, Y.; Shen, H.; Evans, M. J.; May, R. K.; Zeitler, J. A.; Warr, I. In *Near-infrared spectroscopy for non-destructive coating analysis calibrated by terahertz pulsed imaging*, 35th International Conference on Infrared, Millimeter, and Terahertz Waves, IEEE: 2010; pp 1-2.